Applied Computational Electromagnetics Society

Journal

February 2011 Vol. 26 No. 2

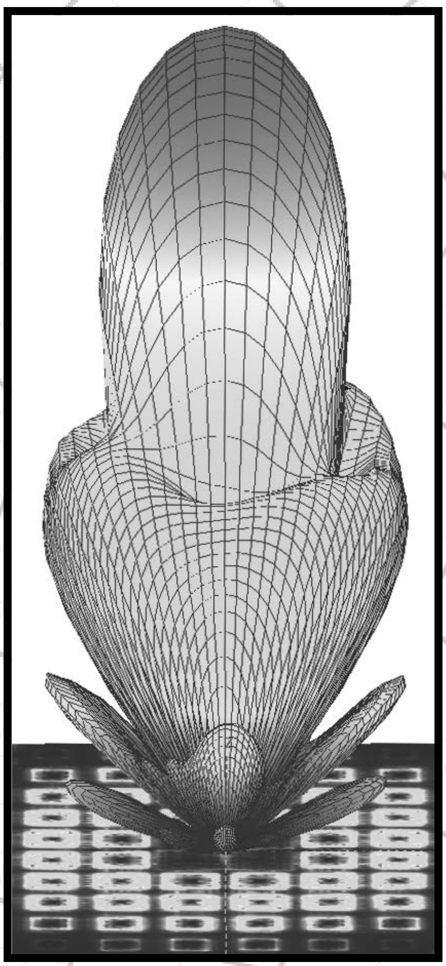

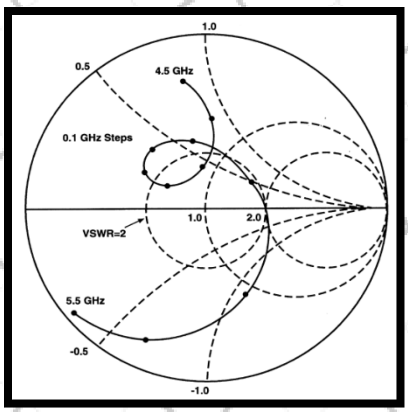

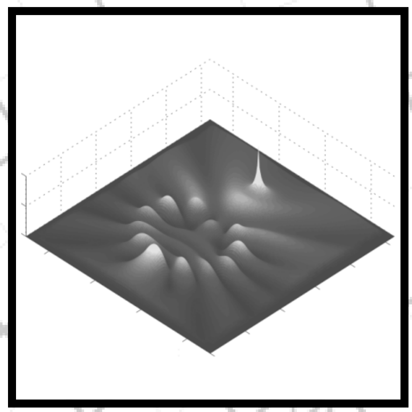

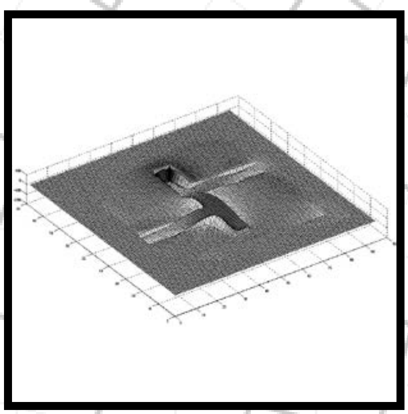

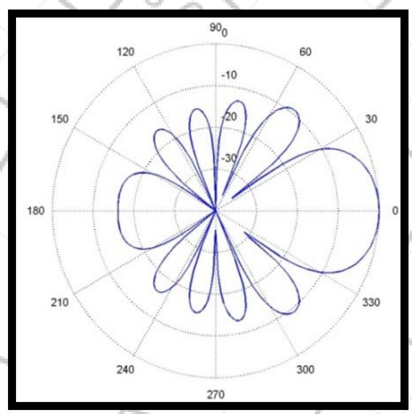

ISSN 1054-4887

GENERAL PURPOSE AND SCOPE: The Applied Computational Electromagnetics Society ***(ACES)*** Journal hereinafter known as the ***ACES Journal*** is devoted to the exchange of information in computational electromagnetics, to the advancement of the state-of-the art, and the promotion of related technical activities. The primary objective of the information exchange is to inform the scientific community on the developments of new computational electromagnetics tools and their use in electrical engineering, physics, or related areas. The technical activities promoted by this publication include code validation, performance analysis, and input/output standardization; code or technique optimization and error minimization; innovations in solution technique or in data input/output; identification of new applications for electromagnetics modeling codes and techniques; integration of computational electromagnetics techniques with new computer architectures; and correlation of computational parameters with physical mechanisms.

SUBMISSIONS: The ***ACES Journal*** welcomes original, previously unpublished papers, relating to applied computational electromagnetics. Typical papers will represent the computational electromagnetics aspects of research in electrical engineering, physics, or related disciplines. However, papers which represent research in applied computational electromagnetics itself are equally acceptable.

Manuscripts are to be submitted through the upload system of ***ACES*** web site http://aces.ee.olemiss.edu See "Information for Authors" on inside of back cover and at ***ACES*** web site. For additional information contact the Editor-in-Chief:

Dr. Atef Elsherbeni
Department of Electrical Engineering
The University of Mississippi
University, MS 386377 USA
Phone: 662-915-5382
Email: atef@olemiss.edu

SUBSCRIPTIONS: All members of the Applied Computational Electromagnetics Society are entitled to access and download the ***ACES Journal*** any published journal article available at http://aces.ee.olemiss.edu. Printed issues of the ***ACES Journal*** are delivered to institutional members. Each author of published papers receives a printed issue of the ***ACES Journal*** in which the paper is published.

Back issues, when available, are $50 each. Subscription to ***ACES*** is through the web site. Orders for back issues of the ***ACES Journal*** and change of address requests should be sent directly to ***ACES*** office at:

Department of Electrical Engineering
The University of Mississippi
University, MS 386377 USA
Phone: 662-915-7231
Email: aglisson@olemiss.edu

Allow four weeks advance notice for change of address. Claims for missing issues will not be honored because of insufficient notice, or address change, or loss in the mail unless the ***ACES*** office is notified within 60 days for USA and Canadian subscribers, or 90 days for subscribers in other countries, from the last day of the month of publication. For information regarding reprints of individual papers or other materials, see "Information for Authors".

LIABILITY. Neither ***ACES***, nor the ***ACES Journal*** editors, are responsible for any consequence of misinformation or claims, express or implied, in any published material in an ***ACES Journal*** issue. This also applies to advertising, for which only camera-ready copies are accepted. Authors are responsible for information contained in their papers. If any material submitted for publication includes material which has already been published elsewhere, it is the author's responsibility to obtain written permission to reproduce such material.

APPLIED COMPUTATIONAL ELECTROMAGNETICS SOCIETY JOURNAL

February 2011
Vol. 26 No. 2
ISSN 1054-4887

The ACES Journal is abstracted in INSPEC, in Engineering Index, DTIC, Science Citation Index Expanded, the Research Alert, and to Current Contents/Engineering, Computing & Technology.

The illustrations on the front cover have been obtained from the research groups at the Department of Electrical Engineering, The University of Mississippi.

FEBRUARY 2011 REVIEWERS

Iftikhar Ahmed
Rodolfo Araneo
Sami Barmada
Deb Chatterjee
Jingyi Chen
William Coburn
Jorge Costa
Jianjun Ding
Andrew L. Drozd
Alistar Duffy
Khaled ElMahgoub
Nathan Ida
Leo Kempel
Marco Klingler
Giampiero Lovat
Antonino Musolino
Andrew Peterson
Lorena Lozano Plata
Levent Sevgi
Fernando Teixeira
Theodoros Tsiboukis
Yasuhiro Tsunemitsu
Ahmet Turk
Veerakumar Venugopal
Su Yan
Korkut Yegin
Amir Zaghloul

THE APPLIED COMPUTATIONAL ELECTROMAGNETICS SOCIETY

JOURNAL

Vol. 26 No. 2 February 2011

TABLE OF CONTENTS

An Improved MM-PO Method with UV Technique for Scattering from an Electrically Large Ship on a Rough Sea Surface at Low Grazing Angle

S. Y. He[1], C. Li[1], F. Zhang[1], G. Q. Zhu[1], W. D. Hu[2], and W. X. Yu[3]

[1] School of Electronic Information
Wuhan University, Wuhan, 430079, China
siyuanhi@gmail.com, whunpredestiny@gmail.com, zhfJoyce@hotmail.com, gqzhu@whu.edu.cn

[2] ATR Lab.
National University of Defense technology, Changsha, 410073, China
wdhu@nudt.edu.cn

[3] School of Electronic Information and Electrical Engineering
Shanghai Jiao Tong University, Shanghai, 200240, China
wxyu@sjtu.edu.cn

Abstract **—** An improved MM-PO-UV hybrid method is developed to calculate the bistatic scattering from the two-dimensional (2-D) composite model of an electrically large ship (ELS) on a one-dimensional (1-D) rough sea surface at a low grazing angle (LGA). The subdivision of the MM and PO region is performed flexibly according to the physical considerations. The MM region contains not only the ship but also a small portion of the neighboring sea region where the surface currents need to be modeled accurately. An iterative solution BiCGSTAB is adopted to solve the final matrix equation of a large dimension caused by the ELS. Then, a UV matrix decomposition technique is applied as the fast algorithm to accelerate the matrix-vector productions and the matrix elements filling in. The improved method makes it possible for the Monte-Carlo simulation of large-scale complex target/rough surface problems under an LGA. The accuracy is validated in comparison with the traditional MOM method.

Index Terms **—** LGA, MM-PO hybrid method, target/rough surface scattering, UV.

I. INTRODUCTION

Electromagnetic scattering from the composite model of a ship on a rough surface is of practical importance to long-range radar surveillance, oceanic remote sensing, and target tracking [1-4]. The low grazing angle (LGA) scattering from the rough surface without a target has been widely studied [5], but the study of target/rough surface scattering under an LGA is much more difficult, because the analysis of these problems is complicated by the many possible interactions between the target and the surface, especially when the target is of arbitrary shape and large electrical size. Some numerical methods based on method of moments have been developed for target/rough surface scattering, e.g., the forward backward method (FBM) [3] and finite element method (FEM) [6]. But the application of the traditional MOM method is restricted when the target and the sea surface are both of large electric scale and is further limited for the LGA incidence. Monte Carlo simulation for scattering from an electrically large ship (ELS) on a rough sea surface under a LGA incidence becomes

1054-4887 © 2011 ACES

impractical because of an extremely large memory requirement and long computation time. For such large-scale target/ rough surface problems, an efficient method is needed. In our previous studies, a hybrid method MM-PO-UV was introduced to compute the scattering from a target above a sea surface [7].

For ELS on the surface under an LGA, two improvements have been made to this MM-PO-UV hybrid method in this paper. Firstly, the subdivision of the MM and PO region is performed flexibly according to the physical considerations. The MM region contains the ship and a small portion of the neighboring sea surface on the illuminated side where the surface currents need to be modeled accurately in the simulation. Secondly, an iterative solution is applied to solve the large matrix equation caused by the ELS, which is difficult to be solved by direct inversion. To further improve the efficiency, a UV fast algorithm is applied to accelerate the computation during per iterative step. With the two improvements, the method proposed is ideally suited for application to LGA scattering from an arbitrarily shaped target of large electric size on the sea surface.

The remainder of the paper is organized as follows. In section 2, the solution of the improved method is proposed. Then Monte Carlo simulations for bistatic scattering from the composite model of an ELS on a Pierson-Morkowitz rough sea surface at an LGA incidence are demonstrated and discussed in section 3. The results are validated in comparison with the traditional MOM method. Finally, the conclusion is given in section 4.

II. SOLUTION OF THE IMPROVED METHOD

As shown in Fig. 1, a ship is located on the sea surface of length L . Some geometrical parameters will be given later in the computation. For simplicity in explaining the algorithm, the ship and the sea surfaces are assumed to be perfectly conducting and they are illuminated from the left by a TE polarized (with electric field $\hat{y}$ indirection) tapered wave $\vec{E}_i(\vec{r})$ with a tapering parameter g incident along the direction $\vec{k} = k(\hat{x}\sin\theta_i - \hat{z}\cos\theta_i)$, where θ_i is the LGA.

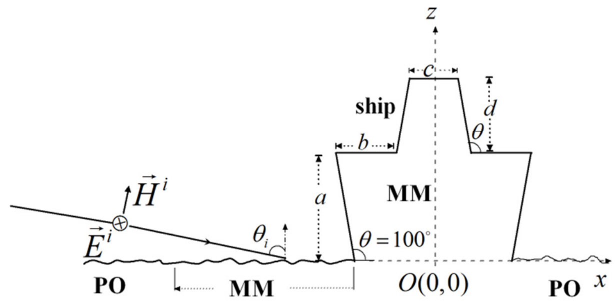

Fig. 1. The model of a ship on rough sea surface.

Within the traditional MM-PO framework, the surface of the scattering model is split into a MM region and a PO region. In our previous research, only the target above the surface is treated as the MM region. For a ship on the rough sea surface, the first improvement made to the hybrid method is to assign the two regions flexibly according to the physical considerations. In this model, the ship target has remarkable induction interaction with the neighboring sea surface on the illuminated side. So the MM region contains not only the ship but also a small portion of the neighboring sea surface where the currents need to be modeled accurately in the simulation. The length of the sea surface in the MM region is an adjustable parameter and set comparable to the height of the ship. This length chosen takes into account all the induction interaction and it won’t bring too much computation. The remaining sea surface is considered as the PO region because the re-radiation interaction with the ship is significant in this region, whereas the induction is obvious in the neighboring sea surface. Since a very large sea surface must be included to allow an LGA incidence, the number of current unknowns in the MM region is typically far smaller than the total number of surface current unknowns.

After the subdivision of the MM and PO region is performed, it is possible to follow the similar process in our previous research [7]. Thus, the final matrix equation obtained by constraining the boundary condition in the MM region can be written as:

$$(\overline{\overline{Z}}_{MM,MM} + \overline{\overline{Z}}_{MM,PO} \cdot \overline{\overline{M}}_{PO,MM}) \cdot \overline{I}_{MM} = \overline{V}_{MM}, \quad (1)$$

where $\overline{\overline{Z}}_{MM,MM}$ is the self-impedance matrix of the MM region. $\overline{\overline{Z}}_{MM,PO}$ is the mutual impedance matrix between the currents in the MM region and the PO region. $\overline{\overline{M}}_{PO,MM}$ is called the magnetic-reaction matrix [8] indicating the excitation from the currents in the MM region to the PO region. The dimension of matrices $\overline{\overline{Z}}_{MM,MM}$, $\overline{\overline{Z}}_{MM,PO}$ and $\overline{\overline{M}}_{PO,MM}$ are, $N_{MM} \times N_{MM}$, $N_{MM} \times N_{PO}$, and $N_{PO} \times N_{MM}$, respectively.

For an ELS, N_{MM} becomes large while N_{PO} is much larger than N_{MM} under an LGA incidence. In our former studies [7], the MM-PO-UV method was demonstrated only for an object of moderate size above a rough surface, so the final matrix equation could be solved directly and the UV matrix decomposition technique is mainly combined for the fast filling-in of the matrix elements. When an ELS is presented in this paper, the MM region results in a final matrix equation of large size, which is difficult to be solved by the direct solution. The second improvement in our study is to apply a proper iterative solution to solve the large matrix equation. The well-known BiCGSTAB (ell) [9] is chosen as the iterative solver. Thus, the bottleneck is the calculation of the product of the matrix and a column vector. Then, the UV matrix decomposition techniques could be further combined in the iterative steps.

During per iterative step of the solution, two matrix-vector multiplications $\overline{\overline{Z}}_{MM,MM} \cdot \overline{I}_{MM}$ and $\overline{\overline{Z}}_{MM,PO} \cdot \overline{\overline{M}}_{PO,MM} \cdot \overline{I}_{MM}$ should be calculated. To accelerate the computation of the matrix-vector products, the matrices $\overline{\overline{Z}}_{MM,MM}$, $\overline{\overline{Z}}_{MM,PO}$, and $\overline{\overline{M}}_{PO,MM}$ are considered and replaced by a set of self, near and far interaction sub-matrices in a multilevel way. The multilevel scheme is exactly similar to that proposed for the three-dimensional (3-D) problems in [10]. Each considered matrix is divided into a series of sub-matrix blocks according to the interaction distances. Generally, the rank of the sub-matrix is dependent on the distance between two interaction regions. Therefore, those far interaction sub-matrices with a low rank could be compressed by the UV matrix decomposition technique [11] based on low-rank criterion and interpolation technology.

According to the UV matrix decomposition algorithm, the given far interaction sub-matrix with low rank r could be approximated by the product of a U and V matrix,

$$\overline{\overline{z}}_{m\times n} = \overline{\overline{U}}_{m\times r} \overline{\overline{V}}_{r\times n} ,$$

where $r << \min(m,n)$. The matrix decomposition is achieved by sampling a small number of rows and columns within the original sub matrix. Therefore, the computational complexity drops from $o(m\times n)$ to $o(r\times(m+n))$ for both the memory requirements and the CPU time consumed in matrix vector multiplication.

The detailed multilevel UV method for the 1-D rough surface scattering had been discussed in [11]. The detailed multilevel UV method for the 3-D problems had been discussed in [10]. In this paper, the multilevel UV method is transformed and applied for 2-D problems. According to the multilevel scheme, the interaction of the matrices $\overline{\overline{Z}}_{MM,PO}$ and $\overline{\overline{M}}_{PO,MM}$ is distinguished as either near interaction or far interaction. Because a large portion of the sea surface is far away from the MM region, most blocks represent the far interaction between the two regions. Only a small portion of the sea surface in the PO region is near the MM region, so the two interaction matrices have a very high compressing ratio by using the multi-level UV method.

III. RESULTS AND DISCUSSIONS

Numerical results are presented and discussed in this section to demonstrate the accuracy and efficiency of this improved method. The validity of the improved method is proved firstly. Then, the method is applied to obtain the LGA scattering from ELS on the sea surface. The results of the large ship case are compared with a smaller one. For all the results, the Pierson-Morkowitz rough sea surface is driven by the wind with a given speed $U = 5\,m/s$.

To validate the improved MM-PO-UV hybrid method, simulation results for the composite model under an LGA $\theta_i = 80^o$ are illustrated and compared with the traditional MOM method. In this validation, the geometrical size of the model is chosen exactly the same as presented in [6]. The surface length is $L = 409.6\lambda$ (λ is the wavelength, $\lambda = 1\,m$) and the tapered wave takes $g = L/6 = 68.2\lambda$. As described in Fig. 1, the electrical size of the ship has $a = 9\lambda$, $b = 5\lambda$, $c = 4\lambda$, $d = 6\lambda$, and $\theta = 100^{\circ}$. The ship geometry is about 15λ high and the deck is 16.1λ wide. The contour of the ship above the sea water has a length of 44.95λ. Considering the height of the ship, a length of 15λ of the sea surface to the left of the ship is considered as the MM region in the improved method.

Figure 2 gives the magnitude of the currents as a function of the length along the contour of the ship from the illuminated side (left side) to the dark side (right side). It is observed that the results of the improved MM-PO-UV hybrid method (the dotted line) and the MOM method (the solid line) are in excellent agreement with each other.

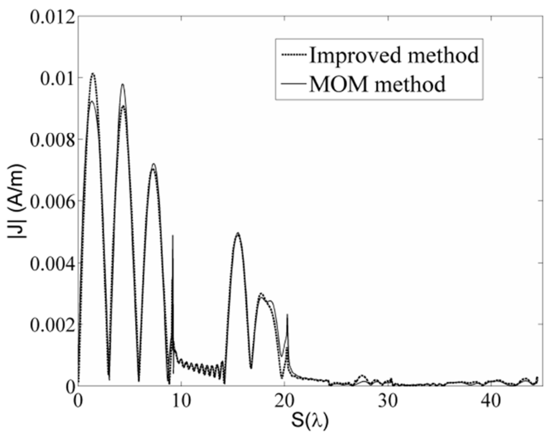

Fig. 2. Comparison of currents on the ship between the improved method and the MOM method .

Figure 3 shows the bistatic scattering results over 50 Monte Carlo realizations of the three methods: MM-PO-UV hybrid method (the dashed line), the improved method (the dotted line), and the MOM method (the solid line). It can be seen that the results of the improved method agree with the MOM method better than the hybrid method without improvements.

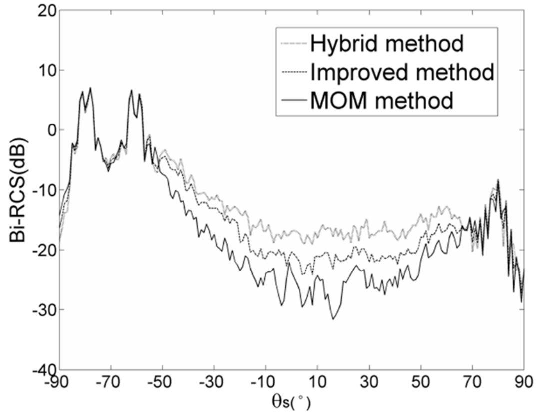

Fig. 3. Comparison of bistatic scattering for three methods.

For comparison, the main memory requirements and the computational time of the three methods in Fig. 3 are given in Table 1. It could be concluded that the improved method has better accuracy when its requirements for the computational resources remain almost the same as the hybrid method.

Table 1: Memory requirements and relative computational time

Method	**Unknowns**	**Memory(MB)**	**Time(s)**
MOM	3804	197	690
Improved	745	44	42
Hybrid	620	42	29

The composite model scattering feature has positive correlation with the shape characteristic of the ship and the distribution of the sea surface. As shown in Fig. 1, the ship's hull forms a large 80^o corner reflector with respect to the flat sea surface. The deck house on top of the ship makes a 100^o corner reflector with the sea surface. Considering the incident angle from the left, strong interactions exist between the near-specular directions of the corner reflectors. It is of interest to see how the coupling interactions contribute to the scattering.

The specular reflection of the corner reflectors formed by the ship and the sea is illustrated in Fig. 4. Figure 4(a) indicates the backscattering path, which involves two reflections from the sea surface and one bounce from the ship's hull. Figure 4 (b) shows the backward scattering in the direction $\theta_s = -60^o$ contributed by two different paths. Both the two paths involve a reflection from the sea surface and a bounce from the ship.

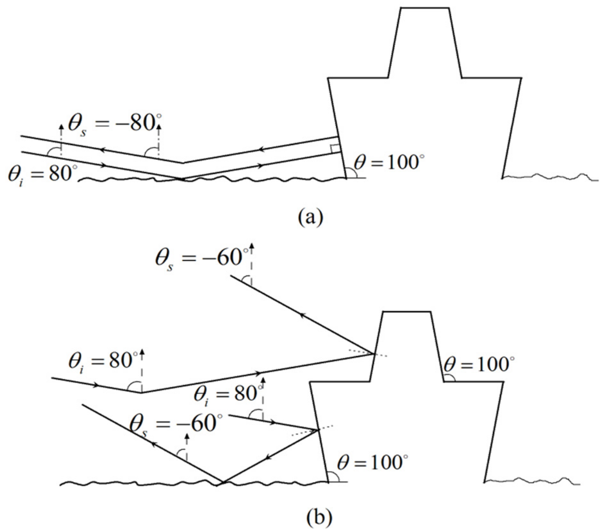

Fig. 4. Specular reflection of the corner reflectors between the ship and the sea surface.

Compared with the corner reflectors formed by the sea surface, the deckhouse also forms a 100^o corner reflector with the deck itself, which is much smaller. The physics of scattering waves interpreted in Fig. 5 (a) indicates that the return wave contributes to the direction $\theta_s = -60^o$. In Fig. 5 (b), the incidence is reflected by the deckhouse directly because its direction is normal to the left of the deckhouse on the top.

Due to the specular and diffuse reflection, it is expected that the corner reflectors will give rise to a very high RCS in the near-specular directions over a wide degrees range. As expected, the RCS in Fig. 3 is greatly enhanced over a broad range of scattering degrees $\Delta\Phi$ ($\Delta\Phi = [-85^\circ, -55^\circ]$) due to the strong interactions between the ship and the sea. The forward near-specular scattering is also strong over the degree range $\Delta\Psi$ ($\Delta\Psi = [75^\circ, 85^\circ]$). The improved hybrid method matches well with the traditional MOM method over the range $\Delta\Phi$ and $\Delta\Psi$, which is of great interest in the practical engineering problems. The peak at forward direction and the backward peaks match exactly well with the traditional MOM method because the PO approximation shows more accuracy in this near-specular directions.

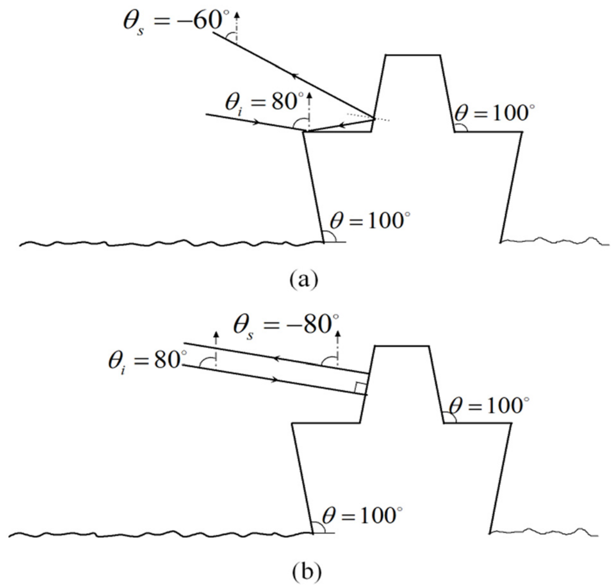

Fig. 5. Specular reflection by the ship itself.

Under the LGA incidence, selection of g and L should be large enough to ensure the convergence. However, a much longer surface results in a huge number of current unknowns, which makes the computation impractical. Previously, no numerical results have been reported involving a rough sea surface much larger than $L = 409.6\lambda$ applied in this composite model. In this paper, a much larger g and L is selected to make sure the ratio of the illuminated intensity on the target to the tapered wave peak can reach to 0.94 [13]. The tapered wave control parameter is chosen as follows:

$$g = 4(r/\cos\theta_i + h\tan\theta_i). \qquad (2)$$

For the composite model in our study, r is the maximum radius of the ship circled by the dotted line in Fig. 6 , h corresponds to the height of the circle center. θ_i is the incidence angle. We have $r = 11\lambda$, $h = 7.5\lambda$ computed in this case, and a $g = 423.7\lambda$ is calculated according to Eq. (2) .

Figure 7 compares the scattering from the composite model with different g and L but with the same other parameters given in the validation.

(1) $g = 68.2\lambda$; $L = 409.6\lambda$;

(2) $g = 423.7\lambda$; $L = 4g = 1694\lambda$;

(3) $g = 423.7\lambda$; $L = 6g = 2542\lambda$.

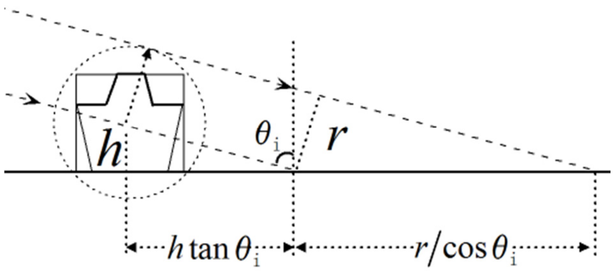

Fig. 6. Sufficient illumination by the tapered wave under an LGA.

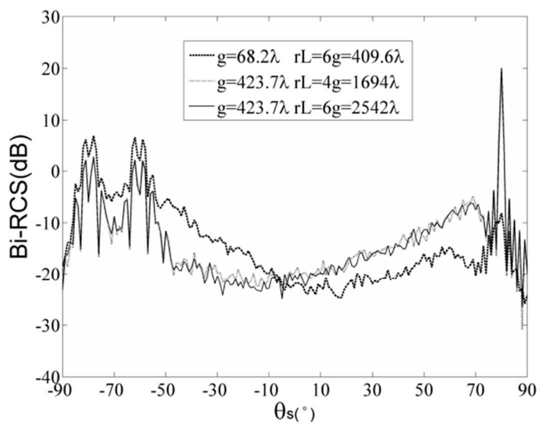

Fig. 7. Bistatic scattering of the same ship with different g and L.

It can be seen that the scattering results for the small $g = 68.2\lambda$, $L = 409.6\lambda$ is not convergent in Fig. 7. That's because when under an LGA incidence, not only the sea region interacting with the ship is greatly enlarged, but also the primary scattering of the ship in the forward direction reaches a much farther area of the sea surface. Obviously, the composite model is not fully illuminated by the incident tapered wave with $g = 68.2\lambda$. But it is observed that when g is chosen large enough to ensure the illumination, then a surface length of $L = 4g$ is sufficient for the simulation.

In the following, this proposed method in our study is applied to a large ship case calculating the LGA scattering from ELS on a sea. The numerical results are compared with a smaller ship case. The smaller ship case has parameters:

$a = 9\lambda, b = 5\lambda, c = 4\lambda, d = 6\lambda$; $g = 423.7\lambda$, $L = 4g = 1694\lambda$.

The large ship case has parameters:

$a = 36\lambda$, $b = 20\lambda$, $c = 16\lambda$, $d = 24\lambda$; $g = 1694\lambda, L = 4g = 6779\lambda$.

The large ship is about 60λ high and the deck is 64.4λ wide. The contour of the ship above the sea water has a length of 179.8λ. The MOM region contains the ship and a small portion of the nearby sea surface with a length of 60λ. A sampling of 10 points per wavelength will result in 1798 ship surface current unknowns and a total of 67790 rough surface current unknowns. The large number of unknowns would be prohibitive for standard approaches to the MOM, especially if a three-dimensional problem must be considered. Applying the improved MM-PO-UV hybrid method, the final matrix equation is of size 2398, which is far smaller than the unknowns used in the MOM method but still difficult to be solved directly. This proposed method makes it possible for the simulation of scattering from an electrically large ship on an extremely large-scale sea surface.

Comparison is made between the smaller ship case and the large ship case in Fig. 8. It is shown that the RCS is strong over a range of near-specular degrees $\Delta\Phi$ ($\Delta\Phi = [-85^\circ, -55^\circ]$) for both cases. But the strong RCS results split for the smaller ship case in the scattering angles $\theta_s = -80^\circ$ and $\theta_s = -60^\circ$ where the RCS reach sharp peaks for the large ship case. To explain this phenomenon, the total scattering from the composite model can be decomposed into two scattering terms: 1) the ship term refers to the scattering contributed by the radiation of currents on the ship; 2) the sea term means the scattering contributed by the radiation of currents on the sea surface.

Figure 9 compares the two decomposed scattering terms of the smaller ship case. It is noticed obviously that the sea term is stronger than the ship term over $\Delta\Phi$ ($\Delta\Phi = [-85^\circ, -55^\circ]$), which is the near-specular directions. The backward scattering over $\Delta\Phi$ is dominated by the sea term due to the re-radiation interaction from the ship.

Compared with the smaller ship case in Fig. 9, each scattering term in Fig. 10 for the large ship case is greatly enhanced over the range $\Delta\Phi$. That's because as the electrical size of the ship is increased, the sea regions interacting with the ship become larger. Thus, the coupling interaction between the large ship and a wider area of the sea surface is apparently stronger than the smaller ship case, which gives rise to higher RCS in the near-specular directions. As a result of the large size, the ship term is greatly intensified and it has a very close value to the sea term in the backscattering.

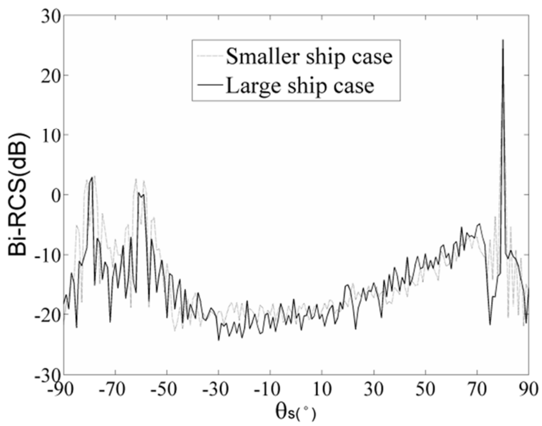

Fig. 8. Comparison of bistatic scattering between a large ship case and a smaller ship case.

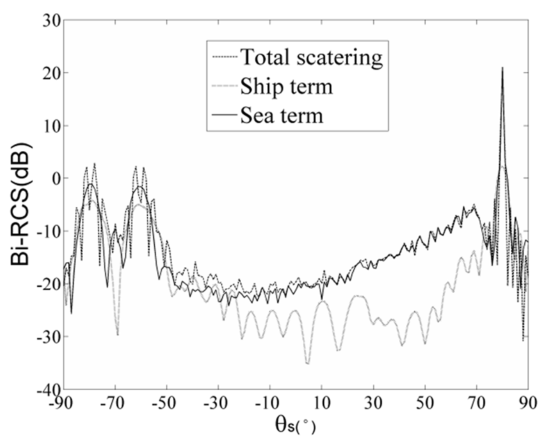

Fig. 9. Scattering terms of the smaller ship case.

To explain the two backward splits of the small ship case, the phase of the scattered field contributed by each scattering term is extracted, respectively. Taking the split in $\theta_s = -80^\circ$ as an example, the phase of the ship term is -60° and the sea term is 90.1°. There's a phase difference of about $\Delta\varphi = 150.1^\circ$ between the two scattering terms. Although each scattering term reaches a high value in the backscattering angle $\theta_s = -80^\circ$ respectively, the total scattering is reduced due to the nearly opposite phase of the two scattering terms. The phase difference could reduce the scattering but it will also enhance the total scattering results. Different to the smaller ship case, the RCS of the large ship case in the backscattering is greatly strengthened, because of the nearly same phase.

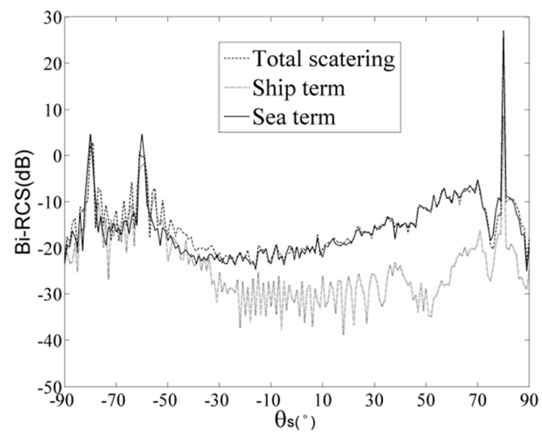

Fig. 10. Scattering terms of the large ship case.

Furthermore, energy conservation by integrating bistatic scattering over the upper half space is given in [11]:

$$P = \int_{-\frac{\pi}{2}}^{\frac{\pi}{2}} d\theta_s \sigma(\theta_s). \qquad (3)$$

In our simulations, the value calculated is close to the unity. The accuracy of the algorithm for the energy conservation is validated.

IV. CONCLUSION

With the improvements made to the hybrid method, its scope of application is enhanced for complex large-scale problems such as an arbitrarily shaped ship target of large electrical scale on the surface under an LGA. In this study, the subdivision of the MM and PO region is performed flexibly according to the physical considerations. An iterative solution combining the UV decomposition method is applied to solve the large matrix equation. The accuracy of the proposed method was validated by the comparison made with the MOM method. As the large number of unknowns would be prohibitive for standard approaches to the MOM, the efficient hybrid method makes it possible for large-scale complex problems, and the large number of simulations can be handled in a reasonable amount of time.

ACKNOWLEDGMENT

This work is supported by the National Natural Science Foundation of China under Grant No. 61001059, by the China Postdoctoral Science Foundation, and by the Fundamental Research Funds for the Central Universities.

REFERENCES

[1] E. A. Shtager, “An Estimation of Sea Surface Influence on Radar Reflectivity of Ships,” *IEEE Transactions on Antennas and Propagation*, vol. 47, no. 10, pp. 1623-1627, Oct. 1999.

[2] R. J. Burkholder, M. R. Pino, and F. Obelleiro, “A Monte Carlo Study of the Rough Sea Surface Influence on the Radar Scattering from 2-D Ships,” *IEEE Transactions on Antennas and Propag. Mag.*, vol. 43, no. 2, 25-33, Apr. 2001.

[3] M. R. Pino, R. J. Burkholder, and F. Obelleiro, “Spectral Acceleration of the Generalized Forward-Backward Method,” *IEEE Trans. Antennas Propag.*, vol. 50, no. 6, pp. 785-797, Jun. 2002.

[4] K. Jamil and R. J. Burkholder, “Radar Scattering from a Rolling Target Floating on a Time-Evolving Rough Sea Surface,” *IEEE Trans. Geosci. Remote Sens.*, vol. 44, no. 11, pp. 3330-3337, 2006.

[5] C. H. Chan, L. Tsang, and Q. Li, “Monte Carlo Simulations of Large-Scale One Dimensional Random Rough-Surface Scattering at Near Grazing Incidence: Penetrable Case,” *IEEE Trans. Antennas Propag.*, vol. 46, no. 1, pp. 142–149, Jan. 1998.

[6] P. Liu and Y. Q. Jin, “Numerical Simulation of Bistatic Scattering from a Target at Low Altitude above Rough Sea Surface under an EM-Wave Incidence at Low Grazing Angle by using the Finite Element Method,” *IEEE Trans. Antennas Propag.*, vol. 52, no. 5, pp. 1205-1210, May 2004.

[7] S. Y. He and G. Q. Zhu, “A Hybrid MM-PO Method Combining UV Technique for Scattering from Two-Dimensional Target above a Rough Surface,” *Microwave Opt. Technol. Lett.*, vol. 49, no. 12, pp. 2957-2960, Dec. 2007.

[8] H. T. Chen, J. X. Luo, and G. Q. Zhu, “Using UV Technique to Accelerate the MM-PO Method for Three-Dimensional Radiation and Scattering Problem,” *Microwave Opt. Technol. Lett.*, vol. 48, no. 8, pp. 1615 -1618, 2006.

[9] E. Topsakal, R. Kindt, K. Sertel, and J. Volakis, “Evaluation of the BiCGSTAB(l) Algorithm for Finite-Element/Boundary-Integral Method,” *IEEE Trans. Antennas Propagation Magazine*, vol. 43, no. 6, pp. 124-131, Dec. 2001.

[10] F. S. Deng, S. Y. He, H. T. Chen, W. D. Hu, W. X. Yu, and G. Q. Zhu, “Numerical Simulation of Vector Wave Scattering from the Target and Rough Surface Composite Model with 3-D Multilevel UV Method,” *IEEE Trans. Antennas Propagat.*, vol. 58, no. 5, pp. 1625-1634, May 2010.

[11] L. Tsang, D. Chen, P. Xu, Q. Li, and V. Jandhyala, “Wave Scattering with the UV Multilevel Partitioning Method: 1. Two-Dimensional Problem of Perfect Electric Conductor Surface Scattering,” *Radio Science*, vol. 39, RS5010, Oct. 2004.

[12] L. Tsang, J. A. Kong, K. H. Ding, and C. O. Ao, *Scattering of Electromagnetic Waves*, *Numerical Simulations*, Wiley-Interscience, Hoboken, N. J., 2001.

[13] H. X. Ye and Y. Q. Jin, “Fast Iterative Approach to Difference Scattering from the Object above a Rough Surface,” *IEEE Trans. Geosci. Remote Sens.*, vol. 44, no. 1, pp. 108-115, Jan. 2006.

S. Y. He was born in 1982. She received the telecommunication engineering degree and the Ph.D. degree in Radio Physics from Wuhan University, Wuhan, China, in 2003 and 2009, respectively. She is currently a post doctoral researcher at Wuhan University. From 2005 to 2006, she was a Research Assistant in Wireless Communications Research Centre,

City University of Hong Kong. Her research interests include EM theory and its application, computational electromagnetic, and radar imaging.

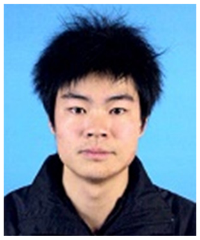

C. Li was born in 1986. He received the B.S. degree in Information Countermeasure Technology from North University of China, China, in 2008. He is currently working towards the Ph.D. degree in Radio Physics at Wuhan University, Wuhan, China. His current research interests are in numerical methods in electromagnetism, inverse scattering, electromagnetic scattering, and radiation.

F. Zhang was born in 1986. She received the telecommunication engineering degree from Wuhan University, Wuhan, China, in 2009. She is currently working towards the Ph.D. degree in Radio Physics at Wuhan University, Wuhan, China. Her current research interests include electromagnetic scattering and complex objects characterizing.

The PMC-Amended DB Boundary – A Canonical EBG Surface

Per-Simon Kildal[1], Ahmed Kishk[1,2], Marko Bosiljevac[3], and Zvonimir Sipus[3]

[1] Department of Signals and Systems
Chalmers University of Technology, 41296 Gothenburg, SWEDEN
per-simon.kildal@chalmers.se

[2] Department of Electrical Engineering
University of Mississippi, University, MS 38677-1848, USA
ahmed@olemiss.edu

[3] Faculty of Electrical Engineering and Computing
University of Zagreb, HR-10000 Zagreb, Croatia
marko.bosiljevac@fer.hr, zvonimir.sipus@fer.hr

Abstract **─** Replacing realistic materials and structures by their ideal counterparts, canonical surfaces, is of great interest for initial and conceptual electromagnetic (EM) studies. The recently introduced DB boundary is defined by a set of simple boundary conditions forcing the normal components of the D- and B- fields to be zero at the boundary. We show that this DB boundary produces many 2-D scattering results that are similar to how practical so-called electromagnetic bandgap (EBG) surfaces behave within the bandgap. Still, it is not directly useable as a canonical EBG surface, because, as we demonstrate in this paper, it is incomplete, creating an anomaly for normal incidence which causes unphysical field solution for 3-D field problems. We have removed this anomaly by introducing the PMC-amended DB boundary. This works in the same way as a practically realized EBG surface for both 2-D and 3-D problems within the bandgap, and is therefore a canonical EBG surface.

Index Terms **─** DB boundary, EBG surfaces, mushroom surface.

I. INTRODUCTION

The present paper will explain some simplified and ideal boundary conditions that can be referred to as canonical surfaces because they have a physically realizable counterpart. Such canonical surfaces are useful for the further development and unification of the metamaterials area. These ideal boundary conditions include perfect electric conductors (PEC), perfect magnetic conductors (PMC), ideal soft and hard surfaces [1] (represented by PEC/PMC strip grids [2]), and the newly introduced DB boundary [3]. Each of them has a physical realizable counterpart, provided in the latter case that the original DB boundary condition is amended. The present paper will show that the physical counterpart of the amended DB surface is the electromagnetic bandgap (EBG) surface. The name DB boundary refers to the fact that the vertical components of both the D-field and the B-field at the boundary are defined to be zero.

The anisotropic soft surface was introduced in analogy with acoustics to explain why certain surfaces stop waves from propagating along them. Later, it was shown that isotropic high impedance surfaces could stop surface waves as well [4]. The latter are now more correctly referred to as electromagnetic bandgap surfaces, because most so-called high impedance surfaces only have high surface impedance for normal incidence, whereas the wave-stop characteristics are related to the non-existence of surface waves along the surface, and not to this high surface impedance. The hard surface was introduced as the complement to the original soft surface, allowing waves of any polarization to propagate freely along it. This was then used for removing blockage by cylindrical objects [5], nowadays referred to as cloaking [6].

The guest editorial in [7] gave a joint comprehensive presentation of the EBG surfaces and the soft and hard surfaces by defining ideal canonical surfaces and their boundary conditions, but it also stated the lack of a simple boundary condition for the EBG surface. The present paper explains how the newly introduced DB boundary [3] can be amended to provide such a simple boundary condition and thereby can represent an ideal EBG surface, or in other words an ideal, isotropic and polarization-independent soft surface. The amendment is needed because the DB boundary condition is undefined for normal incidences, i.e., it is incomplete and needs to be amended. As a result, an anomaly appears in some field solutions. The present paper shows how the DB boundary condition can be amended to avoid such anomalies, providing the direction of wave propagation along the EBG surface is known. The amended DB surface is referred as a PMC-amended DB surface.

The computational and analytical simplifications offered by the canonical surfaces have already proven to be advantageous for numerical solutions [8] and generation of conceptually new microwave devices, such as the invisible hard struts in [5] representing the first metamaterial cloak, and the new gap waveguide described in [9]. The latter is a generalization of the single hard-wall parallel-plate waveguide [10], and represents a way to guide local waves (beams) in the gap between parallel metal plates. It originates from the miniaturized hard waveguide in [11-12], and the concept can also be used for packaging of microstrip circuits [13]. The gap waveguides make use of high impedance surface or EBG surface to suppress parallel plate modes, a physical phenomenon that is easily explained in terms of the ideal PMC or amended DB boundaries, respectively.

II. CANONICAL SURFACES: PEC, PMC, PEC/PMC STRIP GRID, PMC-AMENDED DB BOUNDARY

Artificial surfaces like soft and hard surfaces, artificial magnetic conductors, high impedance surfaces, and electromagnetic bandgap surfaces can be used to control wave propagation: enhance it in desired directions, stop it in undesired directions, and improve polarization characteristics of both. These properties can be explained by reference to Table 1. This was first presented in [2], updated and improved in [6], and it is here extended by introducing the PMC-amended DB boundary as a canonical surface having similar property as the EBG surface at the "best" frequency within the bandgap. The table contains also the related D′B′ boundary as explained below. The boundary conditions of the ideal canonical surfaces are also added to Table 1. Notice that we did not impose any frequency dependence of the boundary condition because we consider ideal surfaces. Actual realizations of the canonical surfaces will always have strong frequency dependences (except for the PEC).

The explanations of the boundaries are:

Perfect Electric Conductor (PEC): This surface is widely used in most EM modeling and computations as it describes metal conductors very well when analyzing guiding or radiating properties in the microwave region. The boundary conditions are well defined.

Perfect Magnetic Conductor (PMC): The EM field theory is easily extended to allow PMC. This surface does not exist naturally, but it can be realized artificially within frequency bands and is then referred to as an artificial magnetic conductor (AMC). The ideal boundary condition is well defined and it appears often in practice at the beginning of the frequency band of operation of the AMC.

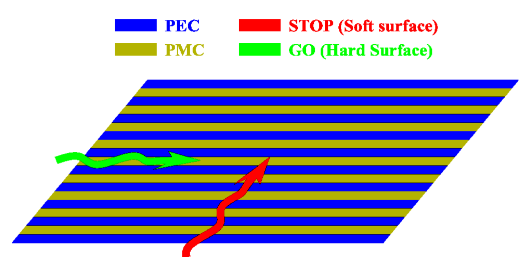

Fig. 1. Visualization of the PEC/PMC strip grid showing the STOP and GO directions.

PEC/PMC strip grid: This is the physical equivalent of an ideal soft/hard surface, see Fig. 1. The surface has locally infinite and unidirectional electric and magnetic conductivity, i.e. both the electric and magnetic currents can only flow in the strips direction. The PEC/PMC strips can follow any arbitrarily shaped path of planar or non planar form. For the transverse soft case (STOP surface) the PEC/PMC strip grids form electric/magnetic current fences that stop wave propagation, and for the longitudinal hard case (GO surface) they form electric/magnetic current lanes that enhance wave propagation. The ideal boundary conditions are well defined, and many realizations exist. The two most common realizations are corrugations and metal-strip-loaded grounded dielectric substrates. In the first case the ridges of the corrugations represent PEC strips, while the PMC strips are obtained by λ/4 transformers formed by the grooves. In the metal-strip-loaded case, the strips naturally represent PEC strips, and the PMC strips are obtained similarly as in the corrugated case by λ/4 transformers present between the ground plane and the dielectric surface. The ideal boundary conditions appear also for these realizations in the beginning of the frequency band where they work as soft or hard surfaces.

DB boundary: The boundary condition states that both the vertical E and the vertical H field components are zero. (The original formulation is vertical D and the vertical B field components being zero, but we limit our practical interpretations to surfaces in vacuum or air.) Thereby, it stops waves at grazing angles for both horizontal and vertical polarizations for all angles of incidence. Therefore, it works similar to an EBG surface, or in other words like an isotropic soft surface. The boundary condition is well defined, except for the case of a plane wave under vertical (normal) incidence to the surface. For normal plane wave incidence the incoming fields have no vertical components, and therefore the boundary condition is automatically satisfied for any reflection coefficient. Thus, the reflection coefficients as well as the boundary conditions are undefined for normal incidence, or in other words the boundary condition is incomplete. In most cases this will mean that the normally incident waves will pass through the boundary. The reflection coefficient of a realized EBG surface has always a phase that varies with elevation angle for TE case, in such a way that it appears like a PEC for grazing incidence and like a PMC for normal incidence. The anomaly of the reflection properties of the ideal DB boundary for normal incidence has therefore some relation to peculiarities of its practical counterpart. This

Table 1: **Left:** Characteristics of different types of canonical surfaces with respect to propagation of waves along the surface for different E-field polarizations. VER means vertical polarization (i.e. TM-case), HOR means horizontal (i.e. TE-case). The background color and pattern symbolize the PEC (yellow), PMC (blue) and PEC/PMC strips (parallel yellow and blue strips). The different orientations of the colored strips for the soft and hard cases symbolize STOP (current fences) and GO (current lanes) characteristics for waves propagating from left to right (as shown by the arrows) in the paper plane. The colored background in the box of the DB boundary is a PMC-type EBG symbolized by the texture of Sievenpiper's EBG mushroom surface. The D′B′ surface has no known realization. **Right:** Ideal boundary conditions of the canonical surfaces. The boundary conditions of the DB and D′B′ boundaries are in Lindell's work described in terms of the D and B fields rather than E and H, but here we have chosen the more common E and H field boundary conditions that are equivalent to the original boundary conditions for our practical case considering the interface to an air-filled region.

Canonical Surface		E-field Polarization		Ideal boundary condition (in xy-plane)
		VER (TM)	HOR (TE)	
PEC		GO	STOP	$E_x = E_y = 0$ & $\partial E_z / \partial z = 0$
PMC		STOP	GO	$H_x = H_y = 0$ & $\partial H_z / \partial z = 0$
PEC/PMC Strip grid	SOFT	STOP	STOP	$E_y = 0$ & $H_y = 0$
	HARD	GO	GO	$E_x = 0$ & $H_x = 0$ $\partial E_z / \partial z = 0$
PMC-amended DB boundary	EBG	STOP	STOP	$E_z = 0$ & $H_z = 0$, amended by (1)
D′B′ boundary (???)		GO	GO	$\partial E_z / \partial z = 0$ & $\partial H_z / \partial z = 0$ (incomplete)

anomaly causes some strange unphysical field solutions for some special cases and needs therefore to be corrected. This will be discussed in the next section.

D′B′ boundary: By analogy with the DB boundary, the D′B′ boundary is an isotropic hard surface defined by the boundary conditions seen in Table 1. However, in contrast to the DB boundary no realization of the D′B′ boundary is known so at present it is of little practical interest.

The characteristics of the three different surfaces with respect to polarization of the grazing waves are also illustrated in Table 1. The PEC supports vertically polarized waves that can propagate with strong amplitude; it is a "GO" surface for vertical polarization. These propagating waves are not really surface waves in the mathematical sense, because they are represented by a branch point rather than a pole in the spectral domain. Thus, they are for the ideal case surface waves at cut-off (linked to the corresponding space waves) rather than normal isolated surface waves trapped by the surface. However, when the surface has a thin dielectric coating, the wave along the surface becomes a TM surface wave (i.e. a pole). The PEC STOPs effectively horizontally polarized waves, because the horizontal field component is zero. The PMC behaves naturally in the opposite (dual) way; it is a GO surface easily passing waves along it for horizontal polarization and a "STOP" surface for vertical polarization (see table). The classical soft/hard surfaces can be represented physically by a PEC/PMC strip grid as explained above and illustrated in the table as well. This will STOP waves propagating with both horizontal and vertical polarizations when the strips are oriented transverse to the direction of propagation (soft case), and it will allow the waves to pass (i.e. GO) when they are oriented longitudinally in the same direction as the waves propagate (hard case).

The soft/hard surfaces were originally realized by metal corrugations or metal strips loading a grounded substrate. The soft/hard characteristics appear when they are oriented transversely/longitudinally with respect to the direction of wave propagation. For the soft case, they form so-called electric and magnetic current fences that stop the waves, and for the hard case they form electric and magnetic current lanes that enhance wave propagation.

III. AMENDING THE ORIGINAL DB BOUNDARY

The realized 2-D periodic EBG surfaces behave normally like PMC within some frequency band (or bands) for wave incidence close to normal. However, for wave incidence close to grazing angle and within the lower part of the same frequency band, the EBG surfaces behave more like transverse PEC/PMC strip surface, i.e. like a soft surface stopping waves. The original anisotropic 1-D periodic soft surface has STOP characteristics over an infinite bandwidth for the TE case (i.e. horizontal polarization), provided the period is small enough. Still, the 2-D EBG surfaces are preferable in some applications (such as in the cut-off regions of gap waveguides) because they are isotropic, stopping waves from any direction. For grazing incidence, the 2-D periodic EBG surfaces normally transform from STOP to PMC-type surface at the upper edge of the stop band. These rather complex characteristics of the 2-D EBG surfaces make them impossible to categorize completely in terms of PEC and PMC boundary conditions. However, as stated in the table, the DB boundary characterizes them well. Still, practical EBG surfaces may also be used as PMC ground planes (for low profile electric current radiators), and this characteristic the DB boundary cannot capture. In fact, as already stated before, the DB boundary condition has no effect on normal incident waves, i.e. the solution is undefined which makes the boundary condition incomplete. Therefore, the original DB boundary condition needs to be completed, or amended.

We propose here to amend the original DB boundary condition in the following way:

$$\begin{aligned}&\text{Original DB boundary:} \quad E_n = 0, \;\; H_n = 0\\&\text{Amended DB boundary:} \quad E_n = 0, \;\; H_n + jH_l = 0\end{aligned} \tag{1}$$

where E_n and H_n are normal components of the E- and H-fields at the boundary and H_l is the longitudinal component in the direction of wave propagation along the surface. Here we prefer to be more general and for that reason we have introduced a local surface normal n, which is referred to by the index z in Table 1. This means that the amendment only can be used if we know the direction of wave propagation along the surface. This is not always known, but luckily in most antenna problems the direction of wave propagation is well known.

We will now study field solutions obtained analytically and numerically for two illustrative cases, plane wave scattering from an EBG cylinder and radiation from a horizontal dipole over an EBG surface. The purpose is to visualize the anomaly appearing for the latter case, and to show that the proposed amendment gives results in agreement with numerical simulations which include all the details of the practically realized EBG structure.

IV. SCATTERING FROM CYLINDER WITH EBG SURFACE

In order to understand the characteristics of the DB boundary and confirm our assessments, we first compare its behavior with other canonical surfaces. The series solutions for the scattering from circular cylinders are considered in this section. The scattering from a DB circular cylinder due to the normal plane wave incidence is found to be exactly the same as the scattering from a circular cylinder of PEC/PMC strips directed longitudinally parallel to the cylinder axis [14, 15]. Also, for plane wave under grazing incidence (along the cylinder axis) the scattering from a DB cylinder is exactly the same as for a cylinder with circumferentially directed PEC/PMC strips. However, these exact equalities are only true if the undefined boundary condition is neglected at the point along the cross section of the cylinder where the wave has normal incidence at the DB boundary itself. It is here argued that this point can be neglected because it represents an infinitesimally small part of the complete circumferential boundary. It should also be emphasized that the two series solutions of the PEC/PMC cylinders were obtained by TE/TM decomposition, and that they were verified against 2-D method of moment solutions for TE and TM cases separately. The results are shown in Figure 2. We see that the DB boundary behaves exactly as a soft surface for the two incidences. For normal incidence, the longitudinal PEC/PMC strips define a soft surface, and for grazing incidence, the circumferential strips do.

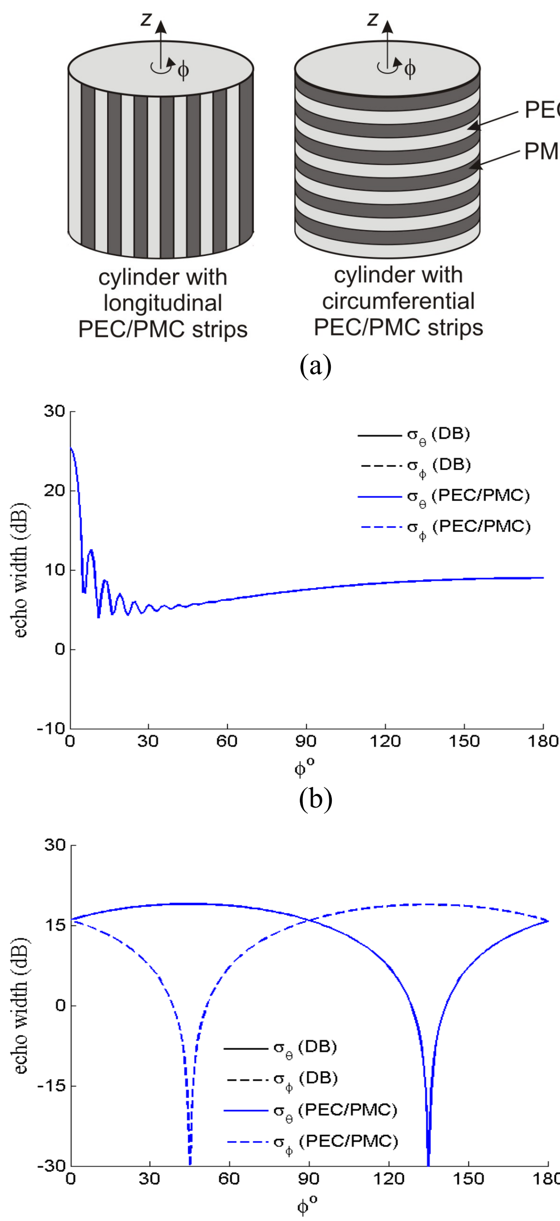

Fig. 2. Echo width of the circular cylinder with geometry shown in (a) for TE and TM cases, i.e. σ_ϕ and σ_θ, respectively. The DB boundary condition is compared with (b) longitudinal PEC/PMC strips forming a circular cylinder due to normal plane wave incidence, and (c) circumferential PEC/PMC strips forming a circular cylinder due to grazing plane wave incidence. Curves not seen explicitly coincide identically with their counterpart. Note that the undefined DB boundary conditions for normal incidence were neglected in these results.

In order to compare the DB boundary conditions to a realistic EBG surface we computed the scattering from a cylindrical mushroom surface by using CST Microwave Studio [15]. The dimensions of the mushroom structure are w = 2.25 mm, P = 2.4 mm, t = 1.6 mm, ε_r = 2.2 and the vias diameter is 0.36 mm. The frequency is 12 GHz and the radius of the PEC cylinder is 20 mm. The results are shown in Figs. 3b and c, and we see that there is quite good agreement between the CST results for the practical surface and the series solution for the DB surface.

We have also calculated the equivalent blockage width for this DB surface case (Figs. 3d and 3e). The equivalent blockage width (W_{eq}) is a complex-valued parameter (introduced in [5]) that represents the width of an ideal shadow which produces the same forward-scattered field as the cylinder that is being observed (in our case, a DB cylinder). Only the real part of W_{eq} is considered here ($\mathrm{Re}(W_{eq})$). The parameter similar to the equivalent blockage width is the scattering cross section per unit length (SCS). It is defined as a ratio of power density of all scattered spatial harmonics and the intensity of the incident Poynting vector. Both the W_{eq} and SCS are the quantities that actually show how wide the cylinder appears for the electromagnetic waves. For lossless scatterers the SCS is equal to $2\cdot\mathrm{Re}(W_{eq})$ according to the forward scattering theorem, being discussed also in [5]. This relation was verified by computation of both SCS and W_{eq} to be satisfied also for cylinders described with DB boundary conditions, therefore there is no leakage of energy present. However, this non-existing leakage problem is in the present case due to the fact that we did not account for the special normal incidence, thereby avoiding that the DB boundary conditions are not defined for normal incidence.

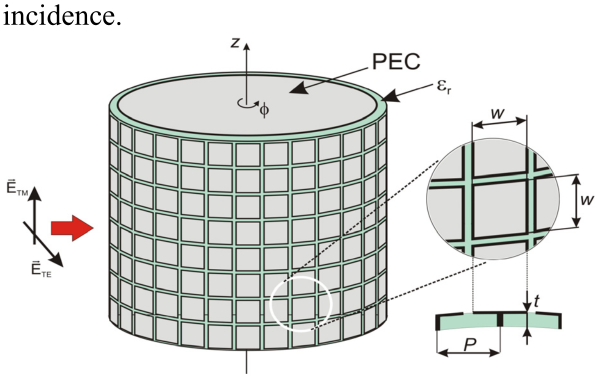

(a) Geometry

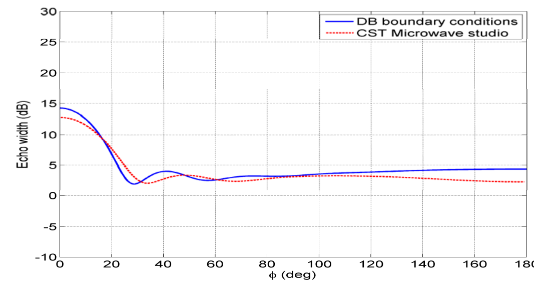

(b) Echo width for TM polarization at 12 GHz

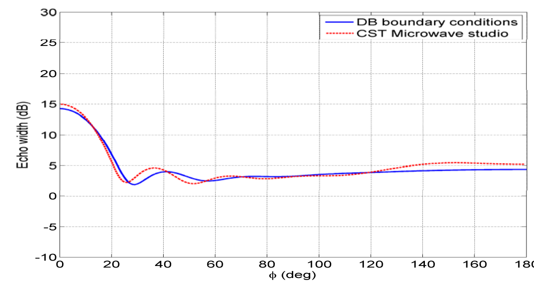

(c) Echo width for TE polarization at 12 GHz

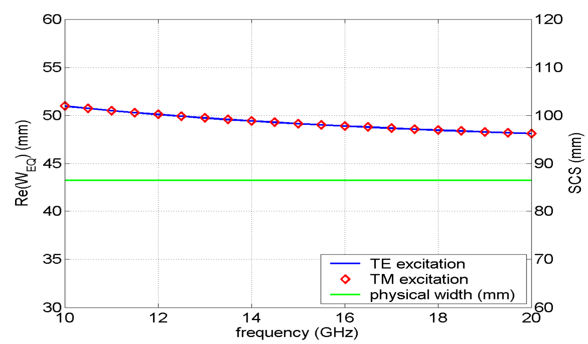

(d) Equivalent blockage width and SCS as a function of frequency for ideal DB cylinder

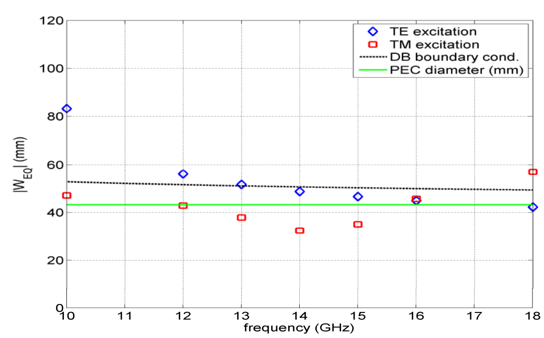

(e) Equivalent blockage width of ideal DB cylinder and EBG mushroom cylinder (TE and TM polarizations computed using CST Microwave Studio)

Fig. 3. Results for ideal DB cylinder (neglecting normal incidence problem) compared to results for EBG mushroom cylinder obtained by CST Microwave Studio.

V. RADIATION FROM DIPOLE OVER EBG GROUND PLANE

In order to investigate properties of the DB boundary conditions further we consider radiation from a horizontal dipole over a planar EBG surface (see Fig. 4a). Using the plane-wave spectral-domain method in the same way as in [18]-[19], it is easy to determine the Green's functions of the DB boundary, see the Appendix. The G_{xx} component of the dyadic Green's function becomes

$$\tilde{G}_{xx}(z>h) = -\frac{\eta_0 k_x^2 k_z^2 \cos(k_z h) + j\eta_0 k_0^2 k_y^2 \sin(k_z h)}{\beta^2 k_0 k_z} e^{-jk_z z}\tilde{J}_x \quad (2)$$

and equivalently for the other components. From this, the far-field radiation pattern of the horizontal dipole can be determined and is plotted in Fig. 4b.

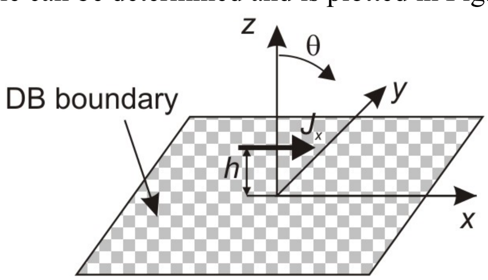

(a) Geometry

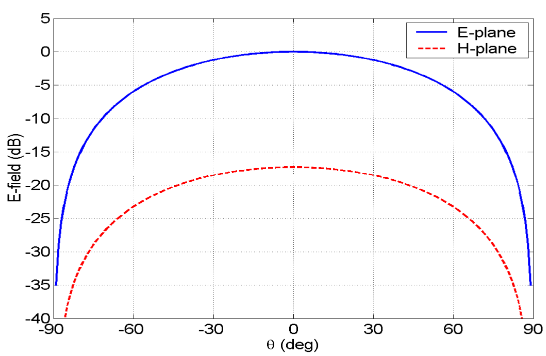

(b) Far-field radiation pattern

Fig. 4. Horizontal dipole over original DB boundary.

The working frequency is 12 GHz, and the short dipole is located 0.5 mm above the DB boundary. It can be seen that the E-plane and the H-plane do not match at all for $\theta = 0^\circ$, which is wrong as E-plane and H-planes coincide for $\theta = 0^\circ$. This is therefore an anomaly produced by the the DB boundary condition not being defined for $\theta = 0^\circ$. The explanation to the particular results still achieved is given below. In the E-plane (i.e. for $k_y = 0$), the structure is equal to the x-directed dipole over the transverse (y-directed) PEC/PMC strips [18]. For the specific case $k_y = 0$, corresponding to $\theta = 0^\circ$, we obtain

$$\tilde{G}_{xx}(z>h) = -\frac{\eta_0 k_z \cos(k_z h)}{k_0} e^{-jk_z z}\tilde{J}_x \quad \text{for} \quad k_y = 0 \quad (3)$$

The same Green's functions are obtained in [18] where the Green's functions of a dipole over the PEC/PMC strips surface are derived. However, in the H-plane ($k_x = 0$) we have the x-directed source over the x-directed PEC/PMC strips, which is the same situation as the horizontal dipole over the PEC plane (since the x-component of H-field is zero, the H-field "does not see" the PMC strips). The corresponding Green's function is simply

$$\tilde{G}_{xx}(z>h) = -\frac{j\eta_0 k_0 \sin(k_z h)}{k_z} e^{-jk_z z}\tilde{J}_x \quad \text{for} \quad k_x = 0 \quad (4)$$

We readily see that these two values are not equal for $\theta = 0^\circ$, i.e. when $k_z = k$, thus the anomalous behavior appears.

A. The amended DB boundary

The EM waves that are excited by the horizontal dipole can be represented as a sum of TM and TE plane waves. The problem with the TE waves is that they "feel" that the EBG surface acts as a PEC structure, which is not correct for angles close to normal incidence. We will now first use a more general form of the amended DB boundary condition than that in (1), i.e.

$$H_n + \alpha \cdot H_l = 0, \quad (5)$$

where H_n and H_l denote the normal and the longitudinal component of the magnetic field, respectively, and α is a coefficient (still to be determined). Since the direction of propagation can be determined from k_x and k_y spectral variables, the normal and longitudinal components of the magnetic field are simply

$$H_n = H_z, \qquad H_l = \frac{k_x}{\beta} H_x + \frac{k_y}{\beta} H_y. \quad (6)$$

Only the TE polarized wave is of interest (reflection of TM waves is described with the boundary condition $E_z = 0$). Without losing generality let us assume that the wave is propagating in the y-direction, and that θ is the angle of incidence (θ is angle towards z-axis). Therefore, we can write

$$\begin{aligned} k_x &= 0, \\ k_y &= k_0 \cdot \sin\theta, \\ k_z &= k_0 \cdot \cos\theta. \end{aligned} \tag{7}$$

The TE wave can be described with (R is the reflection coefficient)

$$H_z = e^{jk_z z} + R \cdot e^{-jk_z z}\ , \tag{8}$$

and consequently at $z = 0$ we can now write $H_z = 1 + R$. The y-component of the H-field is equal to

$$H_y = -\frac{jk_y}{\beta^2}\frac{\partial}{\partial z}H_z = -\frac{j}{k_y}\frac{\partial}{\partial z}H_z, \tag{9a}$$

$$H_y = \frac{k_z}{k_y}\left(e^{jk_z z} - R \cdot e^{-jk_z z}\right), \tag{9b}$$

and again at $z = 0$ we obtain $H_y = (k_z/k_y)(1 - R)$. The modified DB boundary condition is now equal:

$$\left(1+R\right) + \alpha \cdot \frac{k_z}{k_y} \cdot (1-R) = 0. \tag{10}$$

Therefore, the reflection coefficient is equal:

$$R = -\frac{1+\alpha \cdot k_z/k_y}{1-\alpha \cdot k_z/k_y}. \tag{11}$$

Since we are considering reflection from a surface, we expect $|R| = 1$. Therefore, the only way that $|R| = 1$ for all incidence angles is that α is purely imaginary number. We will simply define coefficient α as $\alpha = -j$. Note that the value of the reflection coefficient is now $R = +1$ for $\theta = 0^o$ (PMC for normal incidence) and $R = -1$ for $\theta = 90^o$ (PEC for grazing incidence, i.e. soft surface for grazing incidence). We have already in (1) referred to this special choice of $\alpha = -j$ as the PMC-amended DB boundary condition.

The far-field radiation pattern of a horizontal dipole over a surface described with the corrected DB boundary conditions is given in Fig. 5. Like in the previous case, the working frequency is 12 GHz, and the short dipole is located 0.5 mm above the DB boundary. It can be seen that there now is no problem with singularity at $\theta = 0^\circ$, i.e. the E-plane and the H-plane now match each other at $\theta = 0^\circ$. Furthermore, the radiation pattern reveals that the surface acts as a PMC for angles around normal incidence and that it stops propagating waves for angles close to grazing incidence.

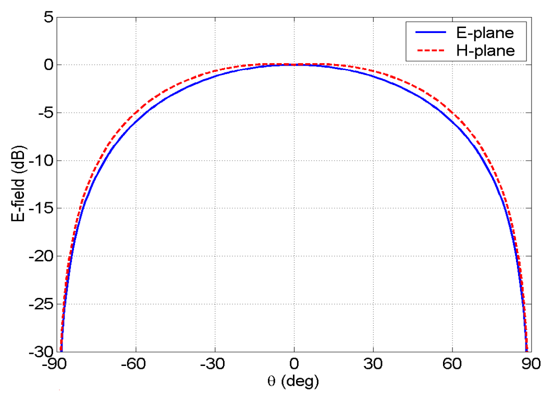

Fig. 5. Far-field radiation pattern of a horizontal dipole over a surface described with PMC-amended DB boundary conditions.

Figure 6 shows comparison of the radiation pattern of the short dipole over the EBG surface realized by the same mushroom structure as in the previous case in Section IV. The working frequency is 12 GHz, i.e. the considered frequency is in the beginning of the stop band which is between 11 and 15 GHz. It can be seen that there is a good agreement between the results for the mushroom structure (modeled with the CST Microwave Studio) and for the canonical EBG surface (modeled with the PMC-amended DB boundary condition) at the best frequency of 12 GHz in the beginning of the bandgap. The frequency dependences of the radiation patterns calculated with both, amended DB boundary conditions and CST, which clearly show that the matching is the best at 12GHz, are shown in Fig. 7. One should note that the considered structures when performing CST calculations were finite and therefore small ripples can be seen due to internal reflection and diffraction from the edges of the structure.

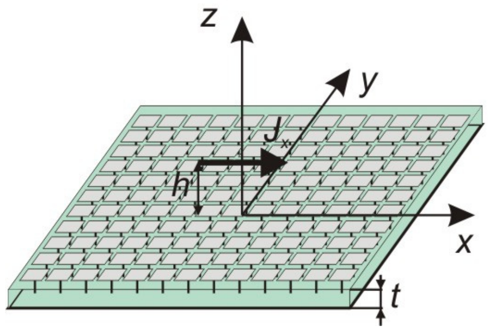

(a) Geometry

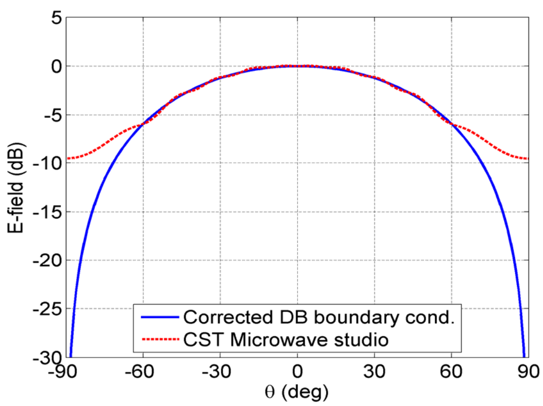

(b) E-plane

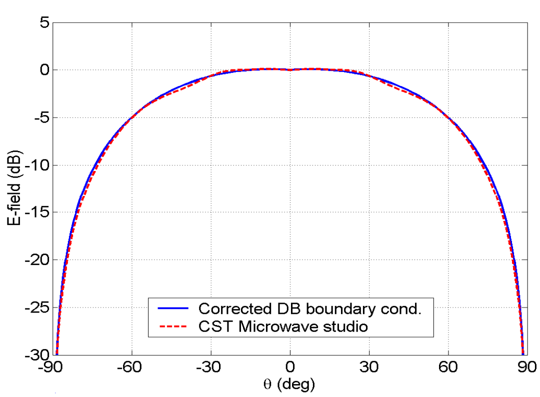

(c) H-plane

Fig. 6. Far-field radiation pattern of a horizontal dipole over the PMC-amended DB and EBG surfaces at 12 GHz.

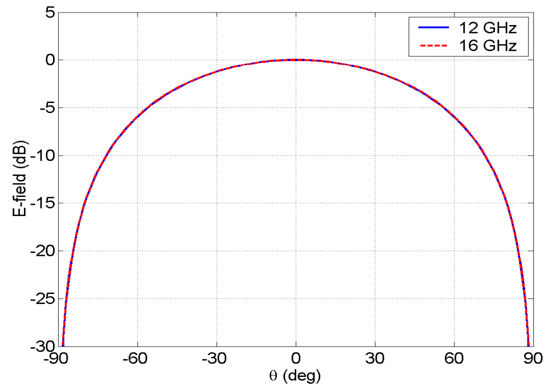

(a) E-plane calculated with PMC-amended DB boundary conditions.

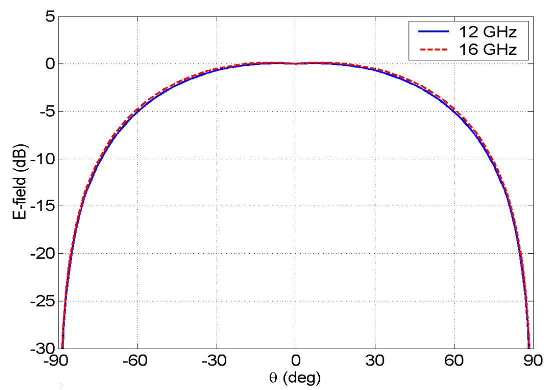

(b) H-plane calculated with PMC-amended DB boundary conditions.

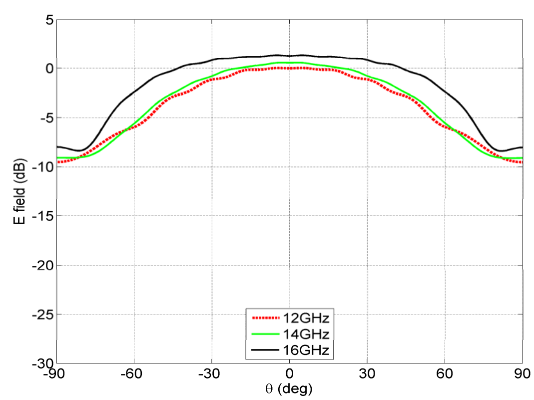

(c) E-plane calculated with CST Microwave Studio.

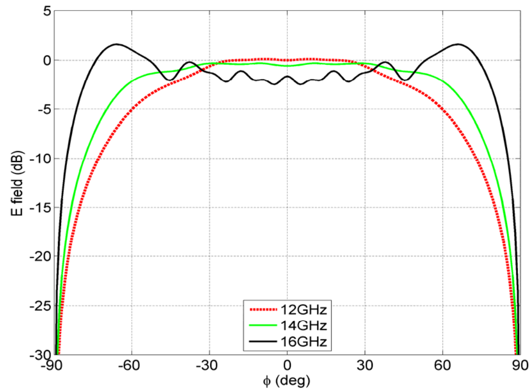

(d) H-plane calculated with CST Microwave Studio.

Fig. 7. Frequency dependence of the far field radiation pattern for the case of a dipole over planar EBG surface.

VI. RADIATION FROM A DIPOLE OVER A CYLINDRICAL PERIODIC STRUCTURE

We would also like to determine how the curvature of the surface influences both the original DB and the PMC-amended DB boundary conditions. In order to do that, we have investigated the radiation of an axially oriented dipole over the cylindrical EBG surface. The problem is described in the classical cylindrical coordinate system: the dipole is z-directed and the surface is described with its radius (we have considered the structure with radius r_{DB} = 21.6 mm). The working frequency is 12 GHz and the dipole height over the DB boundary is 0.5 mm. The problem is analyzed using the spectral-domain approach, similarly to the planar case (the details can be found in [19]). The obtained radiation pattern is shown in Fig. 8. It can be seen that there is no problem with singularities for the direction normal to the structure ($\theta = 90^\circ$ and $\phi = 0^\circ$ for the considered structure), i.e. both E-plane and H-plane patterns match in that direction. However, the radiation pattern is not the one we would expect from a dipole over an EBG surface. In more details, the PEC component of the DB boundary prevails over the PMC component, i.e. for the direction normal to the structure the structure acts more like a PEC.

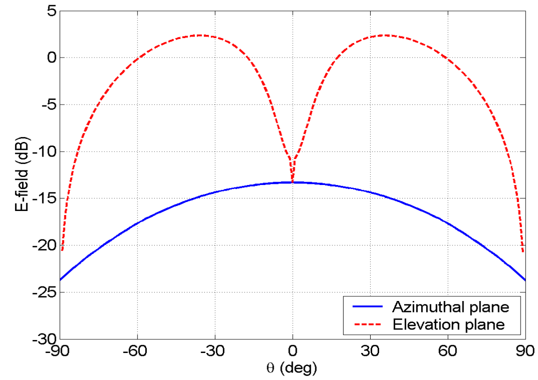

Fig. 8. Far-field radiation pattern of an axially-directed dipole over the cylindrical original DB boundary.

If we apply the PMC-amended DB boundary conditions (defined with the equation (1)), the situation is quite different. In order to compare the DB boundary with a realistic EBG surface we have used the same EBG structure like in the previous case; the working frequency is again 12 GHz. In Fig. 9 we have compared the radiation patterns obtained with corrected DB boundary conditions and with the CST Microwave Studio. It can be seen that the agreement is very good, i.e. the PMC-amended DB boundary condition works very well in describing the main and desired characteristics of the EBG surface. Naturally this is only valid inside the frequency band where the considered structure has a bandgap property. This is clearly seen by viewing Fig. 10 which shows the frequency dependence of this structure, calculated using CST Microwave Studio.

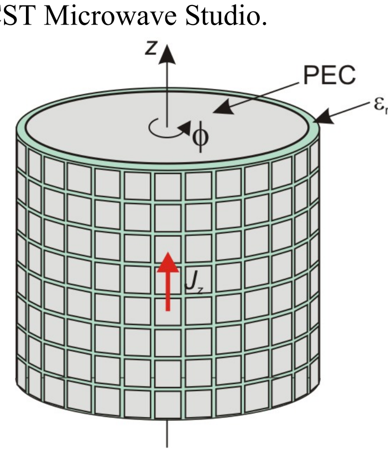

(a) Geometry

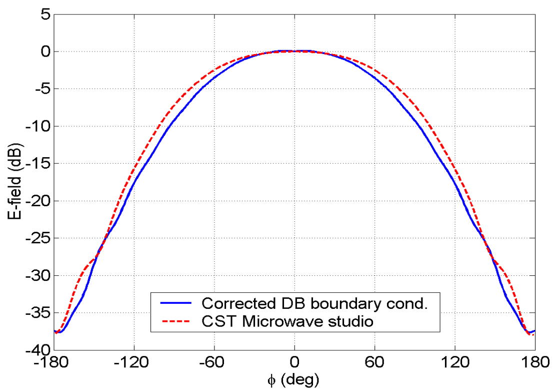

(b) Axially-directed dipole

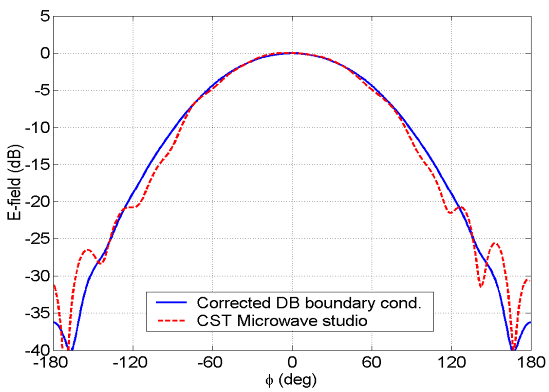

(c) Circumferentially-directed dipole

Fig. 9. Far-field radiation pattern in the azimuth plane of a dipole over the cylindrical PMC-amended DB with EBG surfaces at 12 GHz.

VII. CONCLUSIONS

The paper has summarized previously defined canonical surfaces for use in electromagnetic computations and conceptual studies. The PEC is well accepted and quite extensively used. A similar situation exists for the PMC case, at least in theoretical work and as symmetry planes in EM computations. However, in most computational codes the PMC cannot be used for finite and arbitrary shapes and it cannot be curved. The authors hope that this overview can stimulate software vendors and developers to include arbitrarily shaped PMCs in their codes. This is easily done and will add important capabilities. Similarly, it would be useful if arbitrarily shaped PEC/PMC strip grids with arbitrary strip orientations could be included for general usage. The PEC/PMC strip grids represent soft and hard surfaces and can open up for more fundamental studies and principally new hardware solutions. The PEC/PMC strip grid is also easy to implement as illustrated in [8].

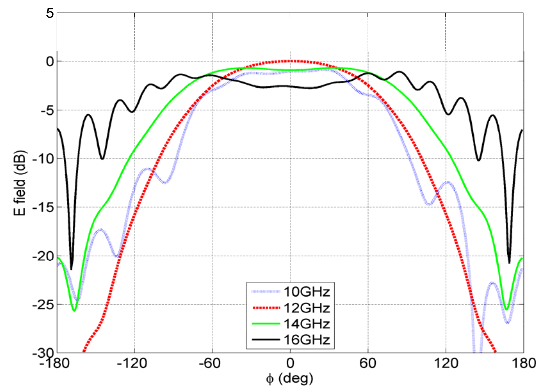

(a) Axial dipole case

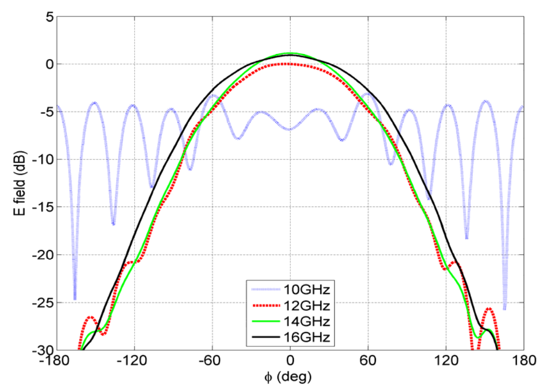

(b) Circumferential dipole case

Fig. 10. Frequency dependence of the far field radiation pattern for the case of a dipole over cylindrical mushroom EBG surface (calculated using CST Microwave Studio).

The newly introduced DB boundary has characteristics similar to an ideal EBG surface, i.e. an isotropic soft surface, but the present paper has highlighted some anomalies that need to be resolved by more research before they can be used in general codes. For a new canonical surface to be meaningful we must require that it is simple and general, and has interesting and useful characteristics. We have proposed a simple amendment in equation (1), referred to as the PMC-amended DB boundary, that seems to work, but it is limited in the sense that it requires knowledge of the propagation direction of the waves along the surface. This limitation is not severe when applied in analytical and semi-analytical modeling like in the present paper. However, for use in general 3-D Moment Method, FDTD and FEM based field solvers a more general amendment is needed.

There is also the previously introduced so-called D′B′ boundary, but this has no known practical counterpart and therefore there is no particular interest for this surface at the moment. The D′B′ boundary suffers from a similar anomaly as the DB boundary and also needs to be corrected.

ACKNOWLEDGMENT

The authors are thankful for fruitful discussions with Stefano Maci, Ismo Lindell, and Ari Sihvola.

APPENDIX

The sketch of the structure is given in Fig. 3. The normal EM field component has a form:

$$\begin{aligned}\tilde{E}_z &= A e^{-jk_z(z-d)} \\ H_z &= B e^{-jk_z(z-d)}\end{aligned} \quad \text{for } z \ge d \qquad \text{(A1a)}$$

$$\begin{aligned}\tilde{E}_z &= C\cos(k_z z) + D\sin(k_z z) \\ \tilde{H}_z &= E\cos(k_z z) + F\sin(k_z z)\end{aligned} \quad \text{for } 0 \le z \le d \qquad \text{(A1b)}$$

The transverse components can be calculated as:

$$\tilde{E}_x = -\frac{jk_x}{\beta^2}\frac{\partial \tilde{E}_z}{\partial z} - \frac{\eta_0 k_0 k_y}{\beta^2}\tilde{H}_z \qquad \text{(A2a)}$$

$$\tilde{E}_y = -\frac{jk_y}{\beta^2}\frac{\partial \tilde{E}_z}{\partial z} + \frac{\eta_0 k_0 k_x}{\beta^2}\tilde{H}_z \qquad \text{(A2b)}$$

$$\tilde{H}_x = -\frac{jk_x}{\beta^2}\frac{\partial \tilde{H}_z}{\partial z} + \frac{k_0 k_y}{\eta_0\beta^2}\tilde{E}_z \qquad \text{(A2c)}$$

$$\tilde{H}_y = -\frac{jk_y}{\beta^2}\frac{\partial \tilde{H}_z}{\partial z} - \frac{k_0 k_x}{\eta_0\beta^2}\tilde{E}_z \qquad \text{(A2d)}$$

$$\beta^2 = k_x^2 + k_y^2 . \qquad \text{(A2e)}$$

The DB boundary conditions at $z = 0$ straightforwardly define two out of six unknowns:

$$E_z = H_z = 0 \qquad \text{(A3a)}$$

$$\Rightarrow \quad C = E = 0 . \qquad \text{(A3b)}$$

The remaining four boundary conditions are:

$$\begin{aligned}\tilde{E}_x^+ - \tilde{E}_x^- &= 0 \\ \tilde{E}_y^+ - \tilde{E}_y^- &= 0 \\ \tilde{H}_x^+ - \tilde{H}_x^- &= 0 \\ \tilde{H}_y^+ - \tilde{H}_y^- &= -\tilde{J}_x\end{aligned} \quad \text{at } z = h. \qquad \text{(A4)}$$

The four equations with four unknowns are “easily” analytically solved giving the following results:

$$\begin{aligned}A &= \frac{\eta_0}{k_0}k_x\cos(k_z h)\,\tilde{J}_x \\ B &= j\frac{k_y}{k_z}\sin(k_z h)\,\tilde{J}_x \\ D &= -j\frac{\eta_0}{k_0}k_x e^{-jk_z h}\,\tilde{J}_x \\ F &= j\frac{k_y}{k_z}e^{-jk_z h}\,\tilde{J}_x .\end{aligned} \qquad \text{(A5)}$$

From here it is easy to derive all EM field components using equations (A1) and (A2). For example, the E_x component is equal to

$$\tilde{G}_{xx}(z>h) = -\frac{\eta_0 k_x^2 k_z^2\cos(k_z h) + j\eta_0 k_0^2 k_y^2\sin(k_z h)}{\beta^2 k_0 k_z}e^{-jk_z z}\,\tilde{J}_x . \qquad \text{(A6)}$$

REFERENCES

[1] P.-S. Kildal, “Artificially Soft and Hard Surfaces in Electromagnetics,” *IEEE Trans. Antennas Propagat.*, Vol. 38, pp. 1537-1544, Oct. 1990.

[2] P.-S. Kildal and A. Kishk, “EM Modeling of Surfaces with STOP or GO Characteristics - Artificial Magnetic Conductors and Soft and Hard Surfaces,” *Applied Computational Electromagnetics Society Journal*, vol. 18, pp. 32-40, Mar. 2003.

[3] V. Lindell and A. H. Sihvola, “Electromagnetic Boundary and its Realization with Anisotropic Metamaterial,” *Physical Review E 79*, 026604, 2009.

[4] D. Sievenpiper, L. J. Zhang, R. F. J. Broas, N. G. Alexopolous, and E. Yablonovitch, “High-Impedance Electromagnetic Surfaces with a

Forbidden Frequency Band," *IEEE Transactions on Microwave Theory and Techniques*, vol. 47, pp. 2059-2074, Nov. 1999.

[5] P.-S. Kildal, A. Kishk, and A. Tengs, "Reduction of Forward Scattering from Cylindrical Objects using Hard Surfaces," *IEEE Trans. Antennas Propagat*., vol. 44, pp. 1509-1520, Nov. 1996.

[6] P.-S. Kildal, A. Kishk, and Z. Sipus, "RF Invisibility using Metamaterials: Harry Potter's Cloak or the Emperor's New Clothes?," *2007 IEEE International Symposium on Antennas and Propagation* (APS), Hawaii, 10-15 June 2007.

[7] P.-S. Kildal, A. A. Kishk, and S. Maci, "Special Issue on Artificial Magnetic Conductors, Soft/Hard Surfaces, and Other Complex Surfaces" (Guest Editors), *IEEE Transactions on Antennas and Propagation*, vol. 53, pp. 2-7, Jan. 2005.

[8] Ahmed Kishk and Per-Simon Kildal, "Modeling of Soft and Hard Surfaces using Ideal PEC/PMC Strip Grids," *IET Microwaves, Antennas & Propagation*, vol. 3, pp. 296–302, Mar. 2009.

[9] P.-S. Kildal, E. Alfonso, A. Valero-Nogueira, and E. Rajo-Iglesias, "Local Metamaterial-Based Waveguides in Gaps between Parallel Metal Plates," *IEEE Antennas and Wireless Propagation Letters* (AWPL), vol. 8, pp. 84-87, 2009.

[10] A. Valero-Nogueira, E. Alfonso, J. I. Herranz, and P.-S. Kildal, "Experimental Demonstration of Local Quasi-TEM Gap Modes in Single-Hard-Wall Waveguides," *IEEE Microwave and Wireless Components Letters*, vol. 19, pp. 536-538, Sept. 2009.

[11] M. Ng Mou Kehn and P.-S. Kildal, "Miniaturized Rectangular Hard Waveguides for use in Multi-Frequency Phased Arrays," *IEEE Transactions on Antennas and Propagation*, vol. 53, pp. 100-109, Jan. 2005.

[12] M. Ng Mou Kehn, M. Nannetti, A. Cucini, S. Maci, and P.-S. Kildal "Analysis of Dispersion in Dipole-FSS Loaded Hard Rectangular Waveguide," *IEEE Transactions on Antennas and Propagation*, vol. 54, pp. 2275-2282, Aug. 2006.

[13] E. Rajo-Iglesias, A. Uz Zaman, and P.-S. Kildal, "Parallel Plate Cavity Mode Suppression in Microstrip Circuit Packages using a Lid of Nails," *IEEE Microwave and Wireless Components Letters*, vol. 20, no. 1, pp. 31-33, Jan. 2010.

[14] M. A. Kishk, A. A. Kishk, and P.-S. Kildal, "Electromagnetic Scattering from Circular Cylinders with PEC/PMC Boundaries," *2010 IEEE International Symposium on Antennas and Propagation*, Toronto, July 11-17, 2010.

[15] P.-S. Kildal, A. A. Kishk, and Z. Sipus, "Introduction to Canonical Surfaces in Electromagnetic Computations: PEC, PMC, PEC/PMC Strip Grid, DB Surface," *The 26th Annual Review of Progress in Applied Computational Electromagnetics*. Tampere, Finland, pp. 514-519, April 26-29, 2010.

[16] CST Microwave Studio 2010, www.cst.com.

[17] I. V. Lindell, and A. H. Sihvola, "Uniaxial IB-Medium Interface and Novel Boundary Conditions," *IEEE Transactions on Antennas and Propagation*, vol. 57, pp. 694-700, Mar. 2009.

[18] Z. Sipus, H. Merkel, and P.-S. Kildal, "Green's Functions for Planar Soft and Hard Surfaces Derived by Asymptotic Boundary Conditions," *IEE Proceedings - Microwaves, Antennas and Propagation*, vol. 144, pp. 321-328, Oct. 1997.

[19] Z. Sipus, P.-S. Kildal, R. Leijon, and M. Johansson, "An Algorithm for Calculating Green's Functions of Planar, Circular Cylindrical and Spherical Multilayer Substrates," *Applied Computational Electromagnetics Society Journal*, vol. 13, no. 3, pp. 243-254, 1998.

Miniature Printed Magnetic Photonic Crystal Antennas Embedded into Vehicular Platforms

Erdinc Irci, Kubilay Sertel, and John L. Volakis

ElectroScience Laboratory, Department of Electrical & Computer Engineering
The Ohio State University, 1320 Kinnear Rd. Columbus, OH 43212, USA
ircie@ece.osu.edu, sertel@ece.osu.edu, volakis@ece.osu.edu

Abstract - In this paper, a miniature printed antenna utilizing magnetic photonic crystal (MPC) modes is presented. Typically, MPC modes are supported by a combination of anisotropic dielectric and ferrimagnetic layers. Here, these modes are emulated using coupled printed lines on a grounded dielectric substrate with small, biased ferrimagnetic inclusions. The resonant antenna is formed by cascading two unit cells excited with a probe feed. A recessed, cavity-backed version of this antenna is embedded into a vehicular platform with a goal to minimize platform effects. Several locations on the vehicle are studied and antenna placement is optimized using a combination of two commercially available electromagnetic simulators.

Index Terms - Anisotropic media, coupled microstrip lines, degenerate band edge (DBE) crystals, magnetic photonic crystals (MPC), metamaterials, miniature antennas, embedded antennas, vehicular antennas.

I. INTRODUCTION

Conventional military ground vehicles usually end up being populated with many protruding antennas, making them vulnerable targets. Thus, when installing antennas on such vehicular platforms, a typical objective is to reduce their profile and decrease their radar signature, while maintaining the performance delivered by protruding antennas. However, for multipurpose military ground vehicles, antenna installation is even more challenging due to limited areas for placement. More specifically, the large conducting surfaces found on the hood and roof cannot be used due to other utilities (such as weapon installments, spare tires, supplies, and personnel transportation). Therefore, antennas need be placed (still conformally) towards the edges of vehicle roof, doors, bumpers, and windows frames. These restrictions place additional challenges for designing antennas that are less susceptible to nearby structure effects. Such platform effects must be reduced to suppress the need for antenna retuning when installed. In this paper, we introduced a cavity-backed (slot type) antenna that remains stable even when placed within 1.5″ (3.81cm) of the vehicle's edges.

The proposed miniature antenna is based on modes found in periodic stacks of misaligned dielectric layers, similar to those shown in Fig. 1(a)-left. These novel modes were referred to as degenerate band edge (DBE) and magnetic photonic crystal (MPC) modes [1-3]. Extreme wave slow down at much lower frequencies was harnessed for realizing miniaturized and highly directive antennas [4-6]. More recently, the misaligned anisotropic dielectric layers in these volumetric crystals were successfully emulated by a combination of uncoupled and coupled microstrip line sections on uniform substrates; see Fig. 1(a)-right. The DBE modes emulated using such coupled lines enabled miniature, high gain microstrip antennas [7]. Specifically, the maximally flat dispersion curves of DBE crystals, shown in Fig. 1(b)-left, allowed for significant miniaturization over microstrip loop and patch antennas. However, the zero slope associated with the K = π resonance at the band edge suffers from reduced bandwidth. As a remedy, in this paper we introduce biased ferrimagnetic inclusions at the coupled line sections to obtain nonreciprocal MPC dispersion modes. As depicted in Fig. 1(b)-right, nonzero slope is realized in the dispersion curve around K = π point. This implies improved miniaturization and bandwidth enhancement.

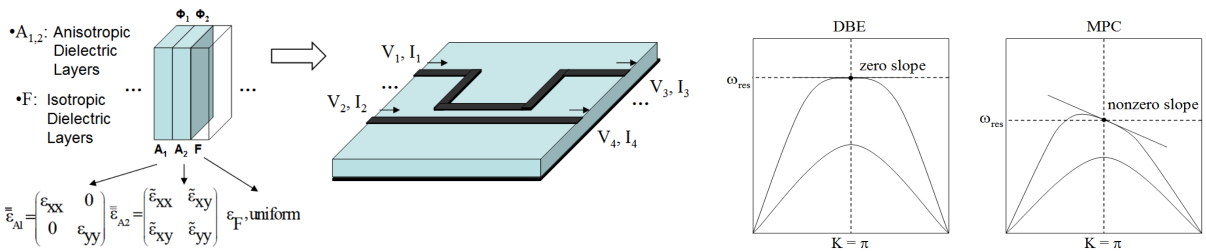

(a) (b)

Fig. 1. (a) Coupled lines emulating anisotropy in a DBE unit cell. (b) DBE and MPC dispersion diagrams.

II. MPC ANTENNA DESIGN AND PERFORMANCE

Previously, DBE dispersion modes were emulated in [7] using uncoupled and coupled line sections on a uniform dielectric substrate, as shown in Fig. 2(a)-top. The uncoupled sections were bent inwards to attain a compact footprint. For emulating nonreciprocal MPC modes, small biased ferrimagnetic inclusions were inserted under coupled line sections, as depicted in Fig. 2(a)-bottom [8]. The corresponding dispersion curves of these DBE and MPC unit cells are shown in Fig. 2(b). Next, DBE and MPC antennas were formed by circularly cascading two unit cells, as depicted in Fig. 3(a). A coaxial probe feed and a small microstrip stub were also used to capacitively excite these DBE and MPC elements. As illustrated in Fig. 3(b), for the MPC case, ferrimagnetic inclusions under the coupled lines extend down to ground plane level and small magnets placed underneath provide the necessary DC magnetic bias. A rectangular patch antenna was also designed for comparison purposes. In all antennas, the same 2″×2″×0.5″ (5.08cm×5.08cm×1.27cm) dielectric substrates with 2″×2″ (5.08cm×5.08cm) ground planes were used. MPC antenna in Fig. 3(a) with 0.8″×0.87″ (2.03cm×2.21cm) footprint resonates at 2.35 GHz, having 8.8% bandwidth and 6.2 dB realized gain. DBE antenna with a 0.97″×0.99″ (2.46cm×2.51cm) footprint resonates at the same frequency, having 6.9% bandwidth and 6.5 dB gain. Patch antenna at the same frequency has 11.6% bandwidth and 6.7 dB gain, by utilizing a much larger footprint of 1.23″×1.14″ (3.12cm×2.9cm). Hence, MPC antenna is 28% smaller than the DBE and 50% smaller than the patch (in terms of footprint area). Although much smaller in footprint size, MPC antenna maintains almost same bandwidth and gain as the patch. The substantial footprint reduction obtained by the MPC antenna suggests that its substrate size can be further reduced without much degradation in performance. This is explored in the next section when a cavity-backed configuration is considered.

A prototype of the MPC antenna in Fig. 3(a) was also fabricated and is shown at the inset of Fig. 4(a). The antenna substrate was formed using four layers of 125 mil thick Rogers Duroid 5880 dielectrics and was fastened using two plastic ribbons. The ferrimagnetic insertions (NG-1001 CVG of TCI Ceramics: $4\pi M_s$ = 976G, ΔH = 7Oe, ε_r = 14.2 and $\tan\delta_d = 1\times10^{-4}$) were inserted into two rectangular holes in each dielectric layer. To bias the antenna, two small permanent magnets (1″×1/2″×1/16″: 2.54cm×1.27cm ×1.59mm) were placed underneath the ground plane. Its measured return loss is plotted in Fig. 4(a). As seen, this prototype delivered 9.1% bandwidth around 2.35 GHz and showed very good agreement with the 8.8% computed bandwidth at around the same frequency.

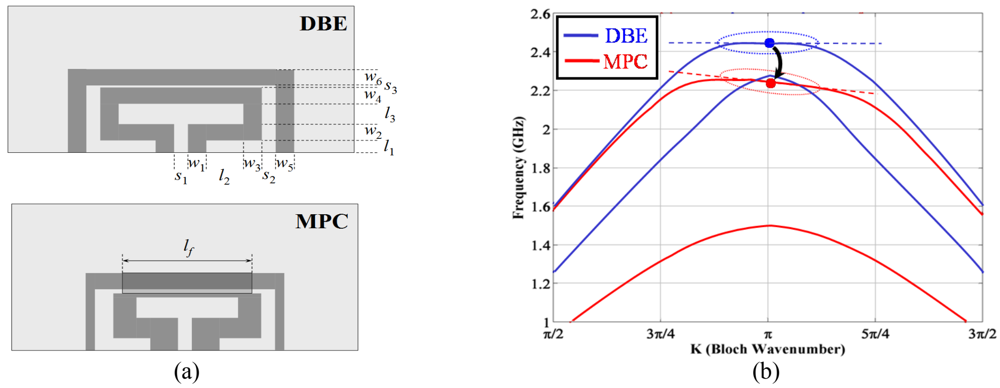

Fig. 2. (a) Layout of DBE and MPC unit cells. (b) DBE and MPC dispersion diagrams.

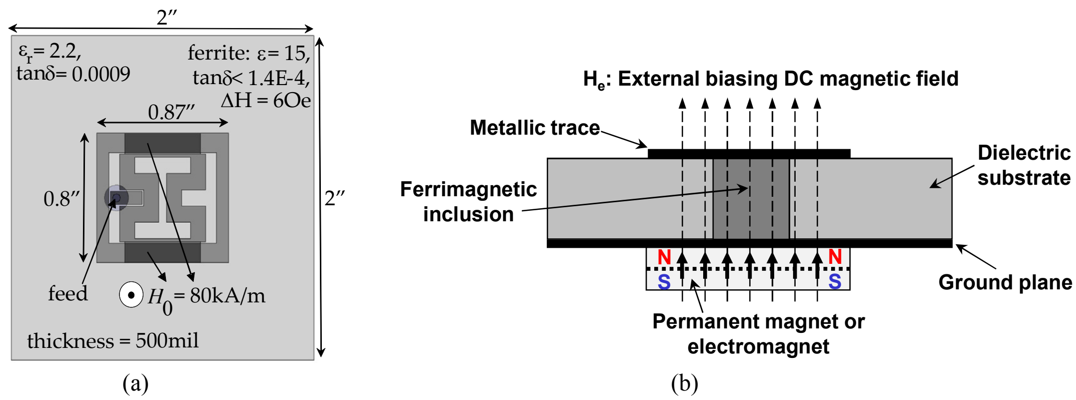

Fig. 3. (a) Resonant MPC antenna formed by circularly cascading two unit cells. (b) Practical realization of MPC modes using ferrimagnetic inclusions and DC magnetic bias.

The broadside realized gain of the fabricated MPC prototype was measured in the anechoic chamber. From Fig. 4(b), we observe a peak realized gain of 4.5 dB (70% efficiency) at 2.35 GHz. This is 1.3 dB smaller than the 5.8 dB computed gain (90% efficiency), which included all magnetic, dielectric and conductivity losses. This difference is attributed to non-uniform bias field inside the ferrimagnetic inclusions. The measured 4.5 dB realized gain is obtained when the MPC is in receiving (Rx) mode. Due to nonreciprocal behavior, its gain is 3.5 dB in transmit (Tx) mode. An opposite nonreciprocal behavior (i.e. Rx = 3.5dB, Tx = 4.5dB) is obtained by reversing the polarization of DC magnetic bias, show in Fig. 4b-left, top.

The realized gain of the unbiased MPC antenna (in the absence of biasing magnets, shown in Fig. 4b-left, bottom) was also measured. As seen in Fig. 4(b), the unbiased MPC has -1.25 dB gain at 2.35 GHz, which is 5.75dB less than the biased case. This demonstrates that the MPC can be effectively switched on/off by toggling the magnetic bias.

III. CAVITY-BACKED MPC ANTENNA

Next, we considered a 1.5″×1.5″×0.5″ (3.81cm×3.81cm×1.27cm) substrate. In addition, the MPC antenna is recessed below the ground plane by embedding it in a metallic cavity, as shown in Fig. 5(a). Consequently, a small and zero-profile aperture is created on the ground plane. The small size and flush mounting of the MPC antenna makes it suitable for installation at corners, edges, and vertical surfaces of the vehicle, while it is less susceptible to nearby effects. Since the ground plane sizes at such locations are varying, one undesirable effect is detuning of antenna resonance. We note that the recessed MPC antenna also mitigates such platform loading effects. When a 3″×3″ (7.62cm×7.62cm) ground plane is used, the MPC antenna resonates at 2.45 GHz with 3% bandwidth. As the ground plane size is made much larger (e.g., 10″×10″=25.4cm×25.4cm or infinite), the resonance slightly shifts to 2.42 GHz, while still keeping the 3% bandwidth, see Fig. 6 (a). In addition, these small detunings can be prevented by slightly tuning the magnetic bias, see Fig. 6 (b). For all cases, the broadside radiation pattern of the antenna is retained almost the same, as can be observed from Fig. 5 (b). The main differences in radiation patterns are observed in back lobes, which are small. With this cavity-backed design, we next proceed to investigate the antenna performance on a representative automobile platform.

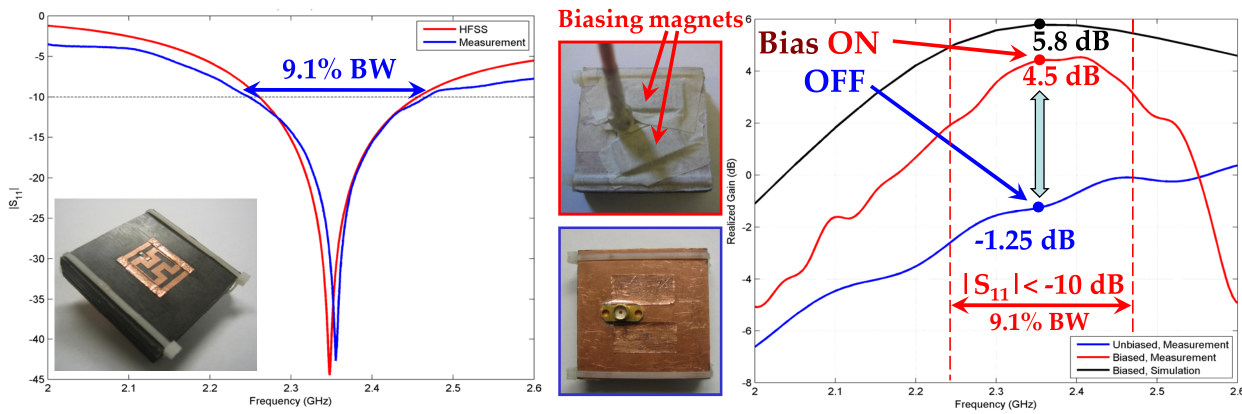

(a) (b)

Fig. 4. Measured return loss and realized gain of the MPC antenna prototype in Fig. 3(a). (a) Return loss. (b) Realized gain at broadside.

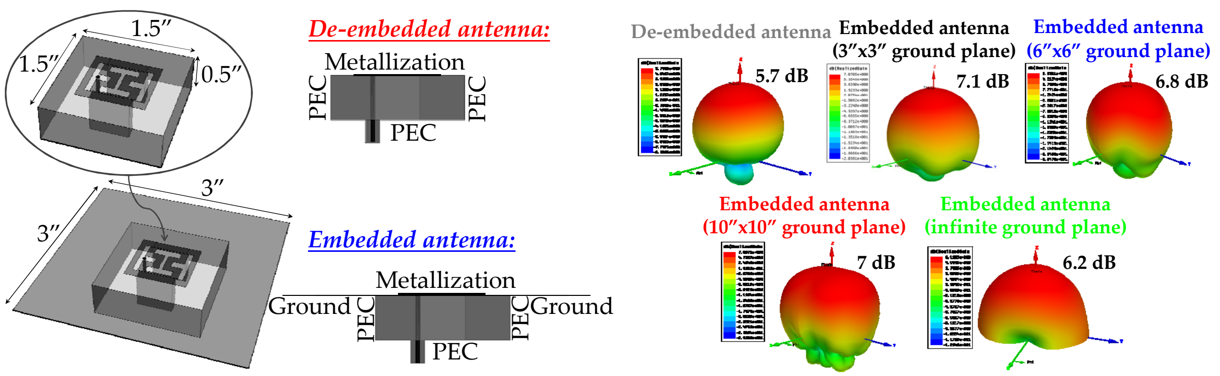

(a) (b)

Fig. 5. (a) Cavity-backed (de-embedded) and recessed (embedded) MPC antenna geometries. (b) Radiation patterns of these MPC antennas.

IV. ANTENNA PLACEMENT ON REPRESENTATIVE AUTOMOBILE PLATFORM

To investigate the in-situ performance of the recessed MPC antenna, several locations on horizontal and vertical surfaces of the automobile platform were selected for antenna placement, as shown in Fig. 7(a). These included centers, edges, and corners of any large/small, horizontal/vertical surfaces. Since the MPC antenna incorporates biased ferrimagnetic inclusions (with gyrotropic permeability tensors), it was designed using Ansoft HFSS. To analyze antenna placement on the electrically large vehicle, we used the uniform theory of diffraction (UTD) package of EMSS FEKO. To do so, the radiation pattern of the MPC antenna with 3″×3″ (7.62cm×7.62cm) ground was first obtained from HFSS. Then, this pattern was used as an excitation to illuminate the vehicle modeled using flat surfaces. Resulting radiation patterns are given in Fig. 7(b)-(e). In all cases, a similar broadside radiation pattern is retained with a gain higher than 5.4 dB. Small ripples in the patterns can be observed when antennas are placed towards surface centers. This is due to different phase terms of diffraction contributions from surface edges and their interference. These ripples are mostly avoided when the antenna is placed close to edges or corners of the surfaces, and overall gains are much improved in these cases.

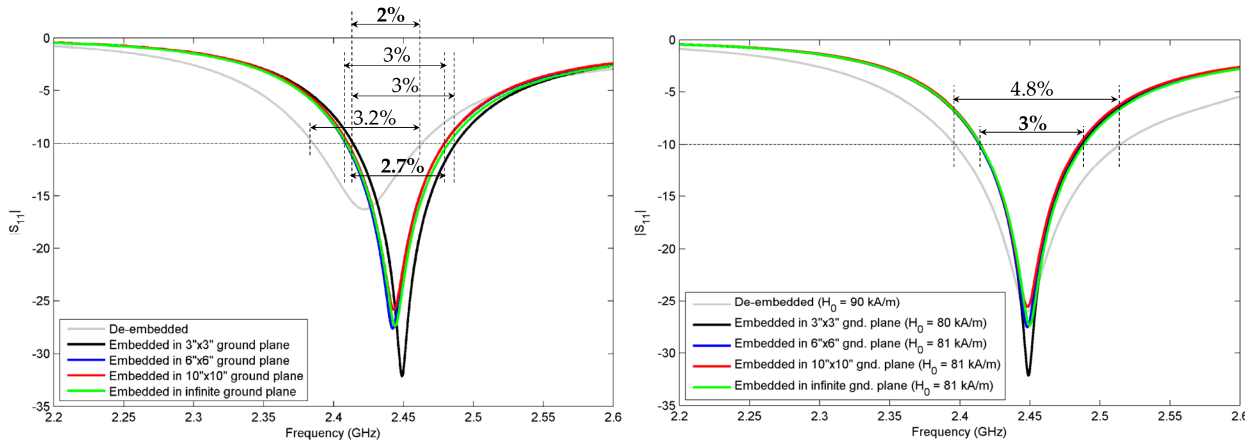

(a) (b)

Fig. 6. (a) Return losses of cavity-backed MPC antennas recessed into a ground plane. (b) Return losses of cavity-backed and recessed MPC antennas after retuning magnetic bias.

V. CONCLUSIONS

In this work, MPC modes were emulated and exploited for realizing smaller printed antennas with much improved bandwidths. Even smaller and cavity-backed versions of these antennas were embedded into a large vehicle. This resulted in zero-profile antennas and mitigated the platform loading effects, such as detuning of resonance or variations in radiation pattern. It is also found that these antennas would be suitable to be used much closer to the edges or corners of the vehicle for resulting in smaller ripple in patterns and improved gain. The presented design also alleviates the restrictions of available areas for antenna placement by utilizing edges and corners on the vehicle body.

ACKNOWLEDGMENTS

This work was supported by the U.S. Air Force Office of Scientific Research under Grant FA9550-04-1-0359, Lockheed Martin Corporation Strategic Technology Threads Program, the U.S. Army Research Laboratory, Adelphi MD (through Applied EM Inc. under contract #W911QX-09-C-0017), and by The Ohio State University Research Foundation.

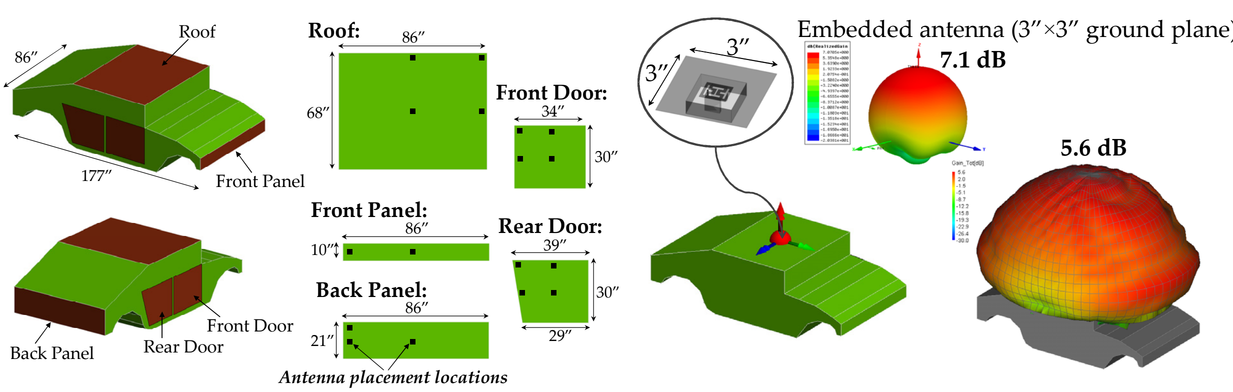

(b)

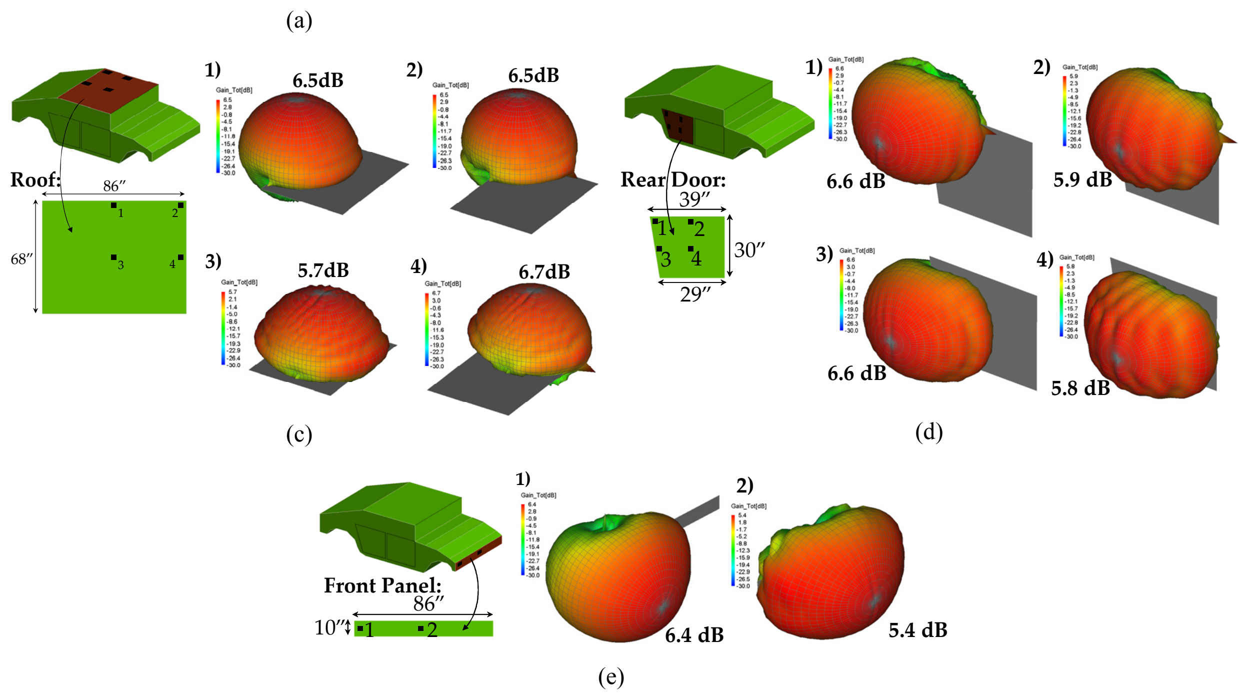

Fig. 7. (a) Selected antenna placement locations on the representative automobile platform. (b) Placement of recessed MPC antenna on the automobile platform. (c) Antenna placement at several locations on the roof, (d) rear door, and (e) front bumper.

REFERENCES

[1] A. Figotin and I. Vitebsky, "Nonreciprocal Magnetic Photonic Crystals," *Phys. Rev. E*, vol. 63, pp. 066 609-066 625, Feb. 2001.

[2] A. Figotin and I. Vitebsky, "Frozen Light in Photonic Crystals with Degenerate Band Edge," *Phys. Rev. E*, vol. 74-066613, pp. 1-17, Oct. 2006.

[3] A. Figotin and I. Vitebsky, "Slow-Wave Resonance in Periodic Stacks of Anisotropic Layers," *Phys. Rev. E*, vol. 76-053839, pp. 1-12, Nov. 2007.

[4] G. Mumcu, K. Sertel, and J. L. Volakis, "Miniature Antennas and Arrays Embedded within Magnetic Photonic Crystals," *IEEE Antennas Wireless Propag. Lett.*, vol. 5, pp. 168-171, Dec. 2006.

[5] S. Yarga, G. Mumcu, K. Sertel, and J. L. Volakis, "Degenerate Band Edge Crystals and Periodic Assemblies for Antenna Applications," in *Proc. IEEE Int. Workshop on Antenna Technol. Small Antennas and Novel Metamater.*, pp. 408-411, Mar. 2006.

[6] J. L. Volakis, K. Sertel, and C. C. Chen, "Miniature Antennas and Arrays Embedded within Magnetic Photonic Crystals and Other Novel Materials", *Applied Computational Electromagnetics Society Journal, Special Issue on ACES 2006 Conference*, vol. 22, no. 1, pp. 22-30, March 2007.

[7] G. Mumcu, K. Sertel, and J. L. Volakis, "Miniature Antenna using Printed Coupled Lines Emulating Degenerate Band Edge Crystals," *IEEE Trans. Antennas Propag.*, vol. 57, no. 6, pp. 1618-1624, June 2009.

[8] E. Irci, K. Sertel, and J. L. Volakis, "Antenna Miniaturization using Coupled Microstrip Lines Emulating Magnetic Photonic Crystals," in *Proc. 2009 IEEE Antennas and Propagation Soc. Int. Symp.*, pp. 1-4, 2009.

Performance Comparison between Rigorous and Asymptotic Techniques Applied to the Analysis of Wind Turbines

Abdelhamid Tayebi[1], Josefa Gómez[1], Iván González[1], Lorena Lozano[1], Mª Jesús Algar[1], Eliseo García[2], Íñigo Etayo[3], and Felipe Cátedra[1]

[1] Computer Sciences Department, University of Alcalá, Alcalá de Henares, Madrid 28871, Spain
hamid.tayebi@uah.es, josefa.gomezp@uah.es, ivan.gonzalez@uah.es, lorena.lozano@uah.es, felipe.catedra@uah.es

[2] Automatic Department, University of Alcalá, Alcalá de Henares, Madrid 28871, Spain
eliseo.garcia@uah.es

[3] Ingeniería y Proyectos de Telecomunicaciones. Acciona-Energía S.A. Sarriguen, Navarra, Spain
ietayo@acciona.es

Abstract ─ The scattering field analysis of wind turbines using asymptotic and rigorous techniques is presented. Several simulations considering different configurations and frequencies are conducted to compare the performance of the electromagnetic techniques. These predictions are very useful for studying the influence of wind farms in terrestrial radio systems. On the other hand, not only a static analysis has been done but also a study of the scattered fields when the blades are in movement. The Doppler effect due to the blade movement has been taken into account to achieve some simulation results. Modules FASANT and MONURBS of NEWFASANT computer tool have been used. FASANT is based on the geometrical theory of diffraction (GTD) on its uniform theory of diffraction (UTD) formulation and MONURBS is based on the method of moments (MoM) and physical optics (PO). A comparison of the results obtained with both codes is shown, as well as the CPU-time and computer memory required.

Index Terms ─ Electromagnetic propagation, radiofrequency interference, wind energy.

I. INTRODUCTION

Concern about energy and the future exhaustion of fossil fuels have led to the use of renewable energy. As an example, it is expected that wind energy will cover 12% of the global energy demand in the next 12 years. According to the Global Wind Energy Council's most ambitious scenario for wind energy development, wind could produce 2,600 TWh of electricity and save 1.5 billion tons of CO2 in 2020 [1]. However, wind energy also implies problems related to electromagnetic interference.

Wind turbines in deployment nowadays consist of a tower with over 80 meters in height and blades of over 40 meters in length, therefore, they are potentially interfering structures for electromagnetic waves with wavelengths comparable or smaller, as is the case of radio communication services operating in VHF bands or higher. For instance wind turbines could interfere with aerial radio navigation, radar, and TV broadcast systems, [2-5].

Before installing a wind farm, a study of the scattered field by the wind turbines must be carried out to avoid any possible interference with nearby radio systems; the location of the wind turbines have to be chosen in function of this study. There are two alternatives considered in this study. The first one is to create a measurement campaign to compute the scattered field of the windmill over the terrain. This solution is often discarded because it implies a high cost in terms of equipment, time, and personnel. The second alternative consists of carrying out several electromagnetic simulations with appropriate computer tools to analyze the behavior of the wind turbines without wasting too many resources.

In this paper, different kinds of simulations comparing GTD/UTD [6], PO, and MoM approaches have been performed to analyze the electric field scattered by a wind turbine. GTD/UTD and PO are asymptotic techniques used to analyze the scattered fields produced by complex bodies at high frequencies. Their main disadvantage is that they do not work properly at low frequencies but have the advantage of spending fewer resources than rigorous techniques. On the other hand, MoM is a rigorous method that can be applied to any frequency. However, one drawback with MoM is that more computer resources are required when the simulation is performed at high frequencies. A comparison of rigorous and asymptotic approaches is performed to evaluate the efficiency of each one at different frequencies.

This paper is organized as follows: section II presents modules FASANT and MONURBS of NEWFASANT computer tool [7-10]; section III describes the geometrical model of the wind turbine; section IV gives the results obtained; and section V presents the conclusions.

II. DESCRIPTION OF THE COMPUTING TOOLS

FASANT and MONURBS modules have been improved recently with the inclusion of new algorithms, parallelization schemes. Both modules share the graphical user interface of NEWFASANT that makes design and simulation easier. This tool allows creating any geometrical model for analysis. The tool also allows the optimization of geometrical parameters to achieve design specifications.

One important feature the modules share is that the structure analyzed is modeled using parametric surfaces. Thus, an accurate representation of the real shape is meshed and analyzed. NEWFASANT has its own meshing tool that provides different mesh sizes depending on the simulation frequency and module considered. Any surface of the model is divided mainly into curved quadrangles as shown in Figure 1. The meshing tool is parallelized using a cluster of processors to quickly obtain the mesh of a wind turbine in a few seconds.

Different versions of NEWFASANT are available for several operating systems and platforms. FASANT and MONURBS have been successfully tested and applied to the analysis of the radiated and scattered fields of several complex structures such as ships, satellites, on board antennas, electromagnetic compatibility, radar cross sections, microstrip circuits, etc.

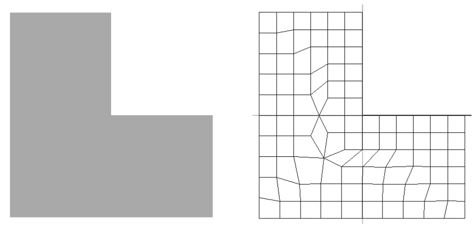

Fig. 1. Mesh of an arbitrary surface.

A. FASANT

FASANT is based on GTD/UTD techniques and ray-tracing methods. A combination of the angular Z-buffer, the volumetric space partitioning, and a new iterative heuristic algorithm is applied for accelerating the ray-tracing technique. The antennas and the environment can be defined by conductors, dielectric materials, periodic structures, or metamaterials.

B. MONURBS

MONURBS is based on MoM and uses the multilevel fast multipole method (MLFMA) [11], the characteristic basis functions method (CBFM) [12], and the message passing interface (MPI) standard [13] to solve large scale structures. PO is also included to reduce the computation time and memory requirements incurred from conventional MoM when analyzing very large structures at high frequencies.

III. WIND TURBINE MODEL

Figure 2 shows an example of a geometrical model of a wind turbine, modeled by 244 parametric surfaces. The size of the model is 120 m high and 64 m between the ends of the blades. This means that the electrical size is 640λ at a 1.6 GHz simulation frequency.

This model can be imported and/or exported to FASANT and MONURBS using CAD formats such as DXF, ACIS SAT, IGES, etc. Both codes are compatible with modern CAD tools. Once the geometry has been imported, it can be analyzed to obtain the scattered field by using the three techniques previously described.

In this study, the source antenna is placed 20 km away from the wind turbine. The source is modeled as a vertical dipole oriented along the z axis with a dipole moment of 1 and elevated 60 m above the reference plane (z=0). The observation points are distributed over a circle with a 5 km radius and elevated 60 m. Figure 3 shows the simulated scenario.

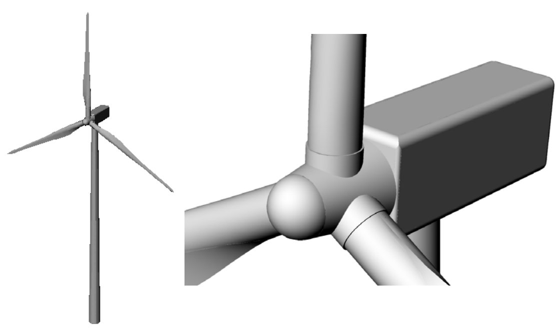

Fig. 2. Geometrical model of the wind turbine.

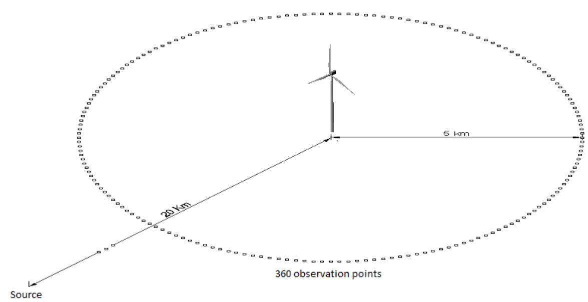

Fig. 3. The wind turbine is located inside the circumference of 360 observation points.

IV. RESULTS

Two different configurations of the wind turbine have been analyzed to study the interference due to its presence on the surrounding radio systems. The first one is related to the static structure (with static blades) and the second one considers the movement of the blades. The Doppler effect has been considered for obtaining realistic results in the second configuration.

A. Study of the wind turbine scattering with static blades

Several simulations were conducted to compare the performance of the different electromagnetic methods at several frequencies. GTD/UTD results were obtained with FASANT, whereas MoM and PO results were obtained with MONURBS.

The scattered field by the wind turbine is computed by taking into account the bistatic and the monostatic analysis at 100 MHz, 200 MHz, 400 MHz, 800 MHz, and 1.6 GHz. Note that only the z component of the electric field (the dominant component in this case) is depicted in Figures 4-8.

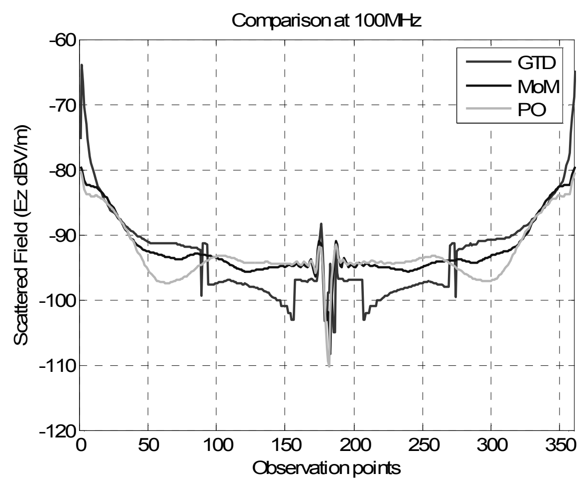

Fig. 4. Comparison of the scattered field at 100 MHz in the bistatic mode.

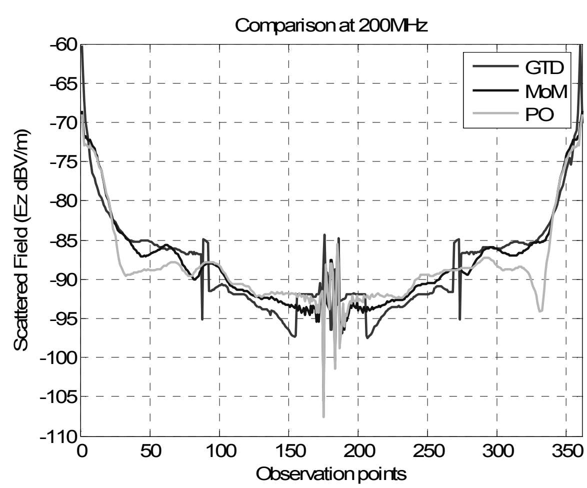

Fig. 5. Comparison of the scattered field at 200 MHz in the bistatic mode.

According to the results, there are significant differences between the asymptotic (PO-GTD/UTD) and rigorous (MoM) solutions at 100 MHz, as can be observed in Figure 4. This occurs because there are parts of the wind turbine that are too electrically small at low frequencies for the asymptotic techniques to provide accurate solutions. When the frequency is higher, the results of the three methods converge to the same solutions, as shown in Figures 5-8.

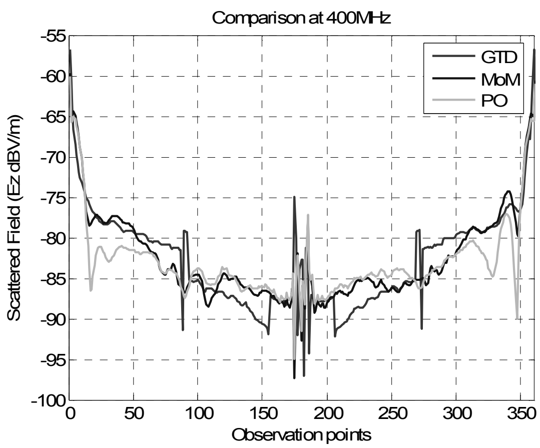

Fig. 6. Comparison of the scattered field at 400 MHz in the bistatic mode.

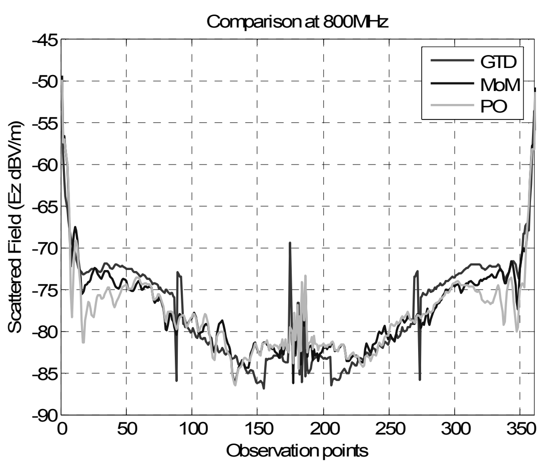

Fig. 7. Comparison of the scattered field at 800 MHz in the bistatic mode.

Regarding the CPU time, the asymptotic techniques take significantly less time than MoM. For instance, FASANT spends 2 hours and 50 minutes to solve the problem for all the frequencies in a single-processor PC. FASANT considers all the frequencies in one simulation because the ray tracing is the same for every frequency. However, MONURBS must calculate the induced currents for each frequency, notably increasing the CPU time. Table 1 shows the CPU time that MONURBS spends using 8 processors to solve the problem from 100 MHz to 800MHz. However, 30 processors have been used to solve the problem at 1.6 GHz. If the PO currents are used, the CPU time for the same computer decreases, as shown in Table 1.

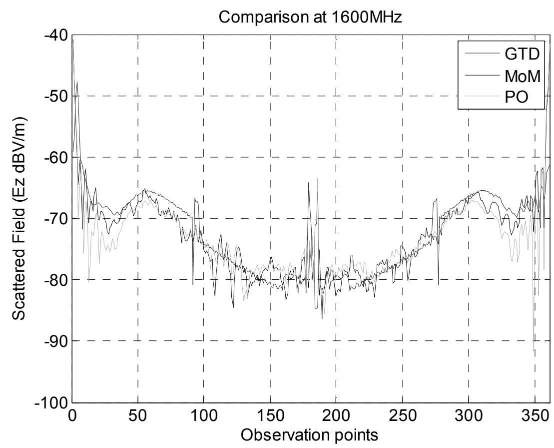

Fig. 8. Comparison of the scattered field at 1600 MHz in the bistatic mode.

Table 1: CPU time comparison for different frequencies

Frequency (MHz)	**MoM**	**PO**	**Nº processors**
100	3min. 36s.	38s.	8
200	6min. 42s.	1min. 15s.	8
400	10min. 35s.	2min. 22s.	8
800	29min. 5s.	7min. 38s.	8
1600	2h. 28min.	11min. 58s.	30

The number of unknowns in the MoM approach increases at high frequencies because the discretization process is performed depending on the frequency. Many MoM computer codes use subdomain basis functions defined over flat faceted meshes of the problem geometry. These codes require a mesh density of 10 divisions per lambda or higher. However, MONURBS uses as basic functions modified rooftop functions defined over curved quadrangles or triangles. Therefore, MONURBS can work with mesh based on curved quadrangular/triangular elements. These meshes fit better to curved surfaces and avoid the truncation errors caused by modeling curved surfaces as a set of flat facets. As a consequence, MONURBS can solve problems involving smooth surfaces with a lower sampling density in the mesh. MONURBS therefore requires fewer unknowns than codes based on flat faceted meshes. The number of unknowns is reduced using MONURBS when the geometry does not present electrically small features. The geometry of the wind turbine can be considered almost uniform because it is composed of smooth surfaces. To ensure this statement is true, a study of the number of divisions per lambda was performed. Figure 9 displays the scattered field at 800 MHz for five different mesh sizes. Table 2 shows the number of unknowns required for each mesh density.

Table 2: Comparison of the number of unknowns at 800MHz for different mesh densities when using MoM technique

Mesh size	MoM unknowns
Lambda/2	41.884
Lambda/3	96,834
Lambda/4	191,947
Lambda/5	265,278
Lambda/6	379,157
Lambda/7	517,782
Lambda/8	674,539
Lambda/10	1,026,132

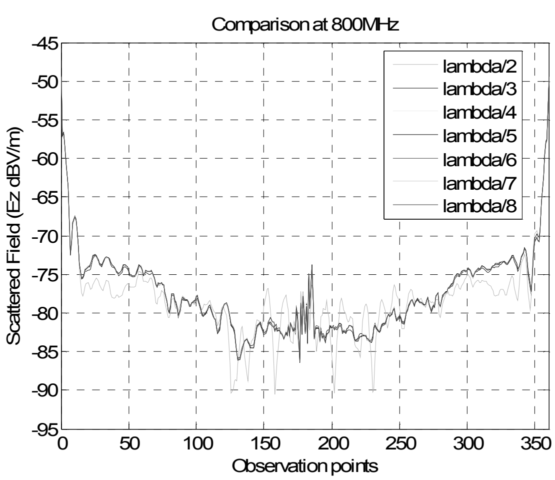

Fig. 9. Comparison of the results for several mesh sizes when using MoM technique.

As shown in Figure 9, only a few slight differences are found when the mesh resolution is increased. Figure 9 shows that the five solutions are similar. The MoM results of Figures 4-8 was obtained with a mesh density of 3 subdomains per lambda.

B. Study of the wind turbine with the blades in movement

One of the main interference problems in the deployment of wind turbine farms in the vicinity of radio communication systems is due to the Doppler frequency spectrum spreading and Doppler frequency shift generated by the rotation of the blades.

The first case we considered in the study of the Doppler effect is a test case defined by the rotating cube of 1 meter side centered at the coordinated axes shown in Figure 10. The y-axis had been chosen as the rotation axis. The transmitting and observation points are static and both located at point (5.0, 0, 0). The angular speed is 1.5 rad/sec. The transmitter emits a pure monochromatic tone of a frequency of 1 GHz. A correlation time of 1 second is considered in the receiver that means that the Doppler spectrum is computed considering spectral windows of 1 Hz width (in other words, for a given frequency f_0 all the fields contributions in a frequency band of 1 Hz centered at f_0 are coherently added).

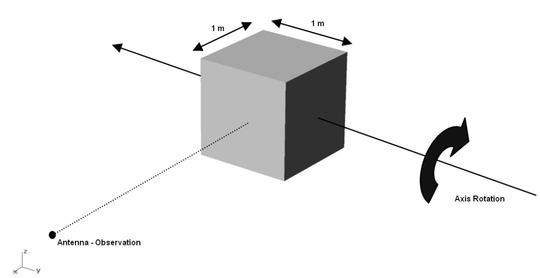

Fig. 10. Rotating cube throw an axis and location of the antenna – observation point.

Figure 11 shows the Doppler spectra for an incident tone of frequency 1 GHz obtained with the GTD/UTD and MoM approaches. The phase delay due to change of the path length due to movement from the transmitter to the scattering (two way path) is considered for each contribution (MoM subdomain current or reflection/diffraction

GTD/UTD point). It can be noticed that the GTD/UTD technique gives an unrealistic discontinuous Doppler spectrum. That is because the GTD formulation computes the fields in terms of a discrete set of ray-path contributions. Each contribution is computed using an asymptotic expression for computing the physical optic integral that does not take into account the phase delay in each point of the surface current due to the movement.

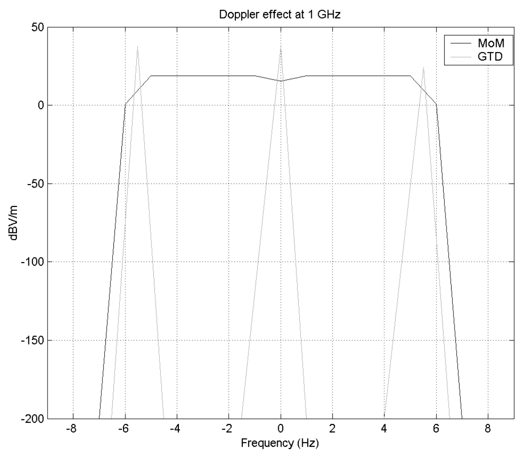

Fig. 11. Doppler spectrum of the scattering field at the observation point for the rotating cube test case comparing MoM and GTD approximation.

An example of analysis of the Doppler effect of the wind turbine test case shown in Figure 12 is presented here. The turbine blades rotate around the axis defined by points (7.27, 0.0, 79.38) and (-21.193, 0.0, 81.87), (the rotating axis is in the y=0 plane). The transmitting and observation points are static in the point (-130, 10, 90) and the angular speed of the blades is 2.0 rad/sec. The transmitter emits a tone of frequency 1.2 GHz.

Figure 13 shows the Doppler effect in the spectra obtained with the MoM and the PO approximation showing good agreements. The GTD/UTD results have been discarded because this approach gives unrealistic results, at least using the expression for the computation of reflection/diffraction coefficients for static cases.

V. CONCLUSION

A preliminary study of the scattered field from a real wind turbine has been presented using GTD/UTD and MoM-PO techniques. It has been demonstrated that the asymptotic techniques do not provide good solutions at lower frequencies. When the frequency is increased, the results converge to a similar solution with GTD/UTD and PO spending less CPU time than the rigorous technique. Additionally, the use of the asymptotic techniques allows higher frequency analysis without requiring higher computational resources. The asymptotic technique also allows the study of more than one wind turbine to analyze the effects of a wind farm. Note that this study would be quite complicated to be performed with rigorous methods due to its limitations when the structure under analysis is too large.

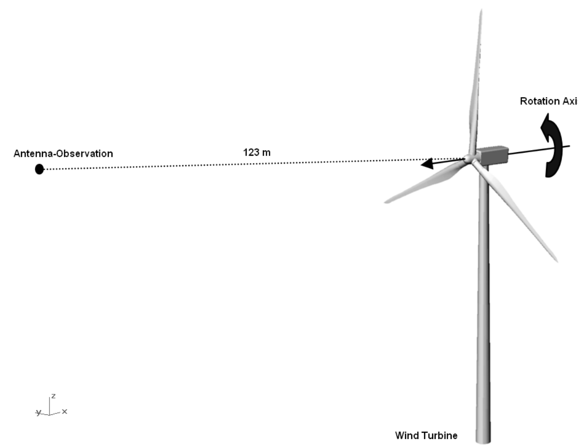

Fig. 12. Rotating blades of the wind turbine and location of the antenna – observation point.

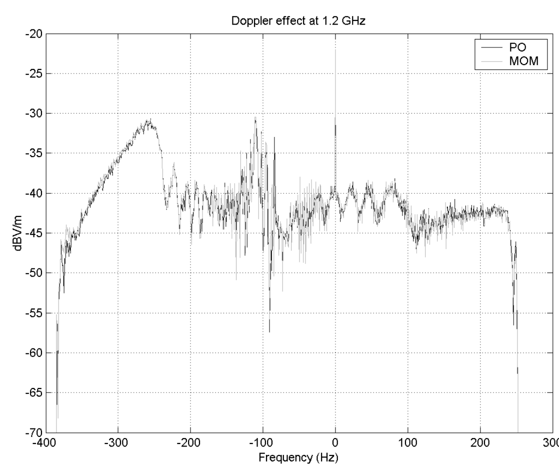

Fig. 13. Doppler effect of the rotating blades of the wind turbine.

ACKNOWLEDGMENT

This work has been supported, in part by the Spanish Department of Education and Science, Project TEC2007-66164 and CONSOLIDER-INGENIO Nº CSD-2008-0068, by Comunidad de Madrid Project S2009/TIC-1485 and by the Castilla-La Mancha Project PPII10-0192-0083.

REFERENCES

[1] http://www.gwec.net/

[2] B. M. Kent, K. C. Hill, A. Buterbaugh, G. Zelinski, R. Hawley, L. Creavens, Tri-Van, C. Vogel, and T. Coveyou, “Dynamic Radar Cross Section and Radar Doppler Measurements of Commercial General Electric Windmill Power Turbines Part 1: Predicted and Measured Radar Signatures,” *IEEE Antennas and Propagation Magazine*, vol. 50, April 2008.

[3] K. H. Cavcey, L. Y. Lee, and M. A. Reynolds, “Television Interference due to Electromagnetic Scattering by the MOD-2 Wind Turbine Generators,” *IEEE Transactions on Power Apparatus and Systems*, vol. 103, February 1984.

[4] D. L. Sengupta and T. B. A. Senior, “Electromagnetic Interference to Television Reception Caused by Horizontal Axis Windmills,” *Proceedings of the IEEE*, August 1979.

[5] I. Etayo, A. Satrustegui, M. Yabar, F. Falcone, and A. Lopez, “Analysis of the Frequency and Time Variation of Radio Signals Scattered by a Wind Turbine,” *European Conference on Antennas and Propagation 2010*, pp. 12-16, Barcelona, April 2010.

[6] F. Weinmann, “UTD Shooting-and-Bouncing Extension to a PO/PTD Ray Tracing Algorithm,” *Applied Computational Electromagnetics Society Journal*, vol. 24, no. 3, pp. 281-293, 2009.

[7] www.fasant.com

[8] I. González, L. Lozano, S. Cejudo, F. Sáez de Adana, and F. Cátedra, “New Version of FASANT Code,” *Antennas and Propagation Society International Symposium*; 5-11 July 2008.

[9] M. F. Cátedra and J. Pérez, *Cell Planning for Wireless Communications,* Artech House Publishers, Boston, London, 1999.

[10] I. González, E. Garcia, F. Saez de Adana, and M. F. Cátedra, “MONURBS: A Parallelized Multipole Multilevel Code for Analyzing Complex Bodies Modeled by NURBS Surfaces,” *Applied Computational Electromagnetics Society (ACES) Journal,* vol. 23, no. 2, pp. 134-142, June 2008.

[11] F. Cátedra, C. Delgado, E. García, and I. González, “Combination of MLFMA and an Interactive Method to Compute Large Scattering of Radiation Problems,” *The 4th European Conference on Antennas and Propagation, EUCAP 2010*, Barcelona, April 2010.

[12] E. García, C. Delgado, A. Tayebi, J. Gómez, and F. Cátedra, “Matrix Compression Technique Based on the Multilevel Characteristic Basis Function Method,” *The 4th European Conference on Antennas and Propagation, EUCAP 2010*, Barcelona, April 2010.

[13] http://www.mcs.anl.gov/research/projects/mpi/

Abdelhamid Tayebi was born in 1983. He received the B.S. and M.S. degrees in Telecommunications Engineering from the University Polytechnic of Cartagena (UPCT), Spain, in 2005 and 2007, respectively. Since 2007, he currently is pursuing the Ph.D. degree at the Computation Science Department, University of Alcalá, Spain. He has participated in several research projects with Spanish and European companies. He has published more than ten conference contributions at international symposia. His research interests are design and optimization of antennas, electromagnetic radiation and scattering, on-board antennas analysis, and design of graphical user interfaces.

Josefa Gómez was born in 1984. She received the B.S. and M.S. degrees in Telecommunications Engineering from the University Polytechnic of Cartagena (UPCT), Spain, in 2005 and 2007, respectively. Since 2007, she is pursuing the Ph.D. degree at the Computation Science Department, University of Alcalá, Spain. She has participated in several research projects with Spanish and European companies. She has published more than ten conference contributions at international symposia. Her research interests are design and optimization of antennas, electromagnetic radiation and scattering, on-board antennas analysis, and design of graphical user interfaces.

Iván González was born in Torrelavega, Spain in 1971. He received the B.S. and M.S. degrees in Telecommunications Engineering from the University of Cantabria, Spain, in 1994 and 1997, respectively, and the Ph.D. degree in Telecommunications Engineering from the Univeristy of Alcalá, Madrid, Spain, in 2004. He worked in the Detectability Laboratory of the National Institute of Technical Aerospace (INTA), Madrid, Spain in RCS prediction and measurements and as Assistant Researcher at the University of Alcalá. Since 2004, he works as Assistant Professor in the University of Alcalá in the Computation Science Department teaching concepts about Data Base Systems. He has participated in several research projects with Spanish and European companies, related with analysis of on board antennas, radio propagation in mobile communications, RCS computation, etc. His research interests are in numerical methods applied to the electromagnetic problems, rigorous and asymptotic techniques like method of moments, GTD/UTD, PO, etc. Also, the numerical method to represent complex bodies for the electromagnetic techniques and computer graphics is one of his research areas.

María J. Algar was born in Madrid, Spain in 1984. She received a M.S. degree (2007) in Telecommunications Engineering from Alfonso X El Sabio University, Spain. She is currently pursuing a Ph.D. in Telecommunications from the University of Alcalá, where she works in research. Her current research interests include the analysis of on-board antennas, radio propagation on mobile communications, ray-tracing techniques, and high frequency techniques.

Eliseo García was born in Madrid, Spain, in 1977. He received the B.S., M.S., and Ph.D. degrees in Telecommunication Engineering from the University of Alcalá, Spain, in 1999, 2001, and 2005, respectively. Since 2005, he worked at the University of Alcalá, first as Assistant Professor and since 2006, as Associated Professor in the Automatic Department. His research interests include numerical methods applied to scattering and radiation problems, parallel computing, and fast computational techniques applied to electromagnetics.

Íñigo Etayo. Biography not available

Manuel F. Cátedra received his M.S. and Ph. D. degrees in Telecommunications Engineering from the Polytechnic University of Madrid (UPM) in 1977 and 1982, respectively. From 1976 to 1989, he was with the Radiocommunication and Signal Processing Department of the UPM. He has been Professor at the University of Cantabria from 1989 to 1998. He is currently Professor at the University of Alcalá, in Madrid, Spain. He has worked on about 90 research projects solving problems of Electromagnetic Compatibility in Radio and Telecommunication Equipment, Antennas, Microwave Components and Radar Cross Section and Mobile Communications. He has developed and applied CAD tools for radio-equipment systems such as Navy-ships, aircraft, helicopters, satellites, and the main contractors being Spanish or European Institutions such as EADS, ALCATEL, CNES, ALENIA, ESA, DASA, SAAB, INTA, BAZAN, INDRA, and the Spanish Defence Department.

He has directed about 18 Ph.D. dissertations, has published about 70 papers (IEEE, Electronic Letters, etc), three books, about 10 chapters in different books, has given short courses and has given around a hundred and thirty presentations in International Symposia.

Dielectric Characterization and Optimization of Wide-band, Cavity-Backed Spiral Antennas

Nahid Rahman[1], Anjali Sharma[1], Mohammed Afsar[1], Sandeep Palreddy[2], and Rudolf Cheung[2]

[1]High Frequency Materials Measurement and Information Center
Tufts University, 161 College Avenue, Medford, Massachusetts 02155, USA
Email: Anjali.Sharma@tufts.edu, Nahid.Rahman@tufts.edu, mafsar@ece.tufts.edu

[2]Microwave Engineering Corporation, 1551 Osgood Street, North Andover, Massachusetts 01845, USA
s_palreddy@microwaveeng.com, r_cheung@microwaveeng.com

Abstract ─ This paper presents a novel approach to facilitate the design of wideband, cavity-backed spiral antennas. Using this approach, first, a 2-18 GHz, two-arm cavity backed Archimedean spiral antenna has been designed in FEKO. A multilayer dielectric absorber has been introduced in the cavity to facilitate unidirectional operation of the antenna. In order to incorporate the frequency-dependent complex permittivity data of the absorbing materials inserted in the cavity, precise microwave instrumentation has been used to determine these parameters experimentally. Based on this data, a genetic algorithm optimization procedure has been applied to derive the most favorable geometry of the absorbing cavity. Our results show that a design thus optimized significantly improves key performance parameters, maximizes the co-polarized gain, and minimizes the cross-polarized gain of the antenna across its operational bandwidth. We have then extended the approach to the design of a zigzagged 2-arm Archimedean spiral antenna and also a 1.5:1 ratio elliptical spiral antenna and presented the radiation characteristics here.

Index Terms ─ Axial ratio, broadband absorbing materials, cavity-backed spiral antenna, complex permittivity measurements, genetic algorithm optimization, radiation patterns.

I. INTRODUCTION

Spiral antennas with their wide bandwidth have always been a fascinating topic. In recent years, system performance demands on these antennas are becoming more and more complex. Currently, considerable interest has been placed on developing cavity-backed spiral antennas that retain their bandwidth performance despite having frequency-dependent lossy materials added to their cavities [1]. Among these antennas, the Archimedean spiral antennas are one of the most popular ones that exhibit exceptionally large bandwidths, can easily be spatially deployed and have the ability to maintain near-circular polarization and consistent input impedance over their bandwidth of operation [2].

The Archimedean spiral antenna is entirely specified by its angles as opposed to its physical length. It is a frequency self-selecting structure, in the sense that it radiates from a region where the length of the arm approximately equals to one or integer multiples of the wavelength. This gives rise to its broadband or frequency independent nature. The antenna has front-to-back symmetry and radiates bi-directionally [3]. But in most cases, a unidirectional pattern is preferred to detect reflections from or transmit towards one direction only. Therefore, a metallic cavity is added to absorb the back wave completely. Now, a cavity of depth $\lambda/4$ would absorb the back wave through destructive interference. But this condition would be satisfied for one frequency only, and we would obtain absorption for a very narrowband. Hence, it becomes necessary to insert absorbing materials in the cavity that can effectively absorb EM energy over a wide range of desired frequencies.

One common approach to extending the bandwidth of microwave absorbers is by using multiple layers of dielectric materials. The effective impedance in the material is gradually tapered with distance to minimize reflections. The loss mechanisms of absorbing materials are captured in the complex dielectric permittivity and magnetic permeability of that material. These properties are functions of frequency and consequently the absorbing properties vary significantly as the frequency of operation changes.

The optimum approach for the design of such an absorber would be to determine analytically the required permittivity and permeability values as a function of distance into the material, so that the reflection coefficient is minimized over a given frequency range, subject to incidence angle and thickness constraints. Unfortunately, the general form of the problem has not been solved yet [4]. What is done in practice is that the absorption properties of known materials are measured experimentally, and then different layers of dielectric materials are stacked together through a trial and error process. The effectiveness of these multi-layer absorbers is again determined from empirical data. This process is further complicated by the requirement of precise and sophisticated microwave techniques and instrumentation for high frequency characterization of dielectric materials.

An ideal broadband absorber should not only have the desired frequency coverage, but should also be sufficiently light, thin, inexpensive, and durable. Commercial absorbers are available only in certain dimensions, fixed by the manufacturers. The absorption characteristics vary significantly with material thickness, making the material dimensions an important parameter. It is very difficult to physically measure the absorber behavior for varying thickness values over a wide range of frequencies. The most feasible option would be to use optimization algorithms such that for a given set of materials, we obtain the best possible dimensions.

Keeping all this in mind, the design and analysis of a cavity backed spiral antenna entails the modeling of the antenna using proper simulation tools, appropriate characterization of the material constitutive properties and optimization of the dimensions of the stacked absorbing layers, so that the most favorable balance among bandwidth, thickness, and weight constraints of inserted materials and gain characteristics of the antenna is obtained.

Here, we have modeled a two-arm, cavity-backed, Archimedean circular spiral antenna with a multi-layer AN-74 dielectric absorber inserted in the cavity. The antenna has been simulated for its radiation characteristics over the frequency range 2 -18 GHz first without the absorbing materials, then with absorbing materials of fixed non-optimized thicknesses, and finally with optimized thicknesses for each absorbing layer. To capture the frequency dependent complex permittivity and loss tangent data for each layer, we used a network analyzer based transmission-reflection method in the High Frequency Materials Measurement and Information Laboratory at Tufts University. The material dielectric properties thus obtained were used in EM simulation software FEKO [5] to define the absorber material properties. With the FEKO optimizer, we then determined the optimal thickness of each layer such that the absorption properties are sufficiently retained, co-pol RHCP gain maximized and cross-pol LHCP gain minimized over the entire bandwidth.

The radiation patterns were then compared for their broadband performance. Our results show that we have been able to obtain an improved design with the best possible radiation characteristics when the knowledge of frequency-dependent data was accurately applied to the EM solver. The concept can be successfully extended to the design of any wideband antenna in general. We are motivated to investigate a wide range of dielectric and magnetic absorbing materials and design the most accurately characterized broadband antennas prior to their fabrication. We have then extended the approach to the design of a zigzagged 2-arm Archimedean spiral antenna and also a 1.5:1 ratio elliptical spiral antenna and presented the radiation characteristics here. Figure 1 shows the general antenna layout and direction of radiation for Archimedean spiral antennas.

Figure 2 shows a zigzagged Archimedean spiral and an elliptical Archimedean spiral antenna.

II. DIELECTRIC CHARACTERIZATION OF BROADBAND ABSORBERS

A 3-layer composite dielectric absorber, AN 74, manufactured by Emerson and Cuming, was used for the absorbing cavity. Each layer is a carbon-loaded polyurethane foam absorber which typically provides -20 dB insertion loss at different frequency bands from 2-18 GHz.

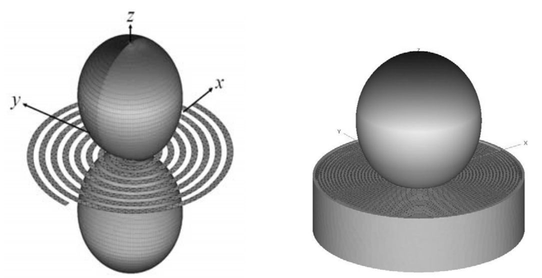

(a) (b)

Fig. 1. a) Bidirectional radiation pattern of a two arm Archimedean spiral antenna, b) unidirectional radiation pattern of a cavity-backed, two-arm Archimedean spiral antenna.

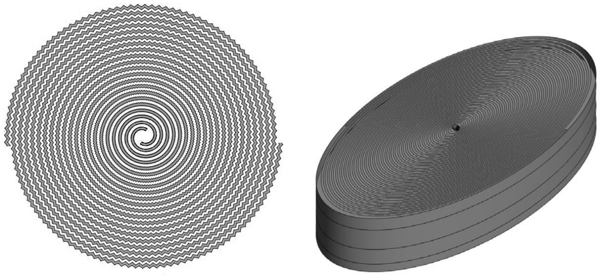

Fig. 2. a) Zigzagged 2-arm Archimedean spiral antenna, b) elliptical two-arm Archimedean spiral antenna.

The complex dielectric permittivity ε_r of each layer of the AN-74 absorber was accurately characterized with an Agilent Vector Network Analyzer using a waveguide-based transmission-reflection method.

The network analyzer automatically measured the complex reflection coefficients and transmission coefficients that resulted when a sample of material was inserted in a waveguide. The network analyzer measured the scattering parameters S_{11} and S_{21}. Once these coefficients were known, the values of ε_r were then calculated using the Jarvis-Baker method [6] for each of the three layers of the absorber. Data is obtained by performing measurements at 201 equally spaced frequency points. The data is stored, and the complex permittivity and permeability of the composite materials are calculated from the measured s-parameters using a MATLAB [7] program based on the Weir algorithm [8].

We denoted the three layers of the composite absorber as hard, middle, and soft layer, with the soft layer being closest to the antenna and the hard layer attached to the metallic cavity. For maximum absorption, there should be no mismatch between the absorber and air. In order to reduce mismatch, the EM wave should see impedance close to 377 ohm when it crosses the air-absorber interface. From the data we obtained from our measurements, we found that the soft layer provides the closest match in terms of impedance seen by the incident wave. Thus, we placed this layer closest to the antenna followed by the middle layer and hard layer.

The frequency dependent permittivity values are shown in Fig. 3.

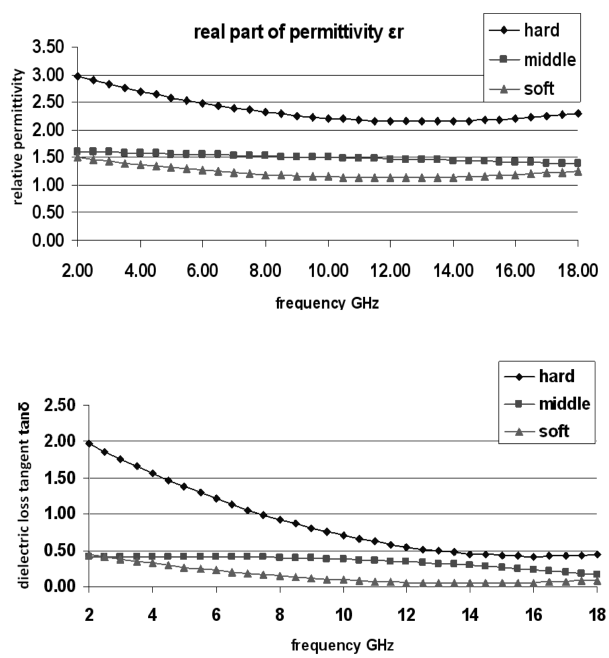

Fig. 3. Real part of permittivity and loss tangent for three layers of the composite absorber.

From the experimental values, we used curve fitting methods to derive the following equations relating complex permittivity to frequency.

Permittivity and loss tangent equations:

Hard: $\varepsilon = .0065f^2 - 0.1723f + 3.281$ (1)

$\tan\delta = 0.0078f^2 - 0.2514f + 2.4373$ (2)

Middle: $\varepsilon = -6e\text{-}17\ f^2 - 0.0133f + 1.6283$ (3)

$\tan\delta = -0.0015f^2 + 0.0147f + 0.38$ (4)

Soft: $\varepsilon = 0.0036\ f^2 - 0.0872f + 1.659$ (5)

$\tan\delta = 0.0027f^2 - 0.0763f + 0.5838$ (6)

Thus, by using very precise microwave measurement techniques, we were able to obtain permittivity data for each layer of the composite absorber from 2 to 18 GHz.

III. OPTIMIZATION OF WIDEBAND ANTENNAS

Derivation of frequency dependent parameters of the absorbing materials greatly facilitates designing optimum dimensions of the lossy cavity. Once we have the equations relating permittivity to frequency, it then becomes straightforward to use this data to define material properties in any electromagnetic simulation software with an optimizer feature available. The antenna can then be simulated at all frequencies for their radiation patterns by varying the material thicknesses. With optimization of the absorber dimensions, it becomes possible to obtain wider bandwidth and lower reflectivity. Although it is possible to calculate the reflectivity of a multilayer absorber, it is unfeasible to analytically solve for the optimum thickness of each layer over a wide range of frequencies. Fortunately, computer-based numerical algorithms can efficiently handle such complicated calculations. The FEKO simulator offers a number of numerical techniques to optimize the physical parameters of a design. Since a major point of concern for most algorithms is that they converge to local optima, we chose a global optimization technique, i.e. the genetic algorithm for our purposes if deriving the most favorable geometry of the composite absorber [5].

Multiple objectives were defined in this procedure to improve the overall radiation pattern of the antenna. Due to time and memory constraints, the number of maximum iterations was set to 80. We also incorporated the frequency dependent permittivity relations directly in the EDITFEKO solution settings. This allowed for the material properties to be appropriately updated as the frequency was varied during one complete iteration of the optimizer. Based on the computed electromagnetic parameters, we proceeded to optimize the thickness of each layer and depth of the cavity such that the RHCP gain of the spiral was maximized, LHCP gain minimized, reflection from the absorbing layers minimized, and absorption properties of the lossy composite material sufficiently retained over the entire bandwidth of operation.

We used the computed permittivity values in the FEKO software optimizer utility to arrive at the best possible thickness values that work best for an Archimedean spiral. For a 2-18 GHz spiral, a minimum composite absorber thickness of 0.805 inches and a 0.178 inch air gap between the antenna and absorbing layers gave the best broadband co-pol gain and axial ratio performance. We also simulated the antenna and observed the gain characteristics using industry specified absorber dimensions and also with no absorber inserted in the cavity at all. These results will serve as a reference to analyze how much improvement has been achieved through optimization. The generalized industry specified thicknesses are adequate for material testing purposes. However, in our work, we arrived at optimum absorber dimensions that provide the best radiation performance of an antenna model. In this way, prior to fabrication of the designed antenna, the required optimum dimensions can be specified to an absorber manufacturer, and each layer of the composite structure can be tailored to the needs of a specific application. In this way, we can eliminate the necessity of using adhesives to increase the thickness or further machining of the layers to decrease the thickness to a certain value.

Our contention is that this procedure can be used to design wideband antennas of any structure and cavity configuration.

IV. RESULTS AND DISCUSSION

The model was simulated at 9 discrete frequency points at intervals of 2 GHz. Upon completion of the optimization process, the final optimum thicknesses for the hard, middle, and soft surfaces were 0.257, 0.229, and 0.319 inches, respectively. Industry specified non-optimized thicknesses for each absorbing layer was 0.25 inches for each layer. The optimized absorber dimensions showed significant improvement over the non-optimized model.

A. Gain

A comparison of the boresight gains for the principle plane φ=0 of the antenna is shown in Table 1. It can be observed that throughout the operational band, the optimized spiral demonstrates sufficiently high gains, low side lobes, and no splits in the main beam for the entire frequency range of interest. It is also evident from the table that the introduction of the absorber layers in the cavity gave better isolation and optimization allowed for more consistent gain values throughout the bandwidth.

Table 1: Co-pol and cross-pol gain of optimized and non-optimized antenna

Freq (GHz)	Boresight Gain (dB)					
	no absorber inserted in cavity		absorber layers of equal thickness		absorber layers of optimal thickness	
	RHC	LHC	RHC	LHC	RHC	LHC
2	-0.10	-3.53	-0.13	-19.13	2.33	-9.74
4	4.18	-5.63	3.66	-15.56	4.67	-14.42
6	6.00	-14.73	5.94	-40.20	5.04	-62.19
8	5.44	-21.33	6.49	-64.20	5.94	-60.75
10	7.12	-29.32	5.25	-63.69	5.04	-71.20
12	2.49	-54.56	5.22	-49.57	5.94	-58.41
14	5.02	-47.97	5.04	-49.94	5.76	-72.46
16	0.90	-52.32	5.21	-54.38	6.12	-56.96
18	4.60	-45.45	6.29	-45.06	6.30	-45.25

B. Axial ratio

Figure 4 shows the axial ratio for all three configurations on boresight. An axial ratio close to 0dB implies that circular polarization is being maintained. The antenna without an absorber loaded cavity showed large values for axial ratio for frequencies until 7GHz. With the absorber inserted in the cavity, axial ratio was fairly less than 4 dB and in most cases, close to 0dB across the entire band. It is evident that the purity of circular polarization was sufficiently retained.

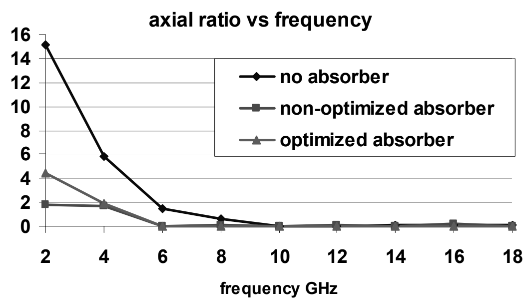

Fig. 4. Variation of axial ratio of the spiral antenna with frequency.

C. Return loss

Figure 5 gives a comparison of the return loss S_{11}. In the absence of absorbing layers, the return loss was as high as -3dB throughout the band of operation. Return loss is efficiently minimized to acceptable levels by loading the cavity with multi-layer absorbing materials.

In defining the optimization objectives, we did not attribute equal weights to all optimization goals. For instance, more weight was given to gain performance across the bandwidth than axial ratio and front-end reflection. As a result, the gain performance shows relatively greater improvement than axial ratio or reflection coefficient. Depending on the application, it is always possible to optimize for certain radiation characteristics or specific bandwidths of interest, where maximum performance is desirable.

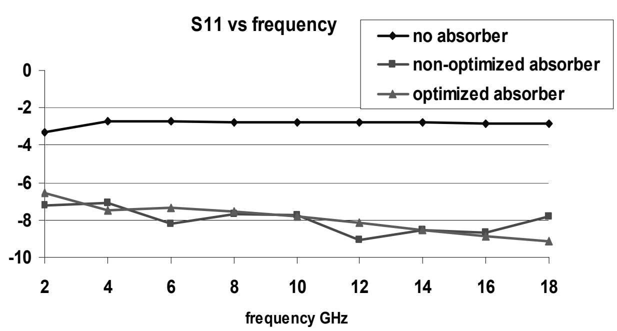

Fig. 5. Variation of return loss of the spiral antenna with frequency.

V. EXTENSION OF DESIGN TO OTHER SPIRAL MODELS

A. Cavity-backed zigzag Archimedean spiral

To reduce the size of the antenna, zigzag shaped arms can be used, so that the same length now occurs in a region much closer to the center of the spiral. But a zigzag circular spiral compromises the gain of the antenna compared to the simple circular spiral [9].

i. Gain

The boresight gains for both principle planes of the optimized antenna are shown in Table 2.

ii. Axial ratio

Figure 6 shows the axial ratio on boresight. Axial ratio was fairly less than 3.5dB and in most cases, close to 0 across the entire band. It is evident that the purity of circular polarization was sufficiently retained.

Table 2: Co-pol and cross-pol gain of optimized zigzag antenna

Freq (GHz)	Gain (Φ=0° plane)		Gain (Φ=90° plane)	
	RHC	LHC	RHC	LHC
2	2.32	-7.48	2.30	-7.48
4	5.02	-13.83	5.02	-14.22
6	5.36	-53.78	5.36	-53.78
8	5.42	-48.58	5.42	-48.58
10	5.56	-50.10	5.56	-50.10
12	5.69	-43.79	5.69	-43.79
14	5.96	-40.76	5.96	-40.65
16	6.22	-52.85	6.22	-52.85
18	6.35	-54.97	6.35	-54.97

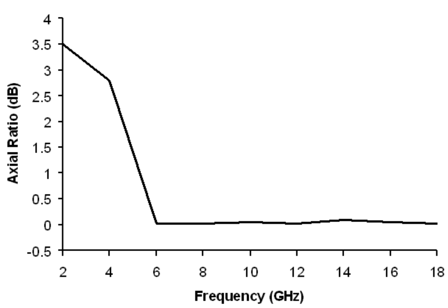

Fig. 6. Variation of axial ratio of the zigzag antenna with frequency.

B. Cavity-backed elliptical spiral

One of the spiral antenna models we have recently investigated is a cavity-backed two-arm elliptical spiral antenna. We investigated the elliptical structure and observed whether the structure provides changes in beam-width as well as changes in the radiation pattern. Our results show that by using an elliptical spiral antenna, we were able to regulate the beam-width in two orthogonal planes, $\varphi=0^0$ and $\varphi=90^0$. A sample plot is shown below in Fig. 7.

i. Gain and half-power beam-width

Table 3 shows the RHC gain, LHC gain, and half-power beam-width in two orthogonal planes for the 1.5:1 elliptical spiral.

ii. Axial ratio

An elliptical structure allows for different beam-widths in 2 orthogonal planes. However, the axial ratio in lower frequencies of operation degrades significantly with increasing major to minor axis ratio. In the future, we hope to improve the axial ratio in the lower frequencies in our models. Figure 8 shows the boresight axial ratio for an elliptical spiral antenna.

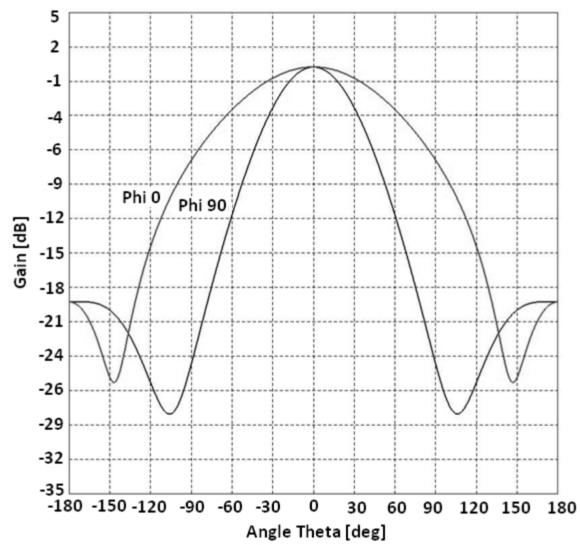

Fig. 7. Difference in half-power beam-widths in two principal planes of an elliptical spiral antenna at 2 GHz.

Table 3: Co-pol and cross-pol gain and 3dB beamwidth of optimized Archimedean elliptical spiral antenna

AN 74	Gain(dB)		-3dB beam-width	
Freq (GHz)	LHC	RHC	Φ=0° plane	Φ=90° plane
2	-8.646	1.025	100	84
4	-12.877	4.047	82	68
6	-22.065	3.322	68	80
8	-18.438	4.652	76	58
10	-26.175	4.168	84	88
12	-18.196	4.773	74	52
14	-17.137	5.917	88	52
16	-19.9	6.118	84	56
18	-15.598	4.846	64	92

At the time of this work, the antennas are in the process of fabrication and we were not able to include measured results. However, we have addressed the general problem of the design and optimization of wideband lossy cavities from a microwave material characterization standpoint. Our procedure can be efficiently used for accurately designing and optimizing the dimensions of any broadband, cavity-backed Archimedean spiral antenna in general with precise frequency dependent electromagnetic properties of materials.

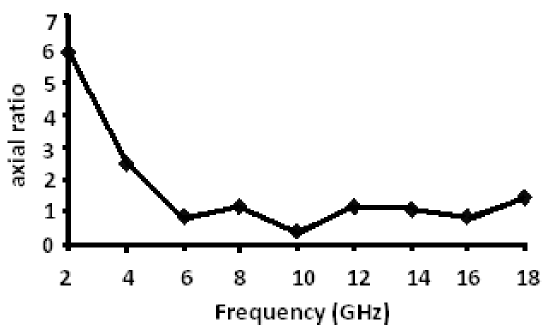

Fig. 8. Variation of axial ratio of the 1.5:1 elliptical antenna with frequency.

VI. CONCLUSION

An effective design procedure for cavity-backed wideband antennas has been presented. We have approached the problem of determining the optimal dimensions of the lossy material inserted in the cavity by using microwave measurement techniques and subsequently applying the genetic algorithm optimization routine to arrive at a geometry that meets desired radiation specifications. Using frequency-dependent complex permittivity or permeability values allows us to accurately take advantage of the powerful computational tools that are commercially available to simulate radiation patterns that give closest approximation to actual measured patterns. This procedure can be extended to the design of any configuration of cavity-backed spiral antenna that uses multi-layered broadband dielectric or magnetic absorbing materials.

ACKNOWLEDGMENT

The authors would like to thank Dr. Mahmut Obol for his assistance with Network Analyzer based measurements and Dr. C. J. Reddy at EMSS, USA for academic support with FEKO software.

REFERENCES

[1] S. E. Lipsky, *Microwave Passive Direction Finding*, SciTech Publishing, January, pp 39-47, 2004.

[2] T. Milligan, *Modern Antenna Design*, Wiley-IEEE Press, pp. 372-373, 1985.

[3] J. L. Volakis, M. W. Nurnberger, and D. S. Filipovic, "A Broadband Cavity-Backed Slot Spiral Antenna," *IEEE Antennas and Propagation Magazine*, vol. 43, no. 6, December 2001.

[4] Eugene F. Knott, John F. Shaeffer, and Michael T. Tuley, *Radar Cross Section*, SciTech Publishing, pp. 248-266, 2004.

[5] *FEKO Software*, EM Software and Systems, South Africa, 2008.

[6] J. Baker-Jarvis, E. J. Venzura, and W. A. Kissick, "Improved Technique for Determining Complex Permittivity with the Transmission/Reflection Method," *IEEE Trans. Microwave Theory Tech.*, vol. 38, no. 8, pp. 1096-1103, August 1990.

[7] MATLAB, (2007a), The MathWorks, Inc.

[8] N. Al-Moayed, M. N. Afsar, U. A. Khan, S. McCooey, and M. Obol, "Nano Ferrites Microwave Complex Permeability and Permittivity Measurements by T/R Technique in Waveguide," *IEEE Transactions on Magnetics*, vol. 44, no. 7, July 2008.

[9] M. N. Afsar, Y. Wang, and R. Cheung, "Analysis and Measurement of a Broadband Spiral Antenna," *IEEE Antennas and Propagation Magazine*, vol. 46, no. 1, February 2004.

Nahid Rahman is a Ph.D. student at the department of Electrical and Computer Engineering at Tufts University, Massachusetts. She received her M.S. degree in 2006 from Lehigh University, Pennsylvania and her B.S. degree in 2003 from Southeastern Oklahoma State University, Oklahoma. She is currently a research assistant at the Millimeter and Sub-millimeter Waves Laboratory at Tufts and working in a collaborative broadband antenna development program with Microwave Engineering Corporation, North Andover, Massachusetts.

Anjali Sharma is a Ph.D. student at the department of Electrical and Computer Engineering at Tufts University, Massachusetts. She received her M.S. degree in 2010 from Tufts University, MA and her B.S. degree in 2008 from Thapar University, India. She is currently a research assistant at the Millimeter and Sub-millimeter Waves Laboratory at Tufts.

Mohammed N. Afsar received the B.Sc. and M.Sc. degrees in Physics from the University of Dhaka, presently in Bangladesh, and the M.Sc.EE. degree in Microwaves and Quantum Electronics, Post-Graduate Diploma in Microwave Engineering from the University College London of the University of London, and the Ph.D. degree in Experimental Physics from the University of London, London, England. He taught physics from 1968 until 1970. From 1972 until 1978, he worked at the National Physical Laboratory of England, in the Division of Electrical Science, where he developed the techniques of Fourier transform spectroscopy for precision measurement of complex refractive index and complex dielectric permittivity and loss tangent of materials at millimeter-and submillimeter- wave frequencies. In 1978, he joined the Massachusetts Institute of Technology (MIT), Cambridge, where he worked as a Senior Scientist and Principal Investigator of several research projects. He was one of the main organizers (Executive Secretary 1985, 1987, 1988, and Conference Chair 1990) of the IEEE and SPIE annual International Conference on Infrared and Millimeter Waves. He is the Series Editor for the Institute of Physics book series in Measurement Science and Technology. He served as a Member of the Editorial board of the Institute of Physics *Journal of Measurement Science and Technology* (formerly *Journal of Physics*. From September 1984 until August 1987, he worked as a Professor, Department of Electrical Engineering, City College and the Graduate School of the City University of New York. Since October 1987, he has been working as Professor of Electrical Engineering and Computer Science at Tufts University, Medford, Massachusetts. He has published about 200 papers, inclusive of several book chapters. He has edited five books on millimeter and sub-millimeter waves, published by SPIE.

Professor Afsar is a Chartered Engineer in England and a Fellow of the IEE. He is also a Chartered Physicist and a Fellow of the Institute of Physics, London. He was awarded the 1977 Duddell Premium (Prize) by the IEE. He is a Member of the Electromagnetics Academy, the Institute of Systems and Components, and the American Physical Society. In 1992, he received the "Outstanding Research on Ferrites" award at the 6th International Conference on Ferrites held in Tokyo. In 1997, he received the "Man of the Year" award from American Biographical Institute Inc.

Sandeep Palreddy received his M.S.EE. degree in 2008 and his B.S.EE. in 2006 from the University of Massachusetts at Amherst. He is currently a Ph.D. student at Virginia Tech and lead RF engineer at the Microwave Engineering Corporation, Andover, Massachusetts.

Rudolf Lao-Tune Cheung received the B.S.EE. M.E.SS., and Ph.D. degrees in Electrical Engineering, all from the University of Washington, Seattle, in 1976, 1978, and 1982, respectively. From 1982 to 1985, he was a staff engineer at Transco Products, Inc., Marina del Rey, California, where he was engaged in the research and development of advanced microwave antenna products, specializing in broadband antennas. From 1985 to 1987, he was with the spacecraft antenna research group of the let Propulsion Laboratory, California Institute of Technology, Pasadena, where he was involved in reflector antenna design, and also developed antenna measurement techniques for space and ground applications. He returned to Transco Products in 1987 as a senior staff member, where he provided technical support to the engineering department. He joined Microwave Engineering Corporation (MEC), North Andover, Massachusetts in 1994 as an antenna product manager. He currently holds the position of Chairman at MEC. Dr. Cheung has published many papers in the electromagnetic and optics areas. He is a member of the IEEE and Tau Beta Pi. He also serves as an industrial advisory board member to the Electrical Engineering Department at the University of Massachusetts, Lowell, MA.

Modeling of CPW Based Passive Networks using Sonnet Simulations for High Efficiency Power Amplifier MMIC Design

Valiallah Zomorrodian, U. K. Mishra, and Robert A. York

Department of Electrical and Computer Engineering
University of California, Santa Barbara, CA 93106 USA
vzomorro@ece.ucsb.edu, mishra@ece.ucsb.edu, rayork@ece.ucsb.edu

Abstract – In this paper, the capabilities of the Sonnet software for accurate modeling and design of CPW based lumped-element resonators and matching networks is studied. A systematic method for design of complex matching networks using Sonnet is presented and good overall agreement between Sonnet simulations and measured s-parameter data from fabricated resonators and matching networks was obtained.

Index Terms ─ CPW, EM simulation, GaN, high power, lumped element, matching network, MMIC, monolithic, passives, Sonnet.

I. INTRODUCTION

High output power and high efficiency are two desirable factors for radio frequency (RF)/ microwave power amplifiers (PAs). Higher power added efficiency (PAE) leads to less DC power consumption by the circuit, therefore increasing the battery life and also relaxing the heat dissipation requirements. Monolithic microwave integrated circuits (MMICs) are of great interest in RF/Microwave application due to their much smaller size compared to the competing hybrid circuit technology. Among the existing microwave device technologies, AlGaN/GaN high electron mobility transistors (HEMTs) are particularly suitable for MMIC power amplifier applications due to their superior power-density and much higher breakdown voltage [1, 2, 3], and they have been successfully used in the past in MMIC power amplifier circuits [4,5].

Class B, C, and switch mode amplifiers such as Class E and Class F topologies are popular choices for high efficiency power amplifier applications. The issue of accurate input and output matching is especially important for these circuits since they are inherently narrow band tuned circuits and the gain, efficiency, and output power of the circuits are very sensitive to even minor mismatches in the matching networks and resonators. In order to obtain optimum circuit performance, it's essential to use accurate models for both the active HEMTs and the passive matching networks.

In this paper, the capabilities of the Sonnet software as an electromagnetic (EM) simulation tool for accurate modeling coplanar waveguide (CPW) based lumped element passive network is studied, and the results obtained from the simulations are compared against measured data from fabricated circuits. This particular topology was chosen because (i) due to lack of via technology in our fabrication process, we are limited to CPW environment for implementation of all passives and (ii) at lower microwave frequencies, lumped-element topology is the only feasible option for MMIC design due to the very large size of distributed elements at these frequencies. Nevertheless, the same design procedure could potentially be used for distributed structures and for microstrip environment.

This paper is not intended to compare the accuracy of Sonnet against other EM simulation software packages. The intention is simply to demonstrate the capabilities of the Sonnet software when it is used for a practical circuit design application, and the systematic design procedure that can be used for an accurate and efficient design for complex passive network.

II. FABRICATION

The lumped-element matching networks and resonators consist of parallel-plate capacitors and multi-turn spiral square inductors. The capacitors were fabricated using two 0.25 μm thick gold layers used for the parallel plates with a 130-nm thick SiN used for the dielectric layer. The dielectric constant of the SiN was experimentally determined to be about 7 at the RF/microwave frequencies of interest. A 3 μm gold layer was used for the ground planes and the interconnects.

The multi-turn inductors were implemented using the 3 μm gold interconnect layer and a 1 μm gold bridge separated by a 3 μm bridge post made from PMGI SF-15 photoresis [6]. The PMGI may be etched away after fabrication to create a true air-bridge, but most often it is left in place considering its relatively large thickness and small dielectric constant. Process variations that most often affect the performance of the passive circuits include the thickness variation of the deposited SiN which affects the capacitance values and to a lesser extent the thickness variation of the deposited interconnect metal, which can affect the resistive losses. All circuits were fabricated at the UCSB Nanofabrication Facility.

III. EM SIMULATION AND MODELING

There are a few approaches possible for designing passive networks. One approach relies on creating libraries based on measured s-parameters from fabricated inductors and capacitors of various sizes and geometries. In the absence of accurate EM simulation software, this is probably the most practical approach. However, this can be a very expensive and time consuming procedure since it requires fabrication and measurement of a large number of elements. Moreover, when the elements are placed in a circuit layout, it is difficult to accurately predict effects such as mutual coupling between the elements, the variations in the ground current paths (especially important in CPW environment) and the effects of all the interconnects using only these libraries.

Reliable EM simulation software can alleviate these problems mentioned above and allow for a much faster and more accurate way of modeling complex matching networks. The Sonnet software has proven to be a very accurate and powerful tool for planar EM simulations [7]. When the modeling is carried out in a systematic way, we will show that complex matching networks and resonators can be designed with excellent accuracy and minimum effort using Sonnet simulations.

Sonnet uses the method of moments applied directly to Maxwell's equations to solve planar problems. Detailed mathematical description of the method of moments and the theory used in Sonnet are found in [8] and [9], respectively, and an overview of Sonnet's operation can be found in [10]. This works quite well for modeling of passive networks used in MMICs because of their planar geometry.

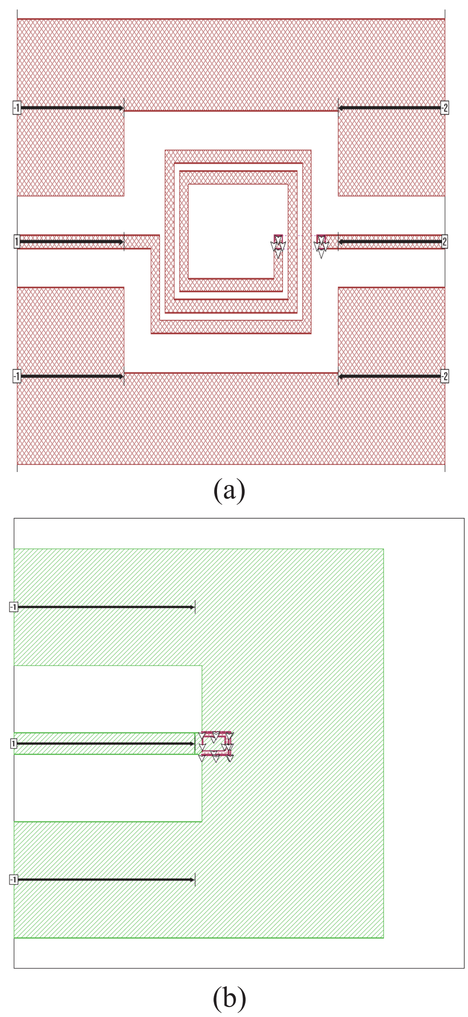

Fig. 1. (a) Layout of an inductor and (b) layout of a capacitor in Sonnet.

For accurate EM modeling it is important to simulate the elements exactly the same way that they are fabricated in the circuit. This will ensure that the currents flow in the right directions and all fields are terminated correctly. Figure 1-(a) shows the layout of an inductor simulated in Sonnet. The inductor simulation consists of four dielectric layers: a 1000 µm glass plate where the substrate is mounted on (ε_r = 3.9), a 300 µm sapphire substrate (ε_r = 9.8, Loss Tan = 1.0 x 10^{-4}), a 3 µm PMGI (1 <□ε_r <2) bridge post, followed by a 3000 µm air column (ε_r = 1) on the top. The dielectric constant of PMGI has negligible effect on the outcome of the simulations at the frequencies of interest and was fixed at ε_r = 2. The metal layers consist of a 3 µm interconnect and a 1 µm bridge-metal gold layers. The metal type was set to NORMAL in the Sonnet simulator and a current ratio of 0.5 or larger resulted in the most accurate ohmic loss in the simulations.

The capacitors were similarly modeled with the glass plate and the sapphire substrate, followed by a 130 nm SiN dielectric layer (ε_r = 7) between the capacitor plates, a 3 µm PMGI bridge post used for decreasing the parasitic capacitance due to the interconnect metal, and a 3000 µm air column on the top. All connections between the metal layers were made using vias through the dielectric layers. Figure 1-(b) shows the layout of a capacitor simulated in Sonnet.

IV. PASSIVE NETWORK SIMULATION AND MODELING

Initially, inductors of various sizes and geometries were simulated in Sonnet, and a high frequency equivalent circuit model was extracted from each simulation in order to create a simulation based inductor library. Figure 2-(a) shows the high frequency equivalent circuit model used for the inductors. The intrinsic section of the model consists of a pie network. The series resistor models the conductor loss in the metal, and the shunt resistors account for the loss in the substrate. All resistor models consist of a frequency dependent component that accounts for high frequency losses. The shunt capacitors are used to model the parasitic capacitance between the inductor and ground. These capacitors are the main factors in determining the inductor's self resonance. The capacitor parallel with the inductor is used for modeling the capacitance between the inductor's loops and its value is usually negligible. The pad parasitic elements are not needed for model extraction from the Sonnet simulations since Sonnet allows de-embedding up to the inductors terminals, and their corresponding values should be set to zero. They are only used for model extraction from measured data (test structures), in which case they need to be extracted separately using open and short pad structures prior to the intrinsic model extraction. Figure 2-(b) shows the extracted equivalent circuit vs. Sonnet simulation results for an inductor. The inductor used in this simulation has n = 2.5 turns, line thickness of 50 µm, line separation 30 µm, ground plane width of 300 µm, and ground plane separation of 150 µm.

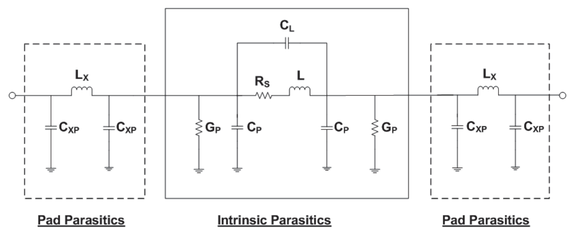

(a)

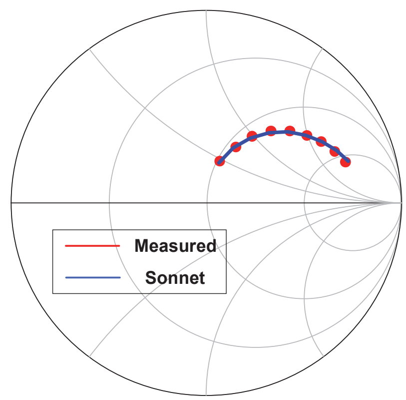

(b)

Fig. 2. (a) High frequency equivalent circuit model and (b) Sonnet simulation vs. extracted equivalent circuit model for an inductor.

The capacitor modeling and parameter extraction procedure is similar to that of inductors. Since our designed matching networks required only shunt capacitors, the capacitor simulations were carried out as one-terminal simulations with capacitors terminating in the ground plane. Figure 3-(a) shows the high frequency circuit model used for modeling capacitors in ADS. The model consists of the capacitor in series with a parasitic inductor. Due to the small size of the capacitors, the value of the series inductor is normally very small. The capacitance values scale quite well with geometry, and hence the creation of a capacitor library was unnecessary. Figure 3-(b) shows the extracted high frequency equivalent circuit vs. Sonnet simulation results for a capacitor.

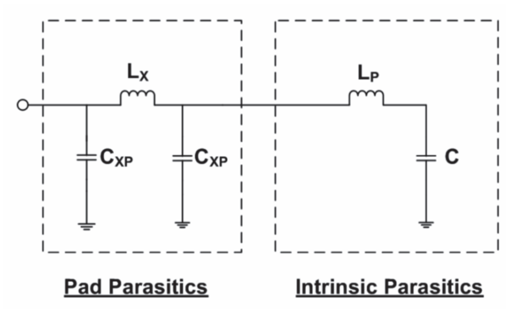

(a)

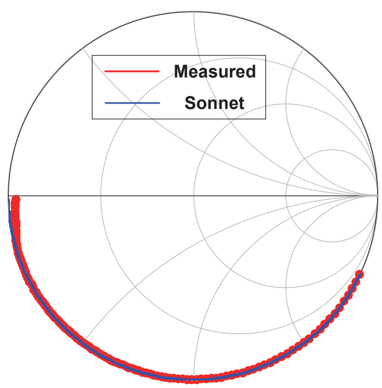

(b)

Fig. 3. (a) High frequency equivalent circuit model and (b) Sonnet simulation vs. extracted equivalent circuit model for a capacitor.

All parameter extractions were carried out in Agilent's advanced design systems (ADS) [11] with the aid of optimization routines. However, in general any other circuit simulation software capable of performing s-parameter simulations and basic optimization can be used to perform the parameter extractions for the equivalent circuits. The optimization routine used for the majority of the model extractions was the gradient method. However, the Quasi-Newton, least p-th, and hybrid routines also resulted in a good fit.

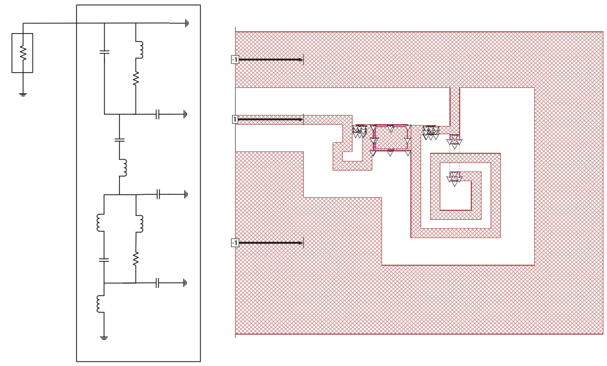

(a) (b)

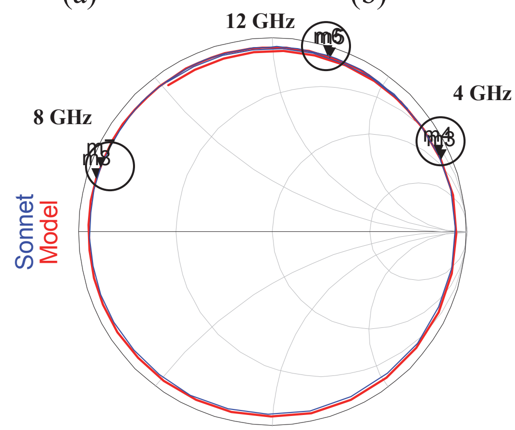

(c)

Fig. 4. (a) High frequency equivalent circuit, (b) Sonnet layout, and (c) Sonnet vs. circuit model s-parameter simulation results for the resonator.

V. MATCHING NETWORKS RESULT

In this section, the design of two output networks for a class F MMIC power amplifier is discussed. These relatively complex circuits serve as good examples for demonstrating the capabilities of Sonnet in correctly simulating their performance. The details of the class F amplifier operation are beyond the scope of this paper and here we will suffice in examining the performance of the designed output networks. The first output network consists of an L matching network and a resonator. The matching network and the resonator were initially designed separately, and then combined and optimized to obtain the complete output network. The optimization steps are needed to compensate for effects such as the changing of the current paths in the ground planes, the coupling between different components and the added interconnects when discrete lumped elements are combined together.

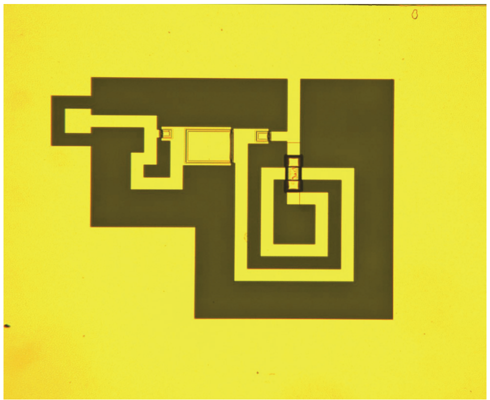

(a)

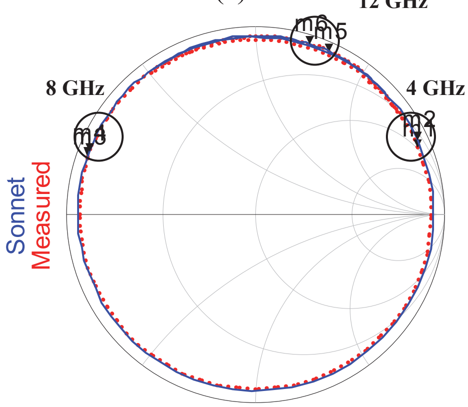

(b)

Fig. 5. (a) The fabricated resonator (b) Sonnet simulation vs. measured s-parameter results for the designed resonator.

Each section was initially designed in ADS using the equivalent circuit models for the inductors and capacitors, taking into the account all the parasitic elements. The layout of the designed networks were then simulated and optimized in Sonnet by adjusting the size and geometry of the capacitors and inductors as needed. Figure 4 shows the equivalent circuit model vs. Sonnet simulation s-parameter response obtained for the resonator circuit alone. We can see that excellent match is obtained over a wide frequency range. The fabricated resonator test structure is shown in fig. 5-(a), and the measured s-parameter result vs. the Sonnet simulation is shown in fig. 5-(b). We can see that excellent match is obtained between the measured data and the Sonnet simulation.

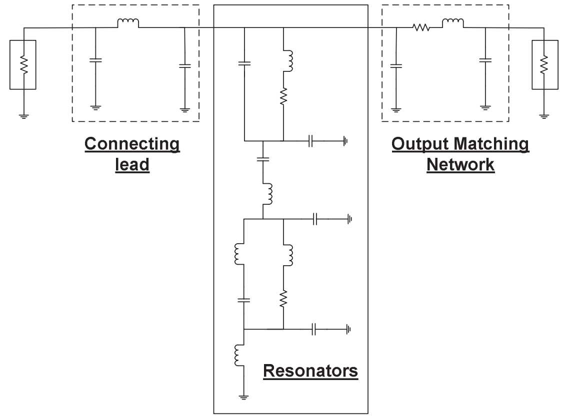

(a)

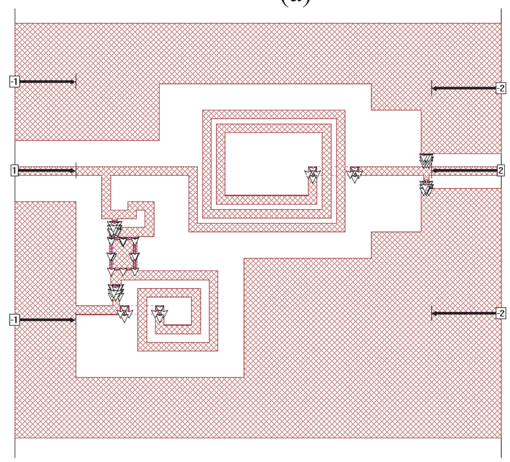

(b)

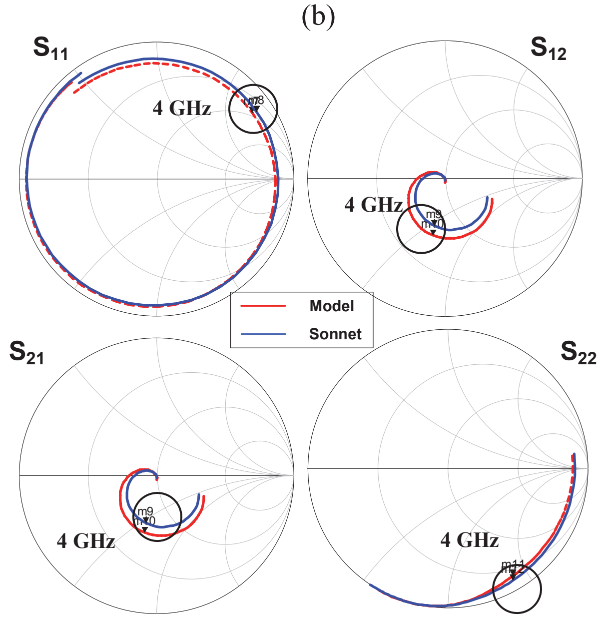

(c)

Fig. 6. (a) High frequency equivalent circuit, (b) Sonnet layout, and (c) Sonnet vs. circuit model s-parameter simulation results for the first output network.

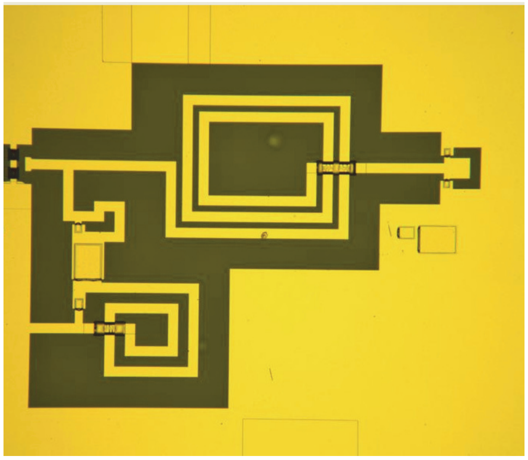

(a)

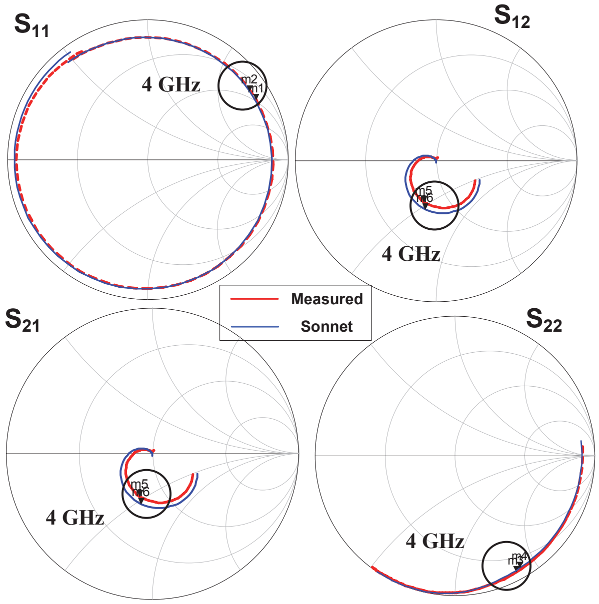

(b)

Fig. 7. (a) The fabricated output matching network (b) Sonnet simulation vs. measured s-parameter results for the first output network.

Finally, the two sections were combined to form the complete output network and final optimizations were carried out. At this point, the circuit becomes quite large and the simulations can take up a lot of time. However, due to the previous optimization of the individual sections the final optimization should not take much iteration. Figure 6 shows the equivalent circuit model vs. Sonnet simulation for the complete output matching network and fig. 7 shows the Sonnet simulation vs. measured results obtained from the fabricated circuit. From the two figures,

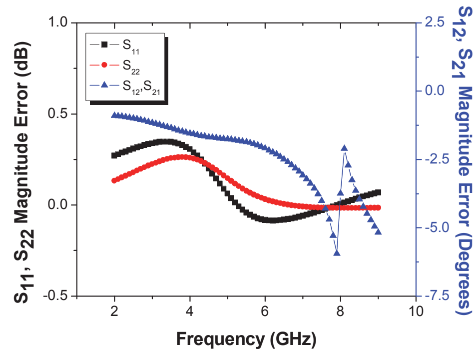

(a)

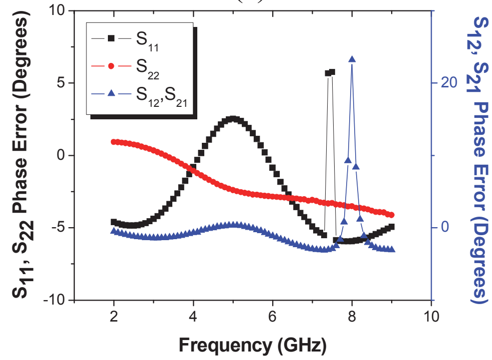

(b)

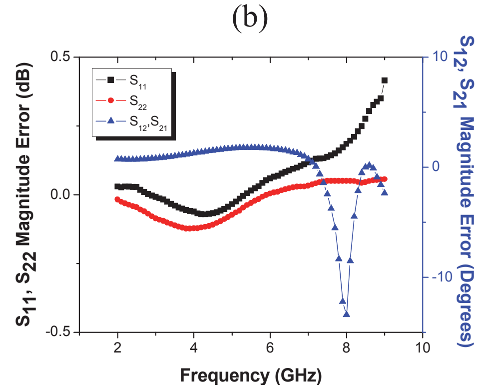

(c)

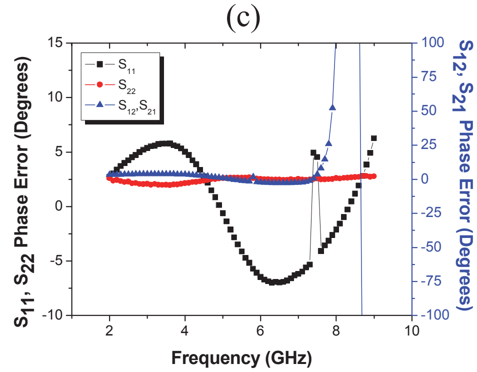

(d)

Fig. 8. Error plots of (a) magnitude and (b) phase of the equivalent circuit model vs. Sonnet simulation and (c) magnitude and (d) phase of measured data vs. Sonnet simulation for the first output network.

we can see that good overall fit is observed between the equivalent model simulation, the Sonnet simulation, and the measured data.

In order to better see the extent of agreement between the equivalent circuit model, Sonnet simulation, and measured data, the amplitude and phase errors are plotted in fig. 8. We can see that in both cases, S_{11} and S_{22} magnitude errors are less than ±0.5 dB and the phase errors are mostly within ±5 degrees. The S_{12} errors are small at lower frequencies. However, at higher frequencies as the magnitude of the S_{12} decreases rapidly, the magnitude and phase errors start to increase substantially. At such small values of S_{12} however, these errors have a negligible effect on the performance of the circuit.

The second output network consists of a π matching network and the same resonator structure at the drain side. Figure 9-(a) shows the equivalent circuit model and fig. 9-(b) shows the Sonnet layout of this output network. It can be seen from the layout that this output network is quite more complex compared to the previous example. Initially, there was a significant mismatch between the response of the equivalent circuit model and the Sonnet simulated s-parameters. After some analysis, it was determined that the mismatch is caused by the large asymmetry in the shape of ground planes on the layout, which has a substantial effect on the ground currents. This effect can be modeled in the equivalent circuit model by addition of small amounts of parasitic inductance in the ground paths, as marked on figure 9-(a). When these parasitic inductances were added to the equivalent circuit model, much improved match between the model and the Sonnet simulations was obtained, as shown in figure 9-(c). Figure 10 shows a picture of the fabricated output network and the comparison between the Sonnet simulations and the measured s-parameter response. We can see that good overall match between the Sonnet simulations and the measured data is obtained here as well.

Figure 11 shows the magnitude and phase error plots for the second output circuit. We can see that for this circuit, S_{11} and S_{22} magnitude errors are within ±1 dB and the phase errors vary from -5 to +25 degrees. These errors are notably larger than the errors seen in the previous circuit, reflecting the increased complexity of this circuit compared to the first circuit.

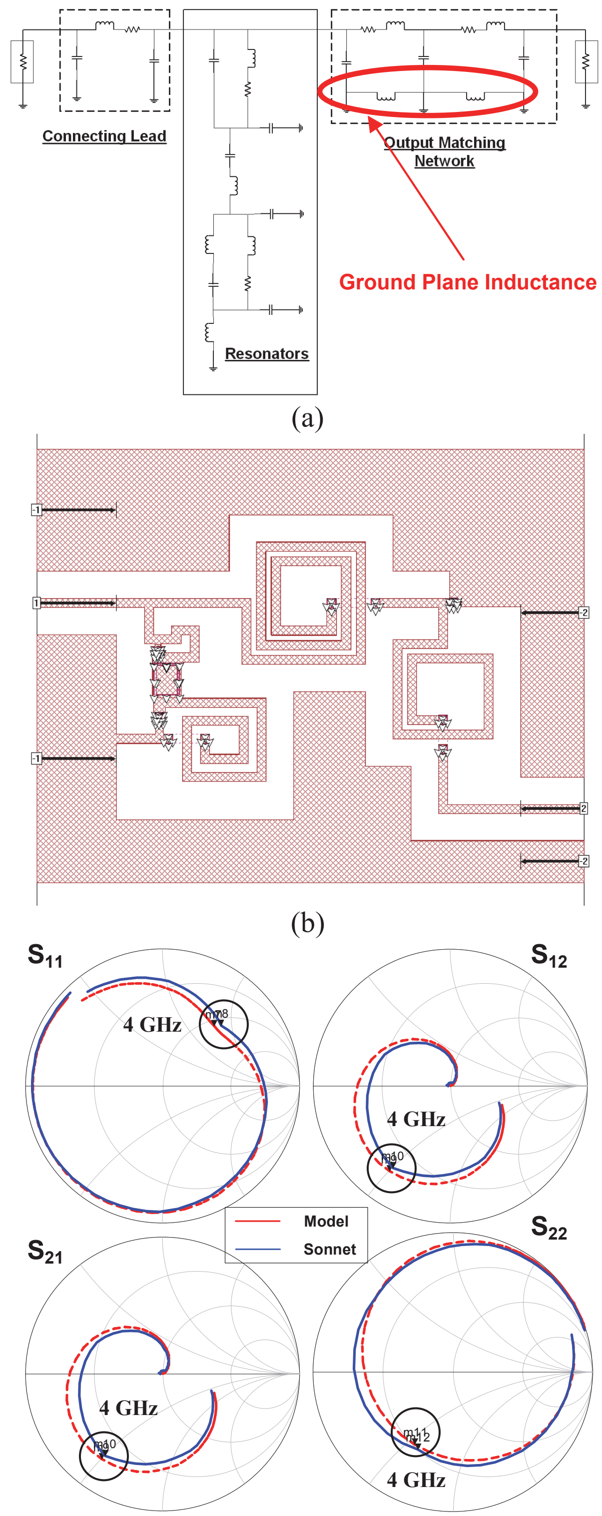

Fig. 9. (a) High frequency equivalent circuit, (b) Sonnet layout, and (c) Sonnet vs. circuit model s-parameter simulation results for the second output network.

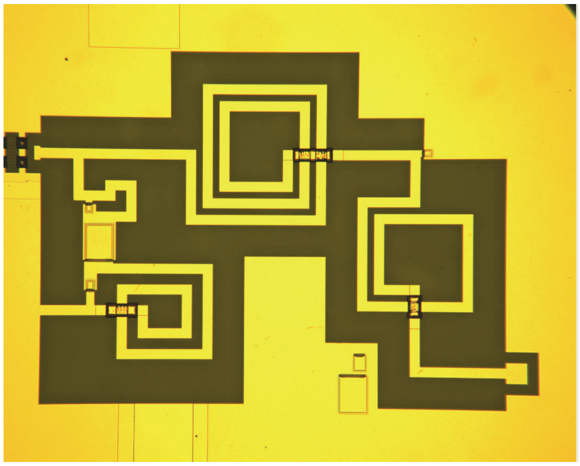

(a)

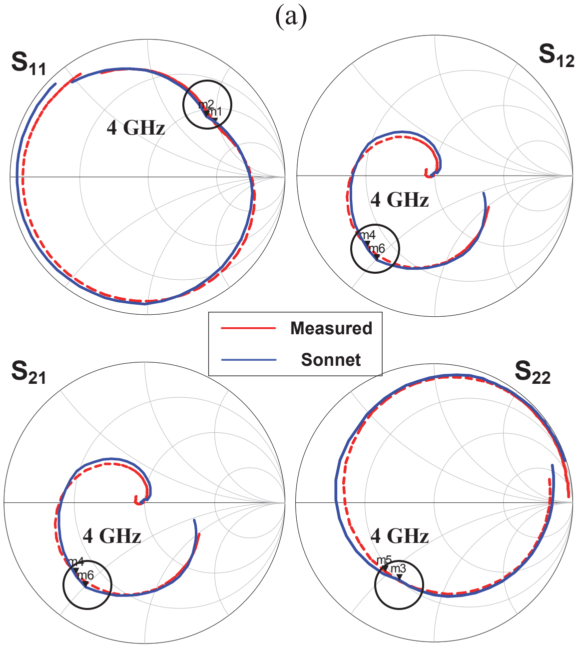

(b)

Fig. 10. (a) The fabricated output matching network and (b) Sonnet simulation vs. measured s-parameter results for the second output network.

The S_{12} errors are comparable to those of S_{11} and S_{22} at lower frequencies. Again at higher frequencies as the magnitude of S_{12} starts to decrease rapidly, the magnitude and phase errors increase substantially, but the effect of these errors are negligible on the performance of the circuit at such small values of S_{12}.

All simulations were performed on a Dell Precision 380 desktop containing a dual core 3.00 GHz Pentium D microprocessor and 3.5 GB of RAM. For all circuit simulations in Sonnet, the cell size was set to 2 μm in both X and Y directions, and the simulations were performed

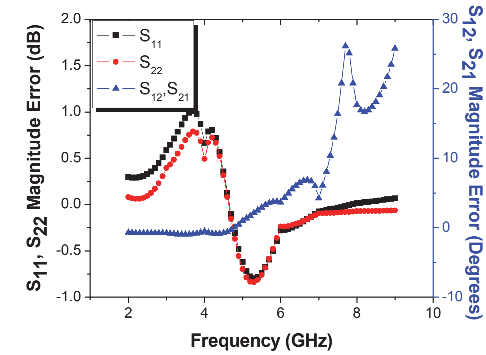

(a)

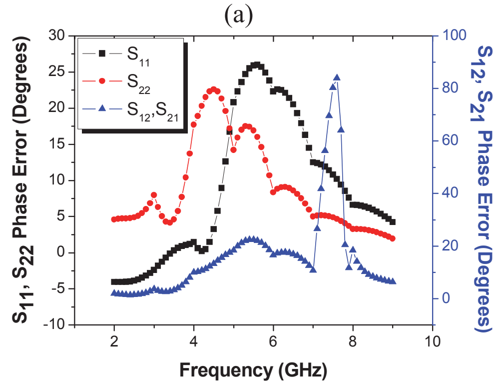

(b)

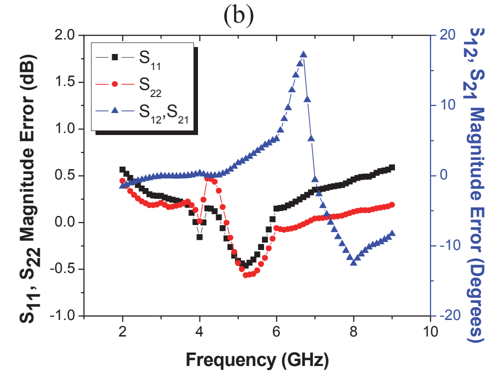

(c)

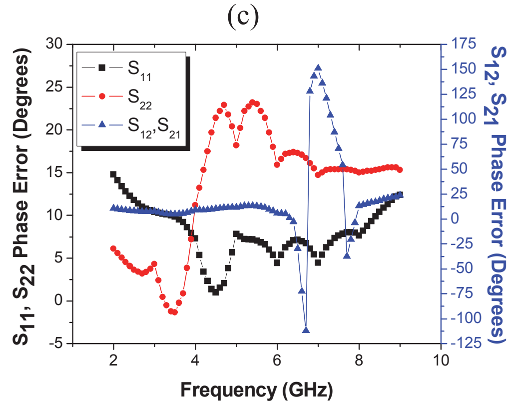

(d)

Fig. 11. Error plots of (a) magnitude and (b) phase of the equivalent circuit model vs. Sonnet simulation and (c) magnitude and (d) phase of measured data vs. Sonnet simulation for the first output network.

from 1 GHz to 16 GHz using the adaptive sweep (ABS) option. The resonator circuit layout shown in figure 4 has a box size of 2200 µm x 2200 µm in the Sonnet simulation window. The simulation time for this circuit was 101 minutes and 9 seconds. For the first output network shown in fig. 6, the final box size in the Sonnet simulation window was 2800 µm x 3000 µm and its simulation time was 224 minutes and 35 seconds. The second output network shown in fig. 9 has a box size of 3000 µm x 3000 µm and the simulation time for this circuit was 218 minutes and 42 seconds.

VII. CONCLUSION

Accurate modeling of CPW based passive components and design of matching networks using Sonnet was discussed in this paper. Initially, individual inductors and capacitors of various sizes and geometries were simulated in Sonnet, and a high frequency circuit model was extracted from each components. These extracted results were used to create a simulation-based inductor library and a scalable capacitor model, which were then used in designing complex passive circuits including resonators and matching networks. The systematic approach used for the design of complex passive networks resulted in obtaining accurate results with reduced time and effort spent. Based on these results Sonnet proved to be a powerful tool for accurate design of complex passive circuits.

ACKNOWLEDGMENT

The authors gratefully acknowledge funding from ONR MINE MURI project, monitored by Drs. P. Maki and H. Dietrich.

REFERENCES

[1] Y.-F. Wu, A.Saxler, M. Moore, R. P. Smith, S. Sheppard, P. M. Chavarkar, T. Wisleder, U. K. Mishra, and P. Parikh, "30-W/mm Gan HEMTs by Field Plate Optimization", *IEEE Electron Device Lett.*, vol. 25, no. 3, pp. 117-119, Mar. 2004.

[2] Y. Pei, R. Chu, N. A. Fichtenbaum, Z. Chen, D. Brown, L. Shen, S. Keller, S. P. DenBaars, and U K. Mishra, "Recessed Slant Gate AlGaN/GaN HEMTs with 20.9 W/mm at 10 GHz," *Japanese Journal of Applied Physics*, vol. 46, no. 45, pp. L1087-L1089 (2007).

[3] J. S. Moon, D. Wong, M. Hu, P. Hashimoto, M. Antcliffe, C. McGuire, M. Micovic, and P. Willadson, "55% PAE and High Power Ka Band GaN HEMTs with Linearized Transconductance via n+ GaN Source Contact Ledge," *IEEE Elec. Device Lett.*, vol. 29, no. 8, pp. 834-837, 2008.

[4] H. Xu, S. Gao, S. Heikman, S. Long, U. K. Mishra, R. A. York, " A High Efficiency Class E GaN HEMT Power Amplifier at 1.9 GHz," *IEEE Microwave and Component Letters*, vol. 16, no. 1, pp. 22-24, 2006.

[5] S. Gao, H. Xu, U. K. Mishra, and R. A. York, "MMIC Class-F Power Amplifiers using Field-Plated AlGaN/GaN HEMTs", *IEEE Compound Semiconductor Integrated Circuit Symp.,* 2006.

[6] The UCSB Nanofabrication Facility Website: http://www.nanotech.ucsb.edu/index.php?option=com_content&view=article&id=45&Itemid=27

[7] http://www.sonnetsoftware.com

[8] R. F. Harrington, *Field Computation by Moment Methods*, reprinted by IEEE Press, 1993.

[9] J. C. Rautio and R. F. Harrington, "An Electromagnetic Time-Harmonic Analysis of Shielded Microstrip Circuits," *IEEE Trans. Microwave Theory Tech.,* vol. MTT-35, pp. 726-730, Aug. 1987.

[10] http://www.sonnetsoftware.com/products/sonnet-suites/how-em-works.html

[11] http://www.home.agilent.com/agilent/product.jspx?nid=-34346.0.00&cc=US&lc=eng

Valiallah Zomorrodian received the B.S. and M.S. degree in Electrical and Computer Engineering from University of Houston, Houston, TX, in 2000 and 2004, respectively. He is currently pursuing a Ph.D. degree in Electrical and Computer Engineering from the University of California Santa Barbara (UCSB). His research interests include large signal and noise modeling of AlGaN/GaN HEMTs and design and fabrication of nonlinear Microwave Monolithic Integrated

Circuits (MMICs) using AlGaN/GaN HEMT technology.

Umesh K. Mishra (S'80–M'83–SM'90–F'95) received the B.Tech. from the Indian Institute of Technology (IIT) Kanpur, India, in 1979, the M.S. degree from Lehigh University, Bethlehem, PA in 1980, and the Ph.D. degree from Cornell University, Ithaca, NY, in 1984, all in Electrical Engineering. He has been with various laboratory and academic institutions, including Hughes Research Laboratories, Malibu, CA, The University of Michigan at Ann Arbor, and General Electric, Syracuse, NY, where he has made major contributions to the development of AlInAs–GaInAs HEMTs and HBTs. He is currently a Professor and the Department Chair at the Department of Electrical and Computer Engineering, University of California at Santa Barbara (UCSB). He has authored or coauthored over 450 papers in technical journals and conferences. He holds nine patents. His current research interests are in oxide-based III–V electronics and III–V nitride electronics and optoelectronics. Dr. Mishra was a corecipient of the Hyland Patent Award presented by Hughes Aircraft and the Young Scientist Award presented at the International Symposium on GaAs and Related Compounds.

Robert A. York (S'85–M'89–SM'99–F'09) received the B.S. degree in Electrical Engineering from the University of New Hampshire, Durham, in 1987, and the M.S. and Ph.D. degrees in Electrical Engineering from Cornell University, Ithaca, NY, in 1989 and 1991, respectively.

He is currently a Professor of Electrical and Computer Engineering with the University of California at Santa Barbara (UCSB), where his group is currently involved with the design and fabrication of novel microwave and millimeter-wave circuits, high-power microwave and millimeter-wave amplifiers using spatial combining and wide-bandgap semiconductor devices, and application of ferroelectric materials to microwave and millimeter-wave circuits and systems.

Dr. York was the recipient of the 1993 Army Research Office Young Investigator Award and the 1996 Office of Naval Research Young Investigator Award.

Design and SAR Reduction of the Vest Antenna using Metamaterial for Broadband Applications

M. Fallah[1], A. A. Heydari[2], A. R. Mallahzadeh[2], and F. H. Kashani[1]

[1]Faculty of Electrical Engineering
Iran University of Science and Technology, Tehran, Iran

[2]Faculty of Engineering
Shahed University, Tehran, Iran
mohsen_fallah@ee.iust.ac.ir, amirabbas.heydari@gmail.com, mallahzadeh@shahed.ac.ir,
kashani@iust.ac.ir

Abstract **─** One of the most important obstacles that portable antennas are facing is their harmful effect on the user's body. In this paper, besides proposing a UWB vest antenna with a bandwidth of at least 500MHz, we try to reduce the specific absorption ratio (SAR) due to the proposed antenna on the human body. In order to achieve the mentioned goal, we modeled the human body after designing the antenna. In order to have simulation results closer to reality, we have used a 3-layer model of the human body instead of the 1-layer model. In our model of the human body, all of the body parts, except the torso, are modeled with three layers of bone, fat, and muscle. Since the torso has a different structure from other body parts and is close to the place of the antenna feed, we modeled it using four layers of air, bone, fat and muscle. As the next step in our simulation process, the antenna was installed on the human body and then the antenna parameters and its SAR were obtained again. In the last stage, SAR due to the proposed antenna is reduced using metamaterial.

Index Terms **─** Meta material antenna, SAR reduction, vest antenna.

I. INTRODUCTION

Soldiers, police officers, firefighters, forest workers, etc. need "hands free" operation for their wireless equipment. A solution is to use antennas borne or worn on their helmet (as a helmet antenna) or on their upper torso (as a vest antenna) [1, 2]. The process of designing the RF vest antenna started with the analysis of ultra wideband antenna concepts, followed by computer simulation of potential designs. An optimum design was chosen based on the input impedance and voltage standing wave ratio (VSWR). In [3], an antenna with a bandwidth of 360MHz was designed; in [4], the design of a vest antenna with a VSWR less than 3.1 for the 100 to 500 MHz frequency band is shown; design of an ultra wideband vest antenna with a VSWR less than 3 for frequencies 31 to 475 MHz can be found in [5]; also, a ZERO VISUAL SIGNATURE vest antenna with VSWR<3 for the frequency range of 50 and 500 MHz is reported in [6].

Ongoing work includes the improvement of the computer model, design optimization, fabrication, and SAR reduction [6].

Natural low-frequency EM fields come from two main sources: the sun and thunderstorm activities. But in the last 100 years, man-made fields at much higher intensities and with a very different spectral distribution have altered this natural EM background in ways that are not yet fully understood. For example, in the design of the combat wear integration (COMWIN) RF vest antenna in addition to providing appropriate frequency range to establish wireless communication, we need to protect the health of the men that use and carry the antenna. There is strong challenge in designing body worn antennas with the appropriate frequency range and at the same time protecting the human body from harmful effects.

Over the last fifteen years, many authors have investigated the SAR with human head due to the complexity and large scale involved in such kinds

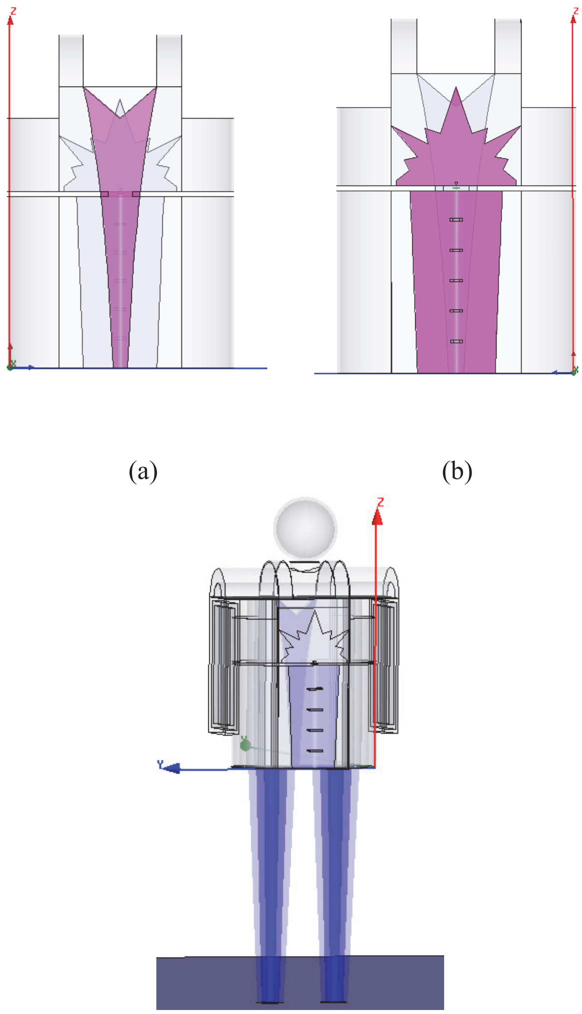

(a) (b)

(c)

Fig. 1. Schematic of the vest antenna (a) front view, (b) back view, and (c) 3D view.

of problems [11-19]. Recently, lots of attention has been paid to the reduction of peak SAR within materials and metamaterials. In [12], a ferrite sheet was adopted as a protection attachment between the antenna and the human head. A reduction over 13% for the spatial peak SAR over 1 gm averaging was achieved. Study on the effects of attaching materials and metamaterials for SAR reduction is presented in [19], and it was concluded that the position of shielding played an important role in the reduction effectiveness.

Recently, metamaterials have inspired great interests due to their unique physical properties and novel application [20, 21]. Metamaterials denote artificially constructed materials having

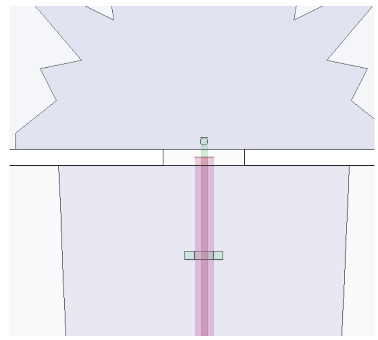

(a)

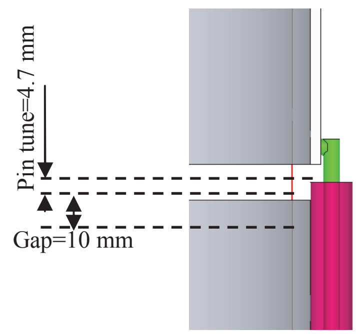

(b)

Fig. 2. The configuration of the feed region (a) side view and (b) front view.

electromagnetic properties not generally found in nature. Two important parameters, electric permittivity and magnetic permeability, determine the response of the materials to the electromagnetic propagation. Mediums with negative permittivity can be obtained by arranging the metallic thin wires periodically [7, 22-31]. On the other hand, an array of split ring resonators (SRRs) can exhibit negative effective permeability [32]. Metallic thin wires and SRRs are narrow-banded and lossy materials. When one of the effective medium parameters is negative and the other is positive, the medium will display as stop band. The metamaterials is on a scale less than the wavelength of radiation and use slow density of metal. The structures are resonant due to internal capacitance and inductance. The stop band of metamaterials can be designed as operation bands of cellular phone while the size of metamaterials is similar to that of a cellular phone. Metamaterials are designed on circuit boards so it may be easily integrated to the cellular phone [33]. Simulation of

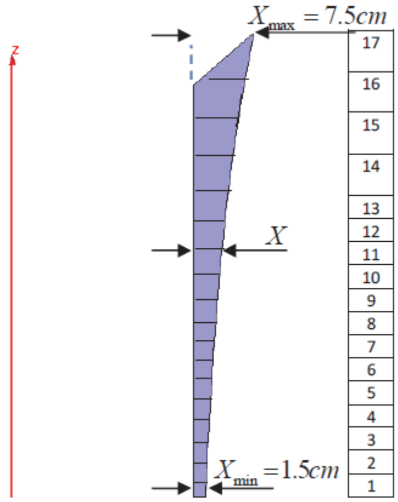

Fig. 3. Schematic of the strip in front side of the vest antenna.

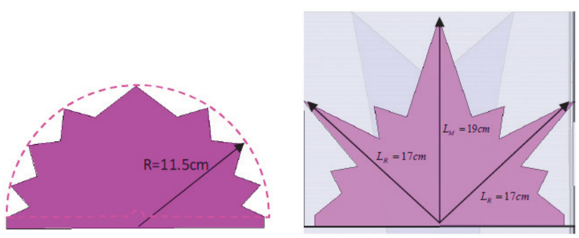

Fig. 4. The initial pattern (a) upper part of the vest antenna and (b) final pattern.

wave propagation into metamaterials was proposed in [34].

Another approach for reducing the SAR is the use of a directional or reflectional antenna [35, 36]. In [17], a perfect electric conductor (PEC) reflector was arranged between a human head and the driver of a folded loop antenna. The result showed that the radiation efficiency can be enhanced and the peak SAR value can be reduced. Metamaterial have inspired great interests due to their unique physical properties and novel applications [35, 40]. The motivation of this paper is to design metamaterial to investigate the potential reduction of the peak SAR value.

In this paper, a broadband vest antenna with a bandwidth of 160% ranging for VSWR<3 with reduced SAR on the human body by using metamaterial is proposed. In order to reduce the vest antenna SAR appropriate metamaterial namely TW type is used.

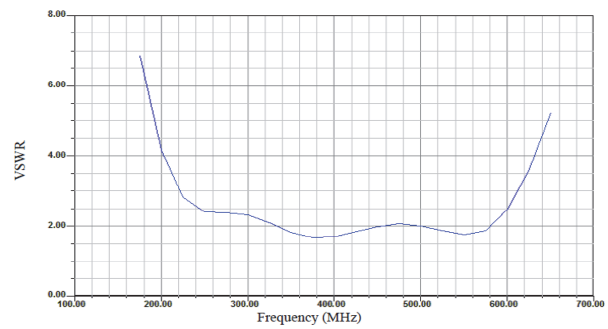

Fig. 5. Simulated VSWR of the designed vest antenna.

In section two of this paper, first we designed an ultra wideband vest antenna. In section three, we modeled the human body using four layers in the abdominal region and three layers in other parts of the body. In section four, we designed metamaterial to reduce the SAR of the antenna, and finally in section five, we measured the specific absorption ratio (SAR) of the vest antenna in the presence of the designed metamaterial.

II. DESIGNING THE UWB VEST ANTENNA

For borne or worn antenna, consider the vest antenna and by shaping obtained the present structure. The antenna is installed on a polyester vest with a thickness of 5mm. It consists of two parts, the upper part and the lower part. Both of the mentioned parts are installed on the back side of the vest. There is a conductive strip in the front side of the vest.

Figure 1 shows the vest antenna from the front side and the back side. The antenna is fed through a coaxial cable in a way that the core of the cable is connected to the upper part of the antenna and the cable shield is connected to the lower part, as shown in Fig. 2.

In order to increase the antenna bandwidth, exponential equations are used in designing the lower part of the antenna and the metal strip in the front side of the antenna. Strip width in the lower part of the antenna starts from 15cm to 17.8cm.

The in front one starts from 3cm to 15cm. For example, in front strip the first 13 components are 2.95cm and the other 4 components are 3.83cm.

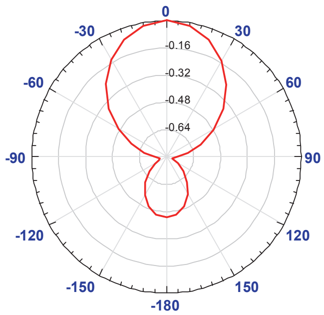

(a)

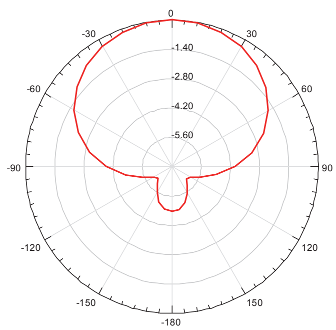

(b)

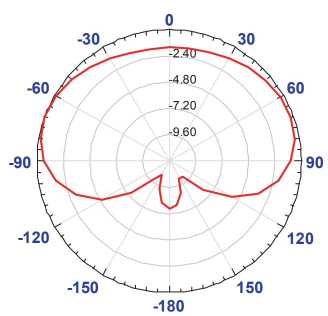

(c)

Fig. 6. Simulated radiation pattern in the horizontal plane at (a) 100MHz, (b) 350MHz, and (c) 600MHz.

$$X = \frac{X_{\min}}{2} e^{az}. \tag{1}$$

$$a = \frac{1}{h.\ln(\frac{X_{\max}}{X_{\min}})}. \tag{2}$$

A jagged shape with the following specifications is used in the design of the upper part of the antenna. The initial design consisted of a semicircle. The maximum point of each jag was

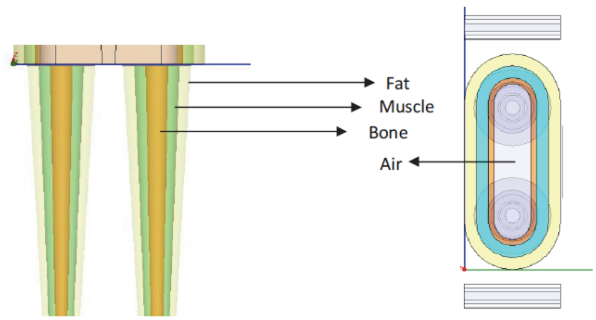

(a) (b)

Fig. 7. The modeled human body (a) legs and (b) torso.

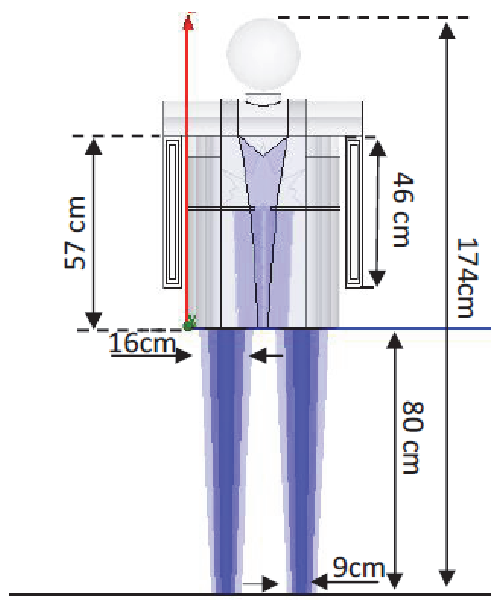

Fig. 8. The configuration of the final modeled of the human body.

located on the circumference of the semicircle. The following shape was obtained, after tuning the initial shape for having a better VSWR. The VSWR of the tuned antenna is shown in Fig. 5. As shown in Fig. 5, the antenna bandwidth is about 400MHz. The radiation pattern of the vest antenna is shown in Fig. 6. The results of the simulation and tuning of the variables are obtained by Ansoft HFSS v.11 [41].

III. SIMULATION RESULT OF THE VEST ANTENNA ON A HUMAN BODY

In this section, we are going to discuss the modeling of the human body. In order to have the closest possible results to reality, the dimensions of the modeled human body are according to the typical person.

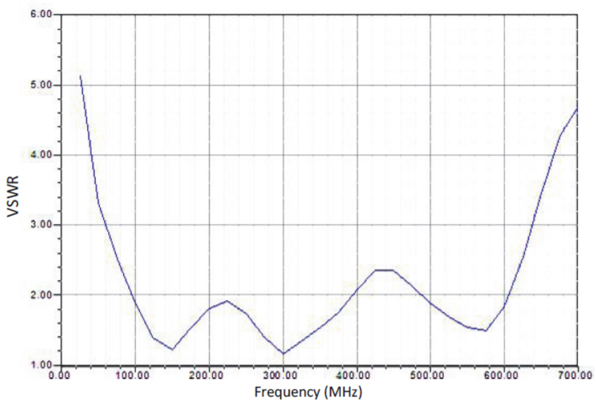

Fig. 9. Simulated VSWR of the vest antenna on the human body.

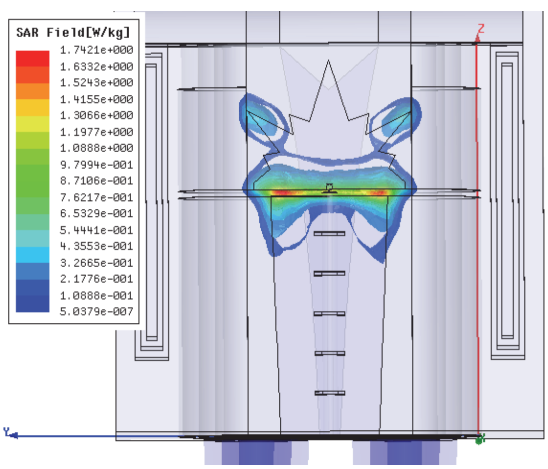

Fig. 10. The simulated average SAR on the human body at 500MHz.

Table 1: The electromagnetic characteristics of the main parts of the human body at 500MHz [8]

Material	ε	σ	***Loss tangent***
Bone	12.946	0.10047	0.27901
Fat	5.5444	0.042793	0.27748
Muscle	56.445	0.82245	0.52383
Brain Grey Matter	55.833	0.77907	0.50165
Brain White Matter	41.004	0.47391	0.41551

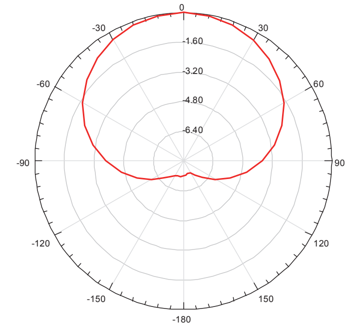

(a)

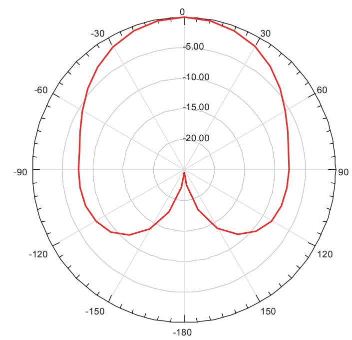

(b)

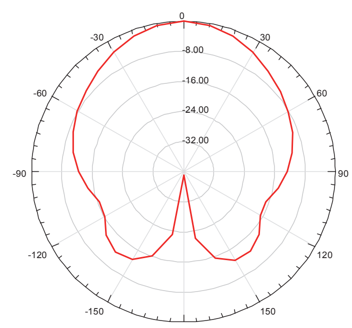

(c)

Fig. 11. Radiation pattern in the horizontal plane at (a) 100MHz, (b) 350MHz, and (c) 600MHz.

As shown in Fig. 7, the legs are constructed of three layers of bone, muscle, and fat. The height of the legs is about 80cm. In the next stage, the torso and the upper part of the shoulders are modeled. Since this part of the body is closer to the antenna and its feed, a more accurate modeling is used. Because the torso has a different structure from the rest of the body (the existence of air inside the lungs), four layers are used for modeling this part of the body as shown in Fig. 7. The final model is

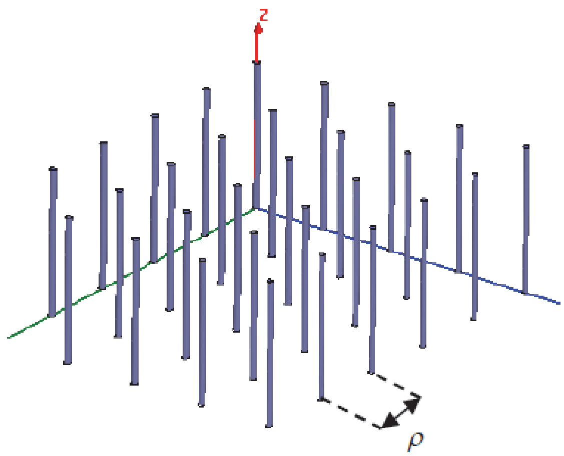

(a)

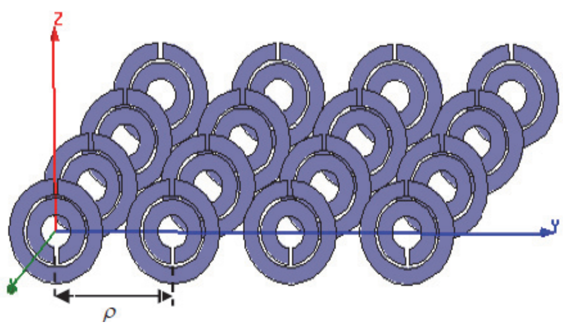

(b)

Fig. 12. Metamaterial structures, (a) TW structure and (b) SRR structure.

depicted in Fig. 8. The electromagnetic characteristics of the main parts of the human body in frequency of 500MHz are listed in Table 1. In spite of the suitable VSWR, the SAR in the body parts close to the antenna, such as the waist is much higher than the standard limits.

According to the IEEE standard, the average SAR in the human body must not be more than 0.08 W/Kg [9, 10]. But this limit is reduced to 0.02 W/Kg for the region close to the head.

As shown in Fig. 10, the obtained peak SAR, due to the proposed antenna, on the human body is about 1.74 W/Kg, which is approximately 22 times the standard limit.

In the next section, we try to use metamaterial in order to reduce the SAR of the vest antenna on a human body. This method was recently used for decreasing the SAR in cell phones [19]. Radiation pattern is shown in Fig. 11 in azimuth for various frequencies.

IV. METAMATERIAL MODELING

Metamaterials are broadly defined as artificial effectively homogeneous electromagnetic structures with unusual properties not readily found in the nature. In these structures, the average cell size is much smaller than the wavelength of the operational frequency in the free space.

A. Designing the appropriate metamaterial for the proposed vest antenna

For designing the needed metamaterial, we consider the operational frequency of the vest antenna and the design formulas of metamaterial, with ε > 0 μ < 0 for a split-ring resonator (SRR) structure and ε < 0 μ > 0 for a thin-wire (TW) structure, we chose the second type which is TW. You can see the structures of these two types of metamaterial in Fig. 12.

B. SRR design procedure

The permeability of a SRR structure can be calculated using:

$$\mu_r(\omega) = 1 - \frac{F\omega^2}{\omega^2 - \omega_{0m}^2 + j\omega\zeta}$$

$$\mu_r(\omega) = 1 - \frac{F\omega^2(\omega^2 - \omega_{0m}^2)}{(\omega^2 - \omega_{0m}^2)^2 + (\omega\zeta)^2} \tag{3}$$

$$+ j\frac{F\omega^2\zeta}{(\omega^2 - \omega_{0m}^2)^2 + (\omega\zeta)^2}.$$

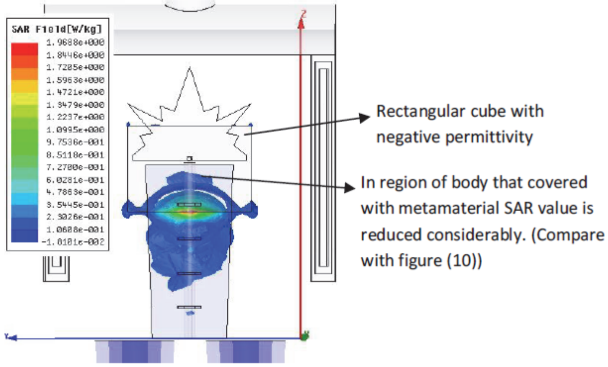

Fig. 13. Simulated average SAR in the presence of the material with a negative ε_r.

Wherein, $F=\pi(a/p)^2$, a is the inner radius of the smaller ring, $\omega_{0m}=c\sqrt{\dfrac{3p}{\pi\ln(2wa^3/\delta)}}$ is the magnetic resonance frequency in which w is the thickness of the rings and δ is the radial distance between the rings. Also, $\xi=2pR^{/}/a\mu_0$ is the damping factor which is related to the loss in the metal, with $R^{/}$ as the metal resistance in the unit length.

For finding the frequency range in (3) in which μ_r < 0, the metal loss is supposed to be small. Therefore,

$$\mu_r<0 \ \ for \quad \omega_{0m}<\omega<\frac{\omega_{0m}}{\sqrt{1-F}}=\omega_{pm}, \tag{4}$$

where ω_{pm} is called the magnetic plasma frequency.

According to (4), the antenna operational frequency must be higher than ω_{0m} for having a negative μ_r, but considering the fact that for SRRs with common dimensions this frequency is about several GHz, using SRRs in our design is not feasible [42]. The attempts made in [10] for using SRR to reduce the SAR of the cell phones on the human head, show that a layer of SRR with a thickness of 25mm can reduce the SAR for only about 27% in the GSM900 frequency band, while the same SRR used in the GSM1800 frequency band can reduce the SAR up to 38%.

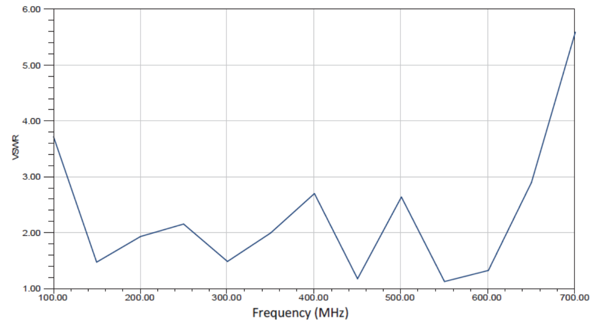

Fig. 14. Simulated VSWR of the proposed vest antenna after reduced SAR.

C. TW design procedure

The relative permittivity of the thin wire can be calculated with the following formulation:

$$\varepsilon_r(\omega)=1-\frac{\omega_{pe}^2}{\omega^2+i\omega\zeta}. \tag{5}$$

In (5), $\omega_{pe}=\sqrt{\dfrac{2\pi c^2}{p^2\ln(\frac{p}{a})}}$ is the electric plasma frequency where c is the light velocity and a is the radius of the wires. $\xi=\dfrac{\varepsilon_0(p\omega_{pe}/a_0)^2}{\pi\sigma}$ is the damping factor with σ as the metal conductivity. From (5) we have:

$$\mathrm{Re}(\varepsilon_r)<0 \ \ for \quad \omega^2<\omega_{pe}^2-\xi^2. \tag{6}$$

Equation (6) gives the frequency range for a negative permittivity. If we ignore the loss, we will have:

$$\varepsilon_r<0 \quad for \quad \omega<\omega_{pe}. \tag{7}$$

From (6), it is evident that if the operational frequency is less than the electric plasma frequency, the ε_r will be negative [42]. The next step instead of the full modeling of the metamaterial, we used a rectangular cube with a

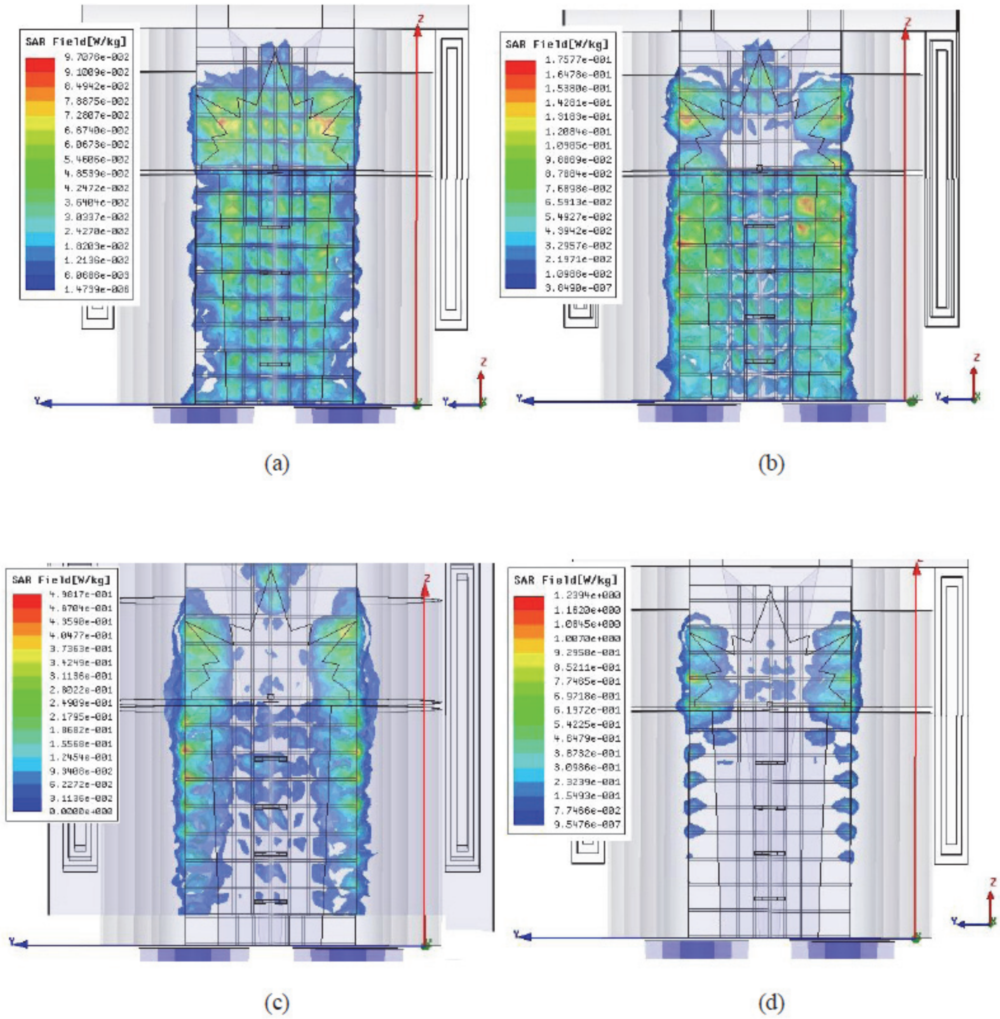

Fig. 15. Simulated SAR in the presence of the metamaterial at (a) 100MHz, (b) 350MHz, (c) 500MHz, and (d) 600MHz.

variable ε_r that it's ε_r was obtained from equation (5).

As illustrated in Fig. 13, using a material with a negative ε_r between the human body and the antenna, the SAR due to the vest antenna in the regions of the body covered with metamaterial is reduced considerably. So we will continue modeling TW metamaterial in our project.

In modeling of the TW metamaterial instead of using wires with a radius equal to a, we used strips with a width of $2a$. In order to have a better compatibility with the antenna structure and also reducing the project runtime, we used the strips in the TW structure. In this article, we used strips with a width of 4mm and the distance between strips is 24mm for the proposed antenna's operational frequency.

V. RESULTS

In this part, vest antenna simulations results are presented after modeling metamaterial. Tuned VSWR of the antenna is shown in Fig. 14. The simulation results show that the final design have the wide impedance bandwidth of approximately 160% ranging from 100MHz to 640MHz for VSWR<3. Comparing to the condition without any metamaterial, the bandwidth variation of the antenna is negligible.

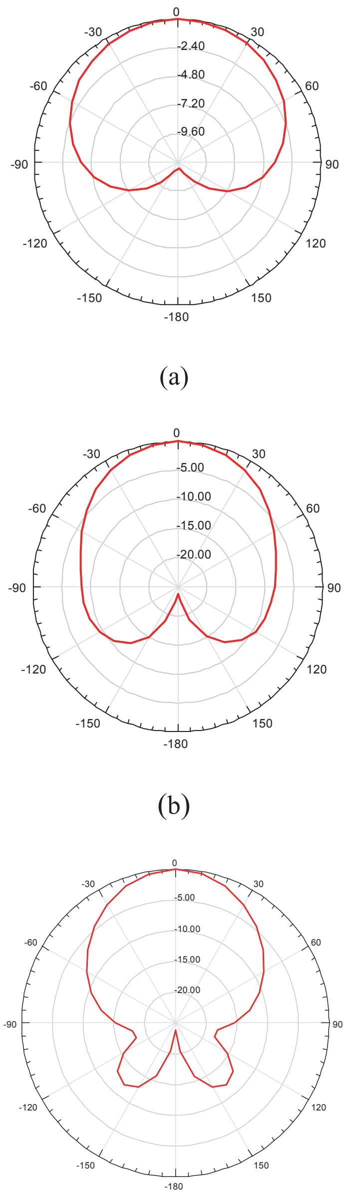

(a)

(b)

(c)

Fig. 16. Simulated radiation pattern in the horizontal plane at (a) 100MHz, (b) 400MHz, and (c) 600MHz.

Also, as it is shown in Fig. 13, the metamaterial substance prevents the waves from penetrating the human body. The parts of the body in which the SAR is higher than the standard limits are located on the ridges of the human body shape. On the other hand, the antenna VSWR is almost unaffected by the metamaterial and the antenna bandwidth is about 530MHz after implementing the SAR reduction procedure. The simulated radiation pattern of the vest antenna after the SAR reduction procedure is shown in Fig. 16.

VI. Conclusion

In this article, a broadband vest antenna with a bandwidth of 160% ranging from 110 MHz to 630 MHz for VSWR<3 is proposed. To do so, the human body was modeled after designing the antenna. To this end, a 3-layer model of the human body has been used instead of the 1-layer model. As the next step in our simulation process, the antenna was installed on the human body and then the antenna parameters and its SAR were measured again. At the last stage, in order to reduce the vest antenna SAR appropriate metamaterial namely TW type is used. It can be seen that SAR due to the vest antenna on the human body is decreased considerably to 1.2 while the VSWR bandwidth and radiation pattern of the antenna is not changed approximately.

REFERENCES

[1] J. J. H. Wang, "Broadband Omni Directional Helmet Antennas," *IEEE AP-S Int. Symp.,* pp. 2129- 2132, 9-14 July 2006.

[2] J. J. H. Wang and D. J. Triplett, "A Multioctave Broadband Vest Antenna Based on SMM Antenna Technology," *IEEE AP-S Int. Symp*., pp. 2125- 2128, 9-14 July 2006.

[3] J. E. Lebaric, R. W. Adler, and T. M. Gainor, "Ultra-Wideband Radio Frequency Vest Antenna," *MILCOM 2000, 21st Century Military Communications Conference Proceedings,* vol. 2, pp. 588-590, 2000.

[4] R. Abramo, R. Adams, F. V. Canez, H. Pace, and P. Haglind, "Fabrication and Testing of the COMWIN Vest Antenna," *MILCOM 2000, 21st Century Military Communications Conference Proceedings***,** vol. 1, pp. 595-598, 2000.

[5] R. C. Adams, "Testing and Integration of the COMWIN Antenna System," *MILCOM 2002, Proceedings,* vol. 1, pp. 637-641, 7-10 Oct. 2002.

[6] J. E. Lebaric, R. W. Adler, and M. E. Limbert, "Ultra-Wideband, Zero Visual Signature RF Vest Antenna for Man-Portable Radios," *MILCOM 2001, Communications for*

Network-Centric Operations: Creating the Information Force. IEEE, vol. 2, pp. 1291-1294, 2001.

[7] J. B. Pendry, A. J. Holden, D. J. Robbins, and W. J. Stewart, "Low Frequency Plasmons in Thin-Wire Structures," *J. Phys. Condens. Matter*, vol. 10, pp. 4785-4809, 1998.

[8] of ITALIAN NATIONAL REASEARCH CONCIL, Institute for Applied Physics*, Calculation of Dielectric Property of Human Tissue in the Frequency Range 10 Hz - 100 GHz* http://www.ifac.cnr.it, http://niremf.ifac.cnr.it/tissprop/

[9] IEEE C95.1-2005, "IEEE Standards for Safety Levels with Respect to Human Exposure to Radio Frequency Electromagnetic Fields, 3 kHz to 300 GHz," *Institute of Electrical and Electronics Engineers, New York, NY*, 2005.

[10] International Non-Ionizing Radiation Committee of the International Radiation Protection Association, "Guidelines on Limits on Exposure to Radio Frequency Electromagnetic Fields in the Frequency Range from 100 kHz to 300 GHz," *Health Physics,* vol. 54, no. 1, pp. 115-123, 1988.

[11] L. C. Fung, S. W. Leung, and K. H. Chan, "An Investigation of the SAR Reduction Methods in Mobile Phone Application," *IEEE International Symposium on EMC*, vol. 2, pp. 656–660, Aug. 2002.

[12] J. Wang and O. Fujiwara, "FDTD Computation of Temperature Rise in the Human Head for Portable Telephones," *IEEE Trans. Microwave Theory Tech.,* vol. 47, no. 8, pp. 1528-1534, Aug. 1999.

[13] J. Wang and O. Fujiwara, "Reduction of Electromagnetic Absorption in the Human Head for Portable Telephones by a Ferrite Sheet Attachment," *IEICE Trans. Commun.,* vol. E80-B, no. 12, pp. 1810-1815, Dec. 1997.

[14] S. Khalatbari, D. Sardari, A. A. Mirzaee, and H. A. Sadafi, "Calculating SAR in Two Models of the Human Head Exposed to Mobile Phones Radiations at 900 and 1800 MHz," *PIERS Online,* vol. 2, no. 1, pp. 104-109, 2006.

[15] A. Hirata, K. Shirai, and O. Fujiwara, "On Averaging Mass of SAR Correlating with Temperature Elevation Due to a Dipole Antenna," *Progress in Electromagnetics Research, PIER 84,* pp. 221-237, 2008.

[16] K. R. Mahmoud, M. El-Adawy, S. M. M. Ibrahem, R. Bansal, and S. H. Zainud-Deen, "Investigating the Interaction Between a Human Head and a Smart Handset for 4g Mobile Communication Systems," *Progress in Electromagnetics Research C,* vol. 2, pp. 169-188, 2008.

[17] N. K. Kouveliotis, S. C. Panagiotou, P. K. Varlamos, and C. N. Capsalis, "Theoretical Approach of the Interaction Between a Human Head Model and a Mobile Handset Helical Antenna using Numerical Methods," *Progress in Electromagnetics Research, PIER 65*, pp. 309-327, 2006.

[18] M. A. Ebrahimi-Ganjeh and A. R. Attari, "Interaction of Dual Band Helical and Pifa Handset Antennas with Human Head and Hand," *Progress in Electromagnetics Research, PIER* 77, pp. 225-242, 2007.

[19] J. N. Hawang and F.-C. Chen, "Reduction of the Peak SAR in the Human Head with Metamaterials," *IEEE Trans. Antennas Propagt.*, vol. 54, no. 12, pp. 3763-3770, 2006.

[20] E. Ozbay, K. Aydin, E. Cubukcu, and M. Bayindir," Transmission and Reflection Properties of Composite Double Negative Metamaterials in Free Space," *IEEE Trans. Antennas Propagt.,* vol. 51, no. 10, pp. 2592-2595, Oct. 2003.

[21] R. W. Ziolkowski, "Design, Fabrication, and Testing of Double Negative Metamaterials," *IEEE Trans. Antennas Propagt.,* vol. 51, no. 7, pp. 1516-1529, July 2003.

[22] M. M. Sigalas, C. T. Chan, K. M. Ho, and C. M. Soukoulis, "Metallic Photonic Band Gap Materials," *Phys. Rev. B.,* vol. 52, no. 16, pp. 11744-11751, Oct. 1995.

[23] R. W. Ziolkowski and A. Erentok, "Metamaterial-Based Efficient Electrically Small Antennas," *IEEE Trans. Antennas Propagt.,* vol. 54, no. 7, pp. 2113-2130, July 2006.

[24] D. Sounas, N. Kantartzis, and T. Tsiboukis, "Focusing Efficiency Analysis and Optimization Performance of Arbitrarily Sized DNG Metamaterial Slabs with Losses," *IEEE Trans. Microw. Theory Tech.,* vol. 54, no. 12, pp. 4111-4121, Dec. 2006.

[25] A. Alù, F. Bilotti, N. Engheta, and L. Vegni, "Subwavelength, Compact, Resonant Patch Antennas Loaded with Metamaterials," *IEEE Trans. Antennas Propagt.,* vol. 55, no. 1, pp. 13-25, Jan. 2007.

[26] D. Sounas and N. Kantartzis, "Systematic Surface Waves Analysis at the Interfaces of Composite DNG/SNG Media," *Optics Express,* vol. 17, no. 10, pp. 8513-8524, 2009.

[27] D. Smith, S. Schultz, P. Markoš, and C. Soukoulis, "Determination of Effective Permittivity and Permeability of Metamaterials from Reflection and Transmission Coefficients," *Phys. Rev. B*, vol. 65, pp. 1951041-1951045, 2002.

[28] Y. Horii, C. Caloz, and T. Itoh, "Super-Compact Multilayered Left-Handed Transmission Line and Diplexer Application," *IEEE Trans. Microw. Theory Tech.,* vol. 53, pp. 1527-1534, 2005.

[29] T. Weiland, R. Schuhmann, R. Greegor et al., "Ab Initio Numerical Simulation of Left-Handed Metamaterials: Comparison of Calculations and Experiments," *J.Appl. Phys.*, vol. 90, pp. 5419-5424, Nov. 2001.

[30] B. Wu, W. Wang, J. Pacheco, X. Chen, T. Grzegorczyk, and J. A. Kong, "A Study of Using Metamaterials as Antenna Substrate to Enhance Gain," *PIER,* vol. 51, pp. 295-328, 2005.

[31] G. V. Eleftheriades and K. G. Balmain, *Negative Refraction Metamaterials Fundamental Principles and Applications*, New York, Wiley, 2005.

[32] J. B. Pendry, A. J. Holen, D. J. Robbins, and W. J. Stewart, "Magnetism from Conductors and Enhanced Nonlinear Phenomena," *IEEE Trans. Microwave Theory Tech.,* vol. 47, no. 11, pp. 2075-2084, Nov. 1999.

[33] J. Moustafa, N. J. McEwan, R. A. Abd-Alhameed, and P. S. Excell, "Low SAR Phased Antenna Array for Mobile Handsets," *Applied Computational Electromagnetic Society* (*ACES) Journal,* vol. 21, no. 3, pp. 196-205, 2006.

[34] R. W. Ziolkowski and E. Heyman, "Wave Propagation in Media Having Negative Permittivity and Permeability," *Phys. Rev. E.*, vol. 64, pp. 1-15, Oct. 2001.

[35] L. C. Fung, S. W. Leung, and K. H. Chan, "Experimental Study of SAR Reduction on Commercial Products and Shielding Materials in Mobile Phone Applications," *Microwave and Optical Technology Letters,* vol. 36, no. 6, pp. 419-422, Mar. 2003.

[36] G. F. Pedersen and J. B. Andersen, "Integrated Antennas for Hand-Held Telephones with Low Absorption," *Proc. 44th IEEE Veh. Tech. Conf.*, Stockholm, Sweden, pp. 1537-1541, Jun. 1994.

[37] R. Y.-S. Tay, Q. Balzano, and N. Kuster, "Dipole Configuration with Strongly Improved Radiation Efficiency for Hand-Held Transceivers," *IEEE Trans. Antennas Propagt.*, vol. 46, no. 6, pp. 798-806, Jun. 1998.

[38] M. Wnuk, W. Kolosowski, and M. Amamowicz, "Microstrip Antennas on Multilayer Dielectric for Mobile System Communication," *Proc. 14th Int. Wroclaw Symp. on Electromagnet. Compat.*, Poland, pp. 346-350, June 1998.

[39] K. H. Chan, K. M. Chow, L. C. Fung, and S. W. Leung, "Effects of Using Conductive Materials for SAR Reduction in Mobile Phones," *Microwave and Optical Technology Letters,* vol. 44, no. 2, pp. 140-144, Jan. 2005.

[40] Recommended Practice for Determining the Peak Spatial-Average Specific Absorption Rate (SAR) in the Human Head from Wireless Communications Devices - Measurement Techniques, *IEEE Standard-1528*, Dec. 2003.

[41] Ansoft HFSS v. 10, v. 11, www.ansoft.com

[42] T. Oitoh, *Electromagnetic Metamaterials Transmission Line Theory and Microwave Applications*, John Willy & Sons Inc., 2006.

Mohsen Fallah was born in Kashan in 1968. He received the B.S. degree in Electrical Engineering from Isfahan University of Technology, Isfahan, Iran, in 1991, and the M.Sc. degree in Electrical Engineering from Iran University of Science and Technology, Tehran, Iran in 1997, and the Ph.D. degree in Electrical Engineering from Iran University of Science and Technology, Tehran, Iran in 2010. He is a member of the academic staff, Faculty of Electrical Engineering, MUT University, Tehran, Iran. His current research interests include microstrip antennas, passive and active microwave devices, metamaterials and EBG structures, and electromagnetic theory.

Amir Abbas Heidari was born in Kashan in 1985. He received the B.S. degree in Electrical Engineering from KNT University of Technology, Tehran, Iran, in 2007 and the M.S. degree in Electrical Engineering from Shahed University, Tehran, in 2010.

Alireza Mallahzadeh was born in Bushehr in 1977. He received the B.S. degree in Electrical Engineering from Isfahan University of Technology, Isfahan, Iran, in 1999 and the M.Sc. degree in Electrical Engineering from Iran University of Science and Technology, Tehran, Iran in 2001, and the Ph.D. degree in Electrical Engineering from Iran University of Science and Technology, Tehran, in 2006. He is a member of the academic staff, Faculty of Engineering, Shahed University, Tehran. He has participated in many projects relative to antenna design, which resulted in fabricating different types of antennas for various companies. Also, he is interested in numerical modeling, and microwaves.

Farokh Hojjat Kashani received his Ph.D. in Electrical Engineering specializing in Electromagnetic from the University of California at Los Angeles in 1970. From 1970 to 1971, he was an Assistant Prof. at Higher Institute of Telecommunication and the University of Tehran. From 1971 to 1976, he was an Assistant Prof. and chairman of the E. E. Dept. at IUST and from 1976 to 1977, he spent sabbatical leave in Hughes Aircraft Company, aerospace division at Canoga Park, California, US. From June 1987 to June 1988, he took one year sabbatical leave in Communication Department, New South Wales University, Sydney, Australia. He is currently a Professor of Electrical Engineering Department, Iran University of Science and Technology. In April 2002, he was selected as an outstanding professor in Iran. He has published over forty papers and ten books in Persian.

Nonstandard Finite Difference Time Domain Algorithm for Berenger's Perfectly Matched Layer

Naoki Okada and James B. Cole

Graduate School of Systems and Information Engineering
University of Tsukuba, 1-1-1 Tennodai, Tsukuba, Ibaraki 305-8573, Japan
okada@cavelab.cs.tsukuba.ac.jp, cole@cs.tsukuba.ac.jp

***Abstract*—**The nonstandard (NS) finite difference time domain (FDTD) algorithm provides remarkably high accuracy on a coarse grid by optimizing to monochromatic wave propagation within each uniform region. But, an effective absorbing boundary condition (ABC) is also necessary to accurately calculate electromagnetic fields. Although Berenger's perfectly matched layer (PML) is a highly effective ABC, there is still no NS-formulation of it. In this paper, we develop a NS-version of the PML (NS-PML). We compare the NS-PML with other ABCs and demonstrate its excellent absorption.

***Index Terms*—**Nonstandard finite difference time domain (NS-FDTD) algorithm, nonstandard perfectly matched layer (NS-PML), stability.

I. INTRODUCTION

The nonstandard (NS) finite difference time domain (FDTD) algorithm provides high accuracy on a coarse grid by optimizing to monochromatic wave propagation [1, 2, 3]. Even for subwavelength structures the NS-FDTD algorithm has performed successfully [4], but an effective absorbing boundary condition (ABC) is also necessary to accurately calculate electromagnetic fields. The improved second-order Mur ABC and higher-order ABCs shows good absorption [5, 6], but reflection at corners of the numerical grid is high and it is sometimes unstable. Although Berenger's perfectly matched layer (PML) [7] is a highly effective ABC, there is no NS-formulation of it.

We develop a NS-FDTD algorithm for the conductive Maxwell's equations in Section II, a NS-version of the PML (NS-PML) in Section III, and its stability in Section IV. We compare the NS-PML with other ABCs and demonstrate its excellent absorption in Section V.

II. NONSTANDARD FDTD ALGORITHM FOR THE CONDUCTIVE MAXWELL'S EQUATIONS

In dispersion-less and linear-isotropic media, the conductive Maxwell's equations are given by

$$(\mu\partial_t + \sigma^*)\,\mathbf{H} = -\nabla\times\mathbf{E}, \tag{1a}$$
$$(\varepsilon\partial_t + \sigma)\,\mathbf{E} = \nabla\times\mathbf{H}, \tag{1b}$$

where $\partial_t = \partial/\partial t$, $\mathbf{H}$ is the magnetic field, $\mathbf{E}$ is the electric field, μ is the permeability, ε is the permittivity, σ is the electric conductivity, and σ^* is the magnetic conductivity. Applying $\nabla\times$ to both sides of (1) and using the vector identity,

$$\nabla\times\nabla\times\mathbf{V} = \nabla\left(\nabla\cdot\mathbf{V}\right) - \nabla^2\mathbf{V}, \quad (\mathbf{V} = \mathbf{H}, \mathbf{E}), \tag{2}$$

we obtain an absorbing wave equation in a medium with zero charge density,

$$\left(\partial_t^2 - v^2\nabla^2 + 2\left(a + a^*\right)\partial_t + 4aa^*\right)\psi = 0, \tag{3}$$

where $v = 1/\sqrt{\mu\varepsilon}$, $a = \sigma/\left(2\varepsilon\right)$, and $a^* = \sigma^*/\left(2\mu\right)$. The forward and backward solutions are

$$\psi_0 = e^{-(a+a^*)t}e^{i(\mathbf{k}\cdot\mathbf{r}\pm\bar{\omega}t)}, \tag{4}$$

where $\mathbf{r} = (x, y, z)$, $\mathbf{k}$ is the wave vector, and

$$\bar{\omega} = \sqrt{\omega^2 - \left(a - a^*\right)^2}, \tag{5}$$

where ω is the angular frequency.

Using the conventional finite difference time domain (FDTD) algorithm for $t = n\Delta t$, $x, y, z = mh$ ($n, m =$ integer), (3) is discretized as follows,

$$\left(d_t^2 - \frac{v^2\Delta t^2}{h^2}\mathbf{d}^2 + (\alpha + \alpha^*)\,\bar{d}_t + 4\alpha\alpha^*\right)\psi = 0, \tag{6}$$

where $\alpha = a\Delta t$, $\alpha^* = a^*\Delta t$, $d_t f(t) = f(t + \Delta t/2) - f(t - \Delta t/2)$, $\bar{d}_t f(t) = f(t + \Delta t) - f(t - \Delta t)$, and $\mathbf{d} = (d_x, d_y, d_z)$ (d_x, d_y, d_z are defined analogously to d_t). Inserting the solution (4) into (6), we find

$$\left(d_t^2 - \frac{v^2\Delta t^2}{h^2}\mathbf{d}^2 + (\alpha + \alpha^*)\,\bar{d}_t + 4\alpha\alpha^*\right)\psi_0 \neq 0. \tag{7}$$

The right side of (7) does not vanish, because ψ_0 is not a solution of the difference equation (6).

We now seek a nonstandard (NS) finite difference (FD) model of (3) which has the same solution as (3). Replacing $\mathbf{d}^2$ with $\mathbf{d}_0^2$ and h with $s(k, h)$, we find a high accuracy spatial FD expression (see Appendix A),

$$\nabla^2\psi_0 \cong \frac{\mathbf{d}_0^2\psi_0}{s(k, h)^2}, \quad s(k, h) = \frac{2}{k}\sin\left(\frac{kh}{2}\right), \tag{8}$$

and require that

$$\left(d_t^2 - u^2\mathbf{d}_0^2 + (\beta + \beta^*)\,\bar{d}_t + 4\beta\beta^*\right)\psi_0 = 0. \tag{9}$$

This is an example of a NS-FDTD algorithm. Let us find u, β, β^* for which (9) is exactly satisfied. The temporal-spatial FD expressions give

$$\begin{aligned} d_t^2\psi_0 &= 4\sinh^2\left(\frac{\alpha + \alpha^* \pm i\bar{\omega}\Delta t}{2}\right)\psi_0, && (10)\\ \bar{d}_t\psi_0 &= -2\sinh\left(\alpha + \alpha^* \pm i\bar{\omega}\Delta t\right)\psi_0, && (11)\\ \mathbf{d}_0^2\psi_0 &= -4\sin^2\left(kh/2\right)\psi_0. && (12) \end{aligned}$$

Substituting (10)-(12) into (9) and requiring that the imaginary part vanishes, we find

$$\begin{aligned} \beta &= \frac{\tanh\alpha}{1 + \tanh\alpha\tanh\alpha^*}, && (13)\\ \beta^* &= \frac{\tanh\alpha^*}{1 + \tanh\alpha\tanh\alpha^*}. && (14) \end{aligned}$$

Setting the real part to zero, we obtain

$$\begin{aligned} u^2 &= \frac{\sinh^2\left[(\alpha + \alpha^*)/2\right] + \sin^2\left(\bar{\omega}/2\right)}{\cosh\left(\alpha + \alpha^*\right)\sin^2\left(kh/2\right)} \\ &- \frac{\beta\beta^*}{\sin^2\left(kh/2\right)}. && (15) \end{aligned}$$

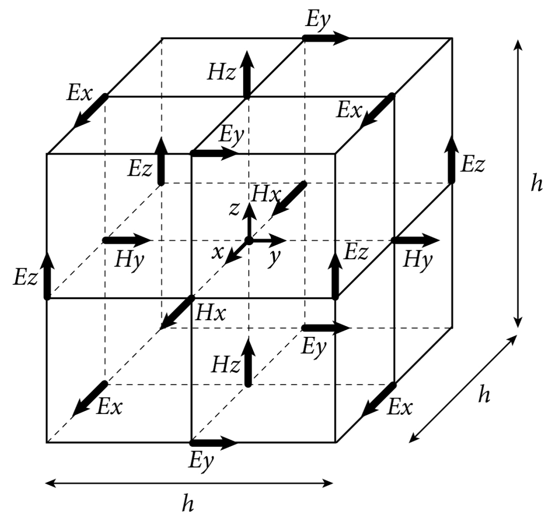

Fig. 1. Yee cell. h is the grid spacing. E_x, E_y, E_z are electric field components. H_x, H_y, H_z are magnetic field components. Components are staggered on the numerical grid.

From the NS-FDTD algorithm for the absorbing wave equation, we obtain the NS-FDTD algorithm for the conductive Maxwell's equations. According to [2], the NS-FDTD algorithm for the non-conductive Maxwell's equations is given by

$$\begin{aligned} d_t\mathbf{H} &= -\frac{u_0}{Z}\mathbf{d} \times \mathbf{E}, && (16a)\\ d_t\mathbf{E} &= u_0 Z\mathbf{d}_0 \times \mathbf{H}, && (16b) \end{aligned}$$

where $u_0 = \sin(\omega\Delta t/2)/\sin(kh/2)$, $Z = \sqrt{\mu/\varepsilon}$, and $\mathbf{d}_0 = \left(d_x^0, d_y^0, d_z^0\right)$ satisfies $\mathbf{d}\cdot\mathbf{d}_0 = \mathbf{d}_0\cdot\mathbf{d} = \mathbf{d}_0^2$ (see Appendix A). Following (16), we define

$$\begin{aligned} \left(d_t + 2\beta^*\right)\mathbf{H} &= -\frac{u}{Z}\mathbf{d} \times \mathbf{E}, && (17a)\\ \left(d_t + 2\beta\right)\mathbf{E} &= uZ\mathbf{d}_0 \times \mathbf{H}. && (17b) \end{aligned}$$

Using the discretized vector identity to which Gauss' law is applied,

$$\mathbf{d}_0 \times \mathbf{d} \times \mathbf{V} = -\left(\mathbf{d}_0 \cdot \mathbf{d}\right)\mathbf{V} = \mathbf{d}_0^2\mathbf{V}, \tag{18}$$

(17a) and (17b) can be transformed into (9). Thus, (17) is a NS-FDTD algorithm for the conductive Maxwell's equations optimized to monochromatic waves. As shown in Fig. 1, the electromagnetic field components are laid out on the grid,

$$\begin{cases} H_x(x + h/2, y, z, t - \Delta t/2), & (19a)\\ H_y(x, y + h/2, z, t - \Delta t/2), & (19b)\\ H_z(x, y, z + h/2, t - \Delta t/2), & (19c) \end{cases}$$

$$\begin{cases} E_x(x, y+h/2, z+h/2, t), & \text{(20a)} \\ E_y(x+h/2, y, z+h/2, t), & \text{(20b)} \\ E_z(x+h/2, y+h/2, z, t). & \text{(20c)} \end{cases}$$

Expanding the temporal finite difference operators, the NS-FDTD algorithm becomes

$$\mathbf{H}^{n+1/2} = \frac{\beta_-^*}{\beta_+^*}\mathbf{H}^{n-1/2} - \frac{u}{\beta_+^* Z}\mathbf{d}\times\mathbf{E}^n, \quad \text{(21a)}$$

$$\mathbf{E}^{n+1} = \frac{\beta_-}{\beta_+}\mathbf{E}^{n-1} + \frac{uZ}{\beta_+}\mathbf{d}_0\times\mathbf{H}^{n+1/2}, \quad \text{(21b)}$$

where $\beta_\pm = 1\pm\beta$, $\beta_\pm^* = 1\pm\beta^*$, and we simply write $\mathbf{H}(\mathbf{r},t)\to\mathbf{H}^n$ (analogously for $\mathbf{E}$).

III. NONSTANDARD PERFECTLY MATCHED LAYER

We derive a nonstandard (NS) perfectly matched layer (PML) formulation based on Berenger's PML. According to the Berenger's PML, the conductive Maxwell's equations in the transverse magnetic (TM) mode ($\mathbf{E}$ parallel to media interfaces) are split by

$$\begin{aligned} \left(\mu\partial_t+\sigma_y^*\right)H_x &= -\partial_y E_z, & \text{(22a)}\\ \left(\mu\partial_t+\sigma_x^*\right)H_y &= \partial_x E_z, & \text{(22b)}\\ \left(\varepsilon\partial_t+\sigma_x\right)E_{zx} &= \partial_x H_y, & \text{(22c)}\\ \left(\varepsilon\partial_t+\sigma_y\right)E_{zy} &= -\partial_y H_x, & \text{(22d)} \end{aligned}$$

where $E_z = E_{zx}+E_{zy}$. The split Maxwell's equations are not equivalent to the absorbing wave equation in the PML, because Gauss' law is invalid for $\sigma_x \neq \sigma_y$. However, we found that the NS-FDTD algorithm based on the absorbing wave equation provides highly effective absorption even in the PML, as shown in Section V. Just as σ is separated into σ_x, σ_y in the PML, we separate $\beta(\sigma)$ into $\beta_x=\beta(\sigma_x)$, $\beta_y=\beta(\sigma_y)$ and $\beta^*(\sigma)$ into $\beta_x^*=\beta^*(\sigma_x)$, $\beta_y^*=\beta^*(\sigma_y)$ in (17). Thus, the NS-FDTD algorithm becomes

$$\begin{aligned} \left(d_t+2\beta_y^*\right)H_x &= -\frac{u}{Z}d_y E_z, & \text{(23a)}\\ \left(d_t+2\beta_x^*\right)H_y &= \frac{u}{Z}d_x E_z, & \text{(23b)}\\ \left(d_t+2\beta_x\right)E_{zx} &= uZd_x^0 H_y, & \text{(23c)}\\ \left(d_t+2\beta_y\right)E_{zy} &= -uZd_y^0 H_x, & \text{(23d)} \end{aligned}$$

where $u=u_0$ only inside the PML to promote the numerical stability as we discuss in Section IV. Expanding the temporal finite difference operators in the Yee cell, we obtain

$$\begin{aligned} H_x^{n+1/2} &= \frac{\beta_{y-}^*}{\beta_{y+}^*}H_x^{n-1/2} - \frac{u}{\beta_{y+}^* Z}d_y E_z^n, & \text{(24a)}\\ H_y^{n+1/2} &= \frac{\beta_{x-}^*}{\beta_{x+}^*}H_y^{n-1/2} + \frac{u}{\beta_{x+}^* Z}d_x E_z^n, & \text{(24b)}\\ E_{zx}^{n+1} &= \frac{\beta_{x-}}{\beta_{x+}}E_{zx}^{n-1} + \frac{uZ}{\beta_{x+}}d_x^0 H_y^{n+1/2}, & \text{(24c)}\\ E_{zy}^{n+1} &= \frac{\beta_{y-}}{\beta_{y+}}E_{zy}^{n-1} - \frac{uZ}{\beta_{y+}}d_y^0 H_x^{n+1/2}, & \text{(24d)} \end{aligned}$$

where $\beta_{i\pm}=1\pm\beta_i$, $\beta_{i\pm}^*=1\pm\beta_i^*$ $(i=x,y)$. In the transverse electric (TE) mode ($\mathbf{E}$ perpendicular to media interfaces), the conductive Maxwell's equations are split by

$$\begin{aligned} \left(\mu\partial_t+\sigma_x^*\right)H_{zx} &= -\partial_x E_y, & \text{(25a)}\\ \left(\mu\partial_t+\sigma_y^*\right)H_{zy} &= \partial_y E_x, & \text{(25b)}\\ \left(\varepsilon\partial_t+\sigma_y\right)E_x &= \partial_y H_z, & \text{(25c)}\\ \left(\varepsilon\partial_t+\sigma_x\right)E_y &= -\partial_x H_z, & \text{(25d)} \end{aligned}$$

where $H_z = H_{zx}+H_{zy}$. We separate β into β_x, β_y (analogously for β^*) and obtain

$$\begin{aligned} H_{zx}^{n+1/2} &= \frac{\beta_{x-}^*}{\beta_{x+}^*}H_{zx}^{n-1/2} - \frac{u}{\beta_{x+}^* Z}d_x E_z^n, & \text{(26a)}\\ H_{zy}^{n+1/2} &= \frac{\beta_{y-}^*}{\beta_{y+}^*}H_{zy}^{n-1/2} + \frac{u}{\beta_{y+}^* Z}d_y E_z^n, & \text{(26b)}\\ E_x^{n+1} &= \frac{\beta_{y-}}{\beta_{y+}}E_x^{n-1} + \frac{uZ}{\beta_{y+}}d_y^0 H_y^{n+1/2}, & \text{(26c)}\\ E_y^{n+1} &= \frac{\beta_{x-}}{\beta_{x+}}E_y^{n-1} - \frac{uZ}{\beta_{x+}}d_x^0 H_x^{n+1/2}, & \text{(26d)} \end{aligned}$$

where $u=u_0$ in the PML. In three dimensions, the NS-PML formulation is similarly derived using the separations based on Berenger's PML.

In two-dimensional PMLs, there is no reflection if the conductivities are continuous and the impedance matching condition is satisfied,

$$\sigma_x^*/\mu = \sigma_x/\varepsilon, \quad \sigma_y^*/\mu = \sigma_y/\varepsilon. \quad \text{(27)}$$

But there is a small reflection due to the discretization on a grid [8], the following definition gives a simple control of the absorption performance [9],

$$\sigma_x = \begin{cases} \sigma_m\left(1-\frac{i}{L}\right)^M, & \text{for } i<L \quad \text{(28a)}\\ \sigma_m\left(1-\frac{N-i}{L}\right)^M, & \text{for } i>N-L, \quad \text{(28b)} \end{cases}$$

$$\sigma_y = \begin{cases} \sigma_m\left(1-\frac{j}{L}\right)^M, & \text{for } j<L \quad \text{(29a)}\\ \sigma_m\left(1-\frac{N-j}{L}\right)^M, & \text{for } j>N-L, \quad \text{(29b)} \end{cases}$$

where $x = ih$, $y = jh$ $(i, j = 0, 1, \cdots, N)$, L is the number of PML layers, M is the damping constant, and σ_m is given by using the incidence angle θ and theoretical reflection coefficient R_{th},

$$\sigma_m = -\frac{(M+1)\varepsilon v}{2Lh\cos\theta}\ln R_{th}. \tag{30}$$

We empirically choose $\theta = 60°$, $R_{th} = 10^{-8}$, and $M = 2$.

IV. NUMERICAL STABILITY

The numerical stability of the NS-FDTD algorithm for the conductive Maxwell's equations is the same as the absorbing wave equation, because they are equivalent in homogeneous media as shown in Section II. Thus, we derive the stability for latter. For a monochromatic wave, we obtain

$$\mathbf{d}_0^2\psi_0 = -D^2\psi_0, \tag{31}$$

where D^2 is given later. Using (31), the NS-FDTD algorithm (9) is rewritten in the form,

$$\begin{pmatrix} \psi_0^n \\ \psi_0^{n+1} \end{pmatrix} = A^n \begin{pmatrix} \psi_0^0 \\ \psi_0^1 \end{pmatrix}, \tag{32}$$

where we simply write $\psi_0(\mathbf{r}, n\Delta t) \to \psi_0^n$, and

$$A = \begin{pmatrix} 0 & 1 \\ -\frac{1-\beta-\beta^*}{1+\beta+\beta^*} & \frac{2-4\beta\beta^*-u^2D^2}{1+\beta+\beta^*} \end{pmatrix}. \tag{33}$$

Since the eigenvalue of A gives the algorithm stability (see Appendix B), we find

$$u^2 \le \frac{2-4\beta\beta^* + 2\sqrt{1-(\beta+\beta^*)^2}}{D^2}. \tag{34}$$

The strictest condition on u^2 is found by taking the maximum possible value of D^2 in (34). Solving $\partial_{k_p} D^2 = 0$ $(p = x, y, z)$ in each dimension, we obtain

$$\max\left(D^2\right) = \begin{cases} 4, & \text{for 1-D} \quad (35a) \\ \dfrac{1}{\gamma_1}, & \text{for 2-D} \quad (35b) \\ \dfrac{\gamma_1}{\gamma_2}\left(3 - \dfrac{2\gamma_1^2}{\gamma_2}\right), & \text{for 3-D,} \quad (35c) \end{cases}$$

where γ_1 and γ_2 are defined in Appendix A. Although the stability is almost-completely satisfied in the PML because electromagnetic waves are exponentially damped, non-physical separated conductivities sometimes cause instability [10, 11]. Thus, we replace conductivity-dependent u with conductivity-independent u_0 in the PML.

Table 1: Example simulation parameters

medium	vacuum
wavelength	500 nm
grid spacing	50 nm
beam width	15μm
computational domain	120μm $\times$ 60μm

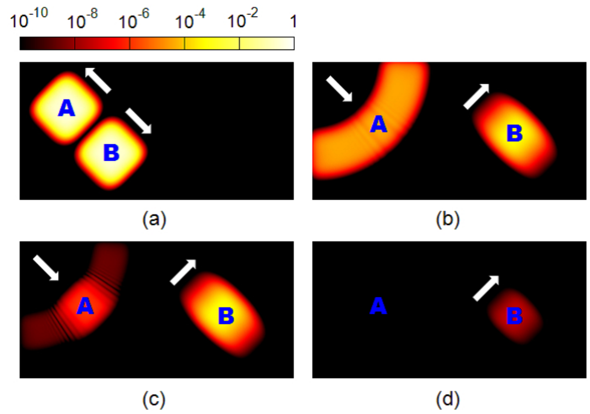

Fig. 2. Comparison of nonstandard (NS) absorbing boundary conditions (ABCs). White arrows show propagation directions of pulses. (a) Incident pulses: A is incident on a corner of the computational domain, while B is incident on a side. Reflections of pulses A and B with (b) NS-Mur ABC, (c) NS-Higdon ABC, and (d) $L = 8$ layer NS-PML.

V. PERFORMANCE VALIDATION

We compare the NS-PML with the nonstandard Mur (NS-Mur) [5] and Higdon (NS-Higdon) absorbing boundary conditions (ABCs). Similarly to the NS-Mur ABC, the NS-Higdon ABC is simply derived from the conventional Higdon ABC [12] by replacing $v\Delta t/h$ with u_0.

Using the example parameters listed in Table 1, we simulate absorptions at an optical wavelength on a coarse grid in the TM mode. Figure 2 shows intensity distributions of reflections using the NS-Mur, NS-Higdon, and NS-PML of $L = 8$ layers. Figure 2(a) shows incident pulses impinge upon the boundary at an angle of $\theta = 45°$ from the normal (A is incident on a corner of the computational domain, B is incident on a side). In Fig. 2(b),

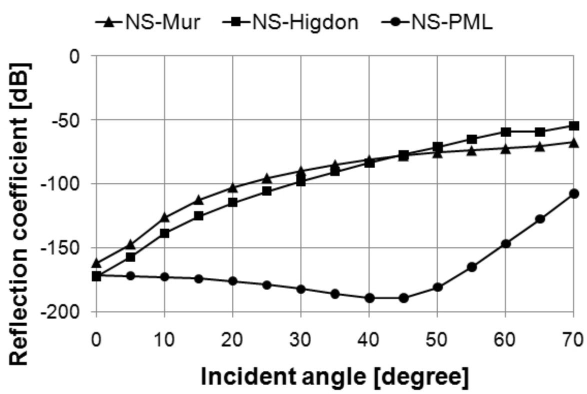

Fig. 3. Angular reflection spectrum of NS-PML ($L = 8$ layers) compared with NS-Mur and NS-Higdon.

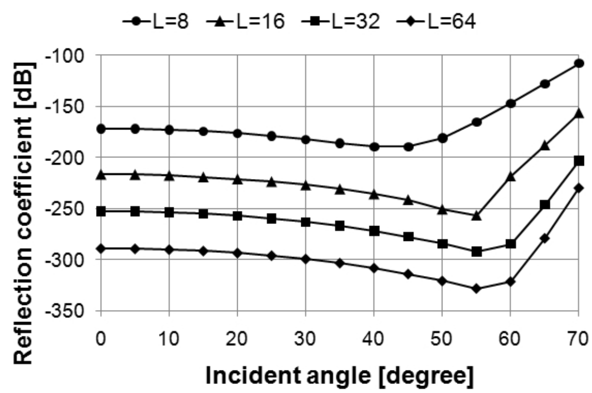

Fig. 4. Angular reflection spectrum of NS-PML with different numbers of layers, $L = 8$, 16, 32, and 64.

the NS-Mur generates large reflections for pulse A (about -80 dB) because corner values are approximated. In Fig. 2(c), the NS-Higdon improves the corner absorption, but it also has about the same reflection as the NS-Mur for pulse B. Whereas, in Fig. 2(d), the NS-PML of 8 layers greatly reduces the reflections for both pulses (about -190 dB).

Using the parameters of Table 1, we calculate the reflection coefficient, which is defined by the ratio of pulse B intensities before and after reflection on a side. In Fig. 3, we show the angular reflection spectra using the NS-Mur, NS-Higdon, and NS-PML of $L = 8$ layers. For both the NS-Mur and NS-Higdon, the reflection rapidly increases with incidence angle, whereas the NS-PML provides high absorption at large angles. In Fig. 4, we show the angular reflection spectra of NS-PML with different numbers of layers, $L = 8$, 16, 32, 64. The more layers, the higher the absorption (doubling L reduces reflection by about 30 dB). When $\theta > 60°$, the reflection exponentially increases.

VI. Conclusion

We developed a nonstandard (NS) finite difference time domain (NS-FDTD) algorithm for the conductive Maxwell's equations and a NS-version of the perfectly matched layer (NS-PML). Heretofore, the NS-FDTD algorithm has performed successfully in many nanoscale simulations [3, 4]. However, it is sometimes unstable after a large number of wave periods (for example, in whispering gallery mode calculations) due to corner reflections, but the NS-PML ensures absolute stability. We showed that the NS-PML provides more effective absorption than conventional NS-Mur and NS-Higdon absorbing boundary conditions.

Comparing the NS-PML with the conventional or standard (S) PML, the absorption performance is the same because it is determined by the given splitted conductivities. But although the memory cost is the same, the NS stability is better than the S one (the NS computational wave velocity can be increased by: 10% in 2-D; 35% in 3-D) [3].

The "unsplit" PML has been proposed [13, 14]. Since the unsplit PML has lower computational cost, in future work we will try to develop a NS-version of the unsplit PML.

Appendix A
Nonstandard Finite Difference Model

A high accuracy spatial finite difference model is found by optimizing to monochromatic wave propagation [2]. In one-dimension, the conventional central finite difference (FD) approximation is defined by

$$\partial_x \psi(x,t) \cong \frac{d_x \psi(x,t)}{h}, \tag{36}$$

where $d_x\psi(x,t) = \psi(x+h/2,t) - \psi(x-h/2,t)$. For monochromatic waves $\psi_0 = e^{i(kx \pm \omega t)}$, we have an exact nonstandard (NS) FD expression,

$$\frac{d_x\psi_0}{s(k,h)} = \partial_x \psi_0, \quad s(k,h) = \frac{2}{k}\sin\left(\frac{kh}{2}\right). \tag{37}$$

The exact NS-FD expression of (37) cannot be generalized beyond one dimension, but it is possible to construct a high accuracy NS-FD expression with respect to plane waves of the form,

$$\nabla^2\psi_0(\mathbf{r},t) \cong \frac{\mathbf{d}_0^2\psi_0(\mathbf{r},t)}{s(k,h)^2}, \tag{38}$$

where

$$\begin{aligned}\mathbf{d}_0^2 = \mathbf{d}^2 &+ \gamma_1\left(d_x^2 d_y^2 + d_y^2 d_z^2 + d_z^2 d_x^2\right)\\ &+ \gamma_2 d_x^2 d_y^2 d_z^2,\end{aligned} \tag{39}$$

where $\mathbf{d} = (d_x, d_y, d_z)$ and

$$\gamma_1 \cong \frac{1}{6} + \frac{k^2h^2}{180} - \frac{k^4h^4}{23040} + \cdots, \tag{40}$$

$$\gamma_2 \cong \frac{1}{30} + \frac{k^2h^2}{360} - \frac{k^4h^4}{7200} + \cdots. \tag{41}$$

Details of this derivation are given in [2, 3]. The error of the NS-FD approximation is

$$\frac{1}{\psi_0}\left(\nabla^2 - \frac{\mathbf{d}_0^2}{s(k,h)^2}\right)\psi_0 \cong \frac{(kh)^6k^2}{20160} + \cdots. \tag{42}$$

Since the error of the conventional FD approximation is

$$\frac{1}{\psi_0}\left(\nabla^2 - \frac{\mathbf{d}^2}{h^2}\right)\psi_0 \cong \frac{(kh)^2k^2}{12} + \cdots, \tag{43}$$

(38) is almost exact.

We need to approximate $\nabla\times$ in Maxwell's equations, but $\mathbf{d}_0 = (d_x^0, d_y^0, d_z^0)$ which satisfies $\mathbf{d}_0^2 = \mathbf{d}_0 \cdot \mathbf{d}_0$ does not exist. Instead, we require that

$$\mathbf{d}_0^2 = \mathbf{d}_0 \cdot \mathbf{d} = \mathbf{d} \cdot \mathbf{d}_0, \tag{44}$$

and find that

$$\mathbf{d}_0 = \begin{bmatrix} d_x\left(1 + \frac{\gamma_1}{2}\left(d_y^2 + d_z^2\right) + \frac{\gamma_2}{3} d_y^2 d_z^2\right)\\ d_y\left(1 + \frac{\gamma_1}{2}\left(d_x^2 + d_z^2\right) + \frac{\gamma_2}{3} d_x^2 d_z^2\right)\\ d_z\left(1 + \frac{\gamma_1}{2}\left(d_x^2 + d_y^2\right) + \frac{\gamma_2}{3} d_x^2 d_y^2\right)\end{bmatrix}. \tag{45}$$

APPENDIX B
EIGENVALUE AND STABILITY

An algorithm is given by

$$\mathbf{\Psi}^n = A^n\mathbf{\Psi}^0, \tag{46}$$

where $t = n\Delta t$ ($n =$ integer), $\mathbf{\Psi}(\mathbf{r},t) \to \mathbf{\Psi}^n$, and

$$A = \begin{pmatrix} 0 & 1\\ -c_1 & 2c_2\end{pmatrix}. \tag{47}$$

If $|A| \neq 0$ such as (33), A is diagonalizable and the algorithm stability is given by $|\lambda| \leq 1$ ($\lambda =$ eigenvalue of A) [15]. λ is found by solving

$$|A - \lambda I| = 0, \tag{48}$$

where I is the identity matrix. We obtain

$$\lambda = c_2 \pm \sqrt{c_2^2 - c_1}. \tag{49}$$

Using $|\lambda| \leq 1$, the algorithm stability becomes

$$c_2^2 \leq c_1 \leq 1. \tag{50}$$

REFERENCES

[1] R. E. Mickens, "Nonstandard Finite Difference Models of Differential Equations," *World Scientific*, 1994.

[2] J. B. Cole, "High-Accuracy Yee Algorithm Based on Nonstandard Finite Differences: New Developments and Verifications," *IEEE Trans. Antennas Propag.*, vol. 50, no. 9, pp. 1185-1191, 2002.

[3] J. B. Cole, S. Banerjee, and M. I. Haftel, "High Accuracy Nonstandard Finite Difference Time-Domain Algorithms for Computational Electromagnetics: Applications to Optics and Photonics," chap. 4, pp. 89-109 in Advances in the Applications of Nonstandard Finite Difference Schemes, R. E. Mickens, ed., *Scientific*, 2005.

[4] N. Okada and J. B. Cole, "Simulation of Whispering Gallery Modes in the Mie Regime using the Nonstandard Finite-Difference Time Domain Algorithm," *J. Opt. Soc. Am. B*, vol. 27, no. 4, pp. 631-639, 2010.

[5] J. B. Cole and D. Zhu, "Improved Version of the Second-Order Mur Absorbing Boundary Condition Based on a Nonstandard Finite Difference Model," *Applied Computational Electromagnetic Society (ACES) Journal*, vol. 24, no. 4, pp. 375-381, 2009.

[6] M. F. Hadi, "Wide-Angle Absorbing Boundary Conditions for Low and High-Order FDTD Algorithms," *Applied Computational Electromagnetic Society (ACES) Journal*, vol. 24, no. 1, pp. 9-15, 2009.

[7] J. P. Berenger, "A Perfectly Matched Layer for the Absorption of Electromagnetic Waves," *J. Comput. Phys.*, vol. 114, no. 2, pp. 185-200, 1994.

[8] W. C. Chew and J. M. Jin, "Perfectly Matched Layers in the Discretized Space: An Analysis

and Optimization," *Electromagnetics*, vol. 16, pp. 325-340, 1996.

[9] Z. Wu and J. Fang, "Numerical Implementation and Performance of Perfectly Matched Layer Boundary Condition for Waveguide Structures," *IEEE Trans. Microwave Theory Tech.*, vol. 43, no. 12, pp. 2676-263, 1995.

[10] S. Abarbanel and D. Gottlieb, "A Mathematical Analysis of the PML Method," *J. Comput. Phys.*, vol. 134, no. 2, pp. 357-363, 1997.

[11] F. L. Teixeira and W. C. Chew, "Finite-Difference Computation of Transient Electromagnetic Waves for Cylindrical Geometries in Complex Media," *IEEE Trans. Geosci. Remote Sens.*, vol. 38, no. 4, pp. 1530-1543, 2000.

[12] R. L. Higdon, "Absorbing Boundary Conditions for Difference Approximations to the Multi-Dimensional Wave Equation," *Mathematics of Computation*, vol. 47, no. 176, pp. 437-459, 1986.

[13] W. C. Chew and W. H. Weedon, "A 3D Perfectly Matched Medium from Modified Maxwell's Equations with Stretched Coordinates," *Microwave Optical Tech. Lett.*, vol. 7, no. 13, pp. 599-604, 1994.

[14] L. Zhao and A. C. Cangellaris, "A General Approach for the Development of Unsplit-Field Time-Domain Implementations of Perfectly Matched Layers for FDTD Grid Truncation," *IEEE Microwave and Guided Wave Letters*, vol. 6, no. 5, pp. 209-211, 1996.

[15] S. Wang and F. L. Teixeira, "Some Remarks on the Stability of Time-Domain Electromagnetic Simulations," *IEEE Trans. Antennas Propag.*, vol. 52, no. 3, pp. 895-898, 2004.

Naoki Okada is a Ph.D. student in the Graduate School of Systems and Information Engineering, University of Tsukuba, Japan. His main research interests are in computational optics, electromagnetic simulations, and algorithm development. In particular, he focuses on the use of high accuracy nonstandard finite difference time domain (FDTD) algorithms for light scattering simulation and optical waveguide device design. He is also interested in parallel computation using the graphics processing unit (GPU), and photorealistic rendering of structural colors such as Morpho butterfly. Please visit his web page at http://nsfdtd.org/.

James B. Cole graduated from the University of Maryland (USA) with a Ph.D. in Particle Physics. During post-doctorate research at the NASA Goddard Space Flight Center, he began his career in numerical simulations (cosmic ray antiproton flux). Later, he worked on stochastic simulations at the Army Research Laboratory, and visited the NTT Basic Research Laboratory (Japan) for one year. As a research physicist at the Naval Research Laboratory, working on the Connection Machine, he developed the earliest nonstandard finite difference (NS-FD) models for acoustic simulations. After joining the faculty of the University of Tsukuba (Japan), where he is a professor, he extended NS-FD models to computational electromagnetics and optics.

Modified Adaptive Cross Approximation Algorithm for Analysis of Electromagnetic Problems

Z. N. Jiang, R. S. Chen, Z. H. Fan, Y. Y. An, M. M. Zhu, and K. W. Leung

Department of Communication Engineering
Nanjing University of Science and Technology, Nanjing, China, 210094
eechenrs@mail.njust.edu.cn

Abstract- In order to efficiently analyze the large dense complex linear system arising from electric field integral equations (EFIE) formulation of electromagnetic scattering problems, the adaptive cross approximation (ACA) is applied to accelerate the matrix-vector multiplication operations. Although the ACA is already efficient compared with the direct method, this paper utilizes a novel technique to further reduce the setup time and storage memory. This method applies the predetermined interaction list supported oct tree (PILOT) to form a new far field interaction list. Using the new far field interaction list, less setup time representation of the far field matrix is obtained. The numerical results of complex objects are used to demonstrate that the memory requirement of the modified ACA is also less than that of the traditional ACA. An efficient preconditioning technique is combined into the inner-outer flexible generalized minimal residual (FGMRES) solver to further speed up the matrix-vector multiplication.

Index Terms- Adaptive cross approximation (ACA), flexible generalized minimal residual (FGMRES), predetermined interaction list supported oct tree (PILOT).

I. INTRODUCTION

Different electromagnetic scattering problems have been studied in recent years. They include, but not limited to, radar cross section (RCS) computations, antenna analysis, remote sensing, biomedicine, electromagnetic interference (EMI), and electromagnetic compatibility (EMC). In this paper, the scattering of the complex objects in free space are analyzed. Simulating these problems is very time demanding, and good numerical methods are required to compute their solutions quickly and efficiently. The method of moments (MoM) [1-6] is one of the most widely used techniques for solving electromagnetic problems. For a large electromagnetic problem, the number of unknowns, N, will be large and it would be difficult to solve the matrix equation. This is because the memory requirement and computational complexity are proportional to $O(N^2)$ and $O(N^3)$, respectively. This difficulty can be circumvented by using the Krylov iterative method, which can reduce the operation count to $O(N^2)$.

To alleviate this problem, many fast solution algorithms have been developed. The most popular fast solution include the multilevel fast multipole algorithm (MLFMA) [7-10], has $O(N\log N)$ complexity for a given accuracy. Though efficient and accurate, this algorithm is highly technical. It utilizes a large number of tools, such as partial wave expansion, exponential expansion, filtering, and interpolation of spherical harmonics. For the MLFMA, however, a *priori* knowledge of the Green’s function is needed for the formulation and implementation. As a result, it cannot be easily applied to analyze the layered media problems. ACA is another popular technique used to analyze the scattering/radiation [11], which exploits the well known fact that for well separated sub-scatterers, the corresponding sub-matrices are low rank and can be compressed. In contrast with MLFMA, the ACA is purely algebraic and, therefore, don’t depend on the problem Green’s function. However, the setup time of the ACA is much more than that of MLFMA. Because of that, the MLFMA reuses multipole and local expansion information across levels, while the ACA does not.

The aim of this paper is to present a modified ACA for solving the electromagnetic problems. It utilizes the predetermined interaction list supported oct tree (PILOT) [12-13] to reduce the setup time and the memory consumption of ACA. An efficient preconditioning technique is combined into the inner-outer flexible generalized minimal residual (FGMRES) solver to speed up the convergence rate of the electric field integral equation (EFIE) [14-17]. Simulation results show that the modified ACA is computationally more efficient than the traditional ACA.

The remainder of this paper is organized as follows. Section II demonstrates the formulation of EFIE. Section III describes the theory and implementation of the modified ACA in more details and gives a brief introduction to the inner-outer flexible generalized minimal residual (FGMRES) method. Numerical experiments are presented to demonstrate the efficiency of this proposed method in Section IV. Conclusions are provided in Section V.

II. Formulation

In this paper, the electric field integral equation (EFIE) is used to analyze electromagnetic scattering problems. The EFIE formulation of electromagnetic wave scattering problems using planar Rao-Wilton-Glisson (RWG) basis functions for surface modeling is presented in [3]. The resulting linear systems from EFIE formulation after Galerkin's testing are briefly outlined as follows

$$\sum_{n=1}^{N} Z_{mn} I_n = V_m, \qquad m = 1, 2, \ldots, N, \tag{1}$$

where

$$\begin{aligned} Z_{mn} = \frac{jk}{4\pi}\Big(&\iint_s \Lambda_m(\mathbf{r}) \cdot \iint_s G(\mathbf{r},\mathbf{r}')\Lambda_n(\mathbf{r}')dS'dS \\ &-\frac{1}{k^2}\iint_s \nabla\cdot\Lambda_m(\mathbf{r}) \cdot \iint_s G(\mathbf{r},\mathbf{r}')\nabla\cdot\Lambda_n(\mathbf{r}')dS'dS\Big), \end{aligned} \tag{2}$$

and

$$V_m = \iint_s \Lambda_m(\mathbf{r}) \cdot \left(\frac{1}{\eta}\mathbf{E}^i(\mathbf{r})\right)dS, \quad G(\mathbf{r},\mathbf{r}') = \frac{e^{-jk|\mathbf{r}-\mathbf{r}'|}}{|\mathbf{r}-\mathbf{r}'|}.$$

Here, $G(\mathbf{r},\mathbf{r}')$ refers to the Green's function in free space and $\{I_n\}$ is the column vector containing the unknown coefficients of the surface current expansion with RWG basis functions. Also, as usual, $\mathbf{r}$ and $\mathbf{r}'$ denote the observation and source point locations. $\boldsymbol{E}^i(\mathbf{r})$ is the incident excitation plane wave, and η and k denote the free space impendence and wave number, respectively. N is the number of unknowns used to discretize the object.

Once the matrix equation (1) is solved, the expansion coefficients $\{I_n\}$ can be used to calculate the scattered field and RCS. In the following, we use Z to denote the coefficient matrix in equation (1), $I = \{I_n\}$ and $V = \{V_n\}$ for simplicity. Then, the EFIE matrix equation (1) can be symbolically rewritten as

$$ZI = V. \tag{3}$$

To solve the above matrix equation by an iterative method, the matrix-vector products are needed at each iteration. Traditionally, a matrix-vector production requires the operation cost $O(N^2)$.

III. Modified ACA

A. The oct tree structure

Take three dimensional problems into account; ACA is based on the data structure of the oct tree [8]. In Fig. 1, the box enclosing the object is subdivided into smaller boxes at multiple levels, in the form of an octal tree. The largest boxes not touching each other are at level 2, while the smallest boxes are at level L. The subdivision process runs recursively until the finest level L.

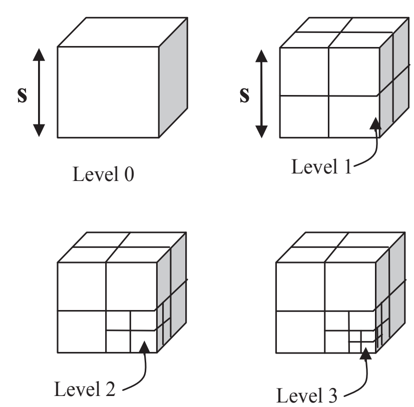

Fig. 1. The sketch of the octree structure.

With reference to Fig. 1, the box has its far interaction box at level 2 or higher. The far interaction boxes can be analyzed using the ACA.

B. Predetermined interaction list supported oct tree (PILOT)

The form of possible far interaction boxes for an observation box in the two dimensional case is shown in the Fig. 2.

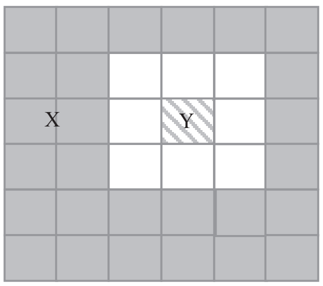

Fig. 2. The form of possible far interaction boxes for an observation box in the two dimensional case.

Where *Y* is the observation box, *X* indicates the far interaction part of *Y*. For each observation box in Fig. 2, there are 27 possible boxes of the far interaction part of the impedance matrix in the two dimensional problems (there are 189 possible boxes in the far interaction part for the three dimensional case). The interaction matrix between the observation box and the box in the far interaction part is filled by ACA [11]. Therefore, the setup time of the traditional ACA is very long. In order to improve the setup time of the traditional ACA, a new far field interaction list called the PILOT algorithm is used in this paper.

According to [13], the PILOT algorithm utilizes the idea that higher compression is achieved when the dimension of the matrix is large. It utilizes that the far field interaction lists of siblings share many common cubes to regroup a new far field interaction list, while further compression is achieved by using the PILOT algorithm. It must be noted that the common interaction list does not directly translate into a merged interaction because the rank of such an interaction submatrix will not in general be low. The common interaction list is decomposed into disjointed parts such that the overall compression is optimized. Each of these disjointed parts is an interaction between grouped source cubes and observer cubes. For simplicity, the two dimensional common interaction list of sibling combination is illustrated in Fig. 3.

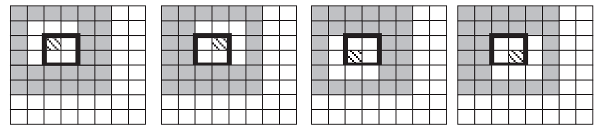

(a)

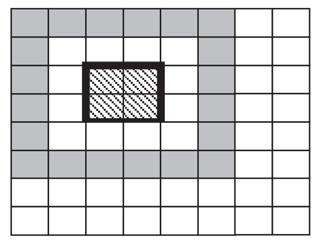

(b)

Fig. 3. (a) Far interaction part of each cube. (b) The common interaction list of sibling combination.

The decomposition of the common interaction list of Fig. 3 (b) into merged interactions is shown in Fig. 4.

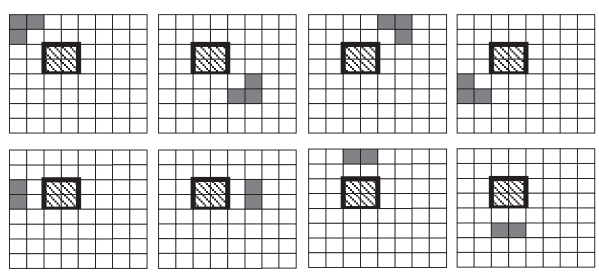

Fig. 4. The decomposition of the common interaction list.

Further compression is possible considering common interaction lists for each pair's siblings. Thus, the regular interaction list is replaced by the new interaction list. The types of the new interaction for the two dimensional case are shown in Fig. 5.

In [11], there are 108 possible far interaction boxes for each sibling of the traditional ACA in the two dimensional case which is shown in Fig. 3 (a) (there are 1512 possible far interaction boxes for three dimensional case). However, there are only 16 entries with four distinct types (4 entries for the type 1, 4 entries for the type 2, 4 entries for the type 3, and 4 entries for the type 4) of the far interaction for each sibling of the modified ACA which are shown in Fig. 5. The types of the new interaction in the three dimensional case are shown in Fig. 6.

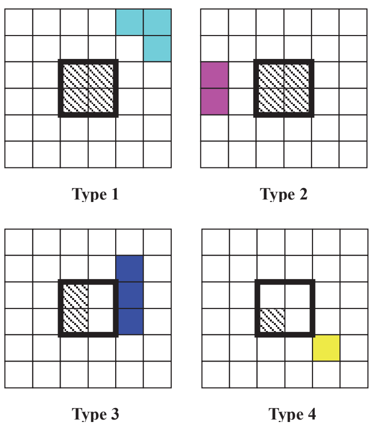

Fig. 5. The types of the interaction in two dimensional case.

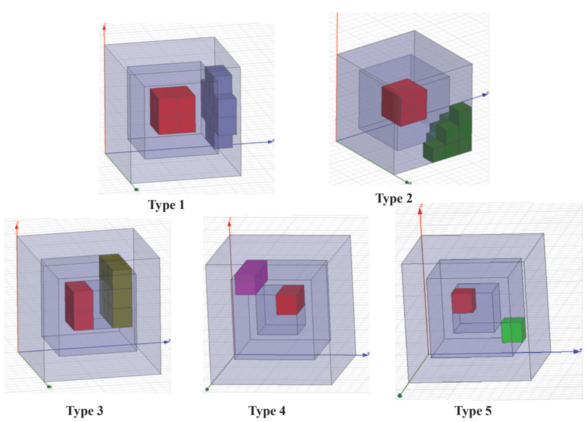

Fig. 6. The types of the interaction in the three dimensional case.

There are 40 entries with five distinct types (6 entries for the type 1 and type 3, 8 entries for the type 2 and type 5, 12 entries for the type 4) of the far interaction for each sibling of the modified ACA. The pattern of the new far field interaction list for a given sibling combination is invariant from that of a different sibling combination at the same level. It is the same for sibling combinations across levels. A higher-level far field interaction list is just a magnified version of that at the lower level.

C. ACA compression of the new interaction list

For the far interaction part of the impedance matrix, its elements are not explicitly computed and stored. Two domains are considered. The first one is an observation domain i that contains m_1 basis functions, whereas the second one is a source domain j that contains m_2 test functions. When the two domains are sufficiently separated, the impedance matrix associated with them can be expressed using low rank representations [18-20]. This feature is utilized in the ACA. In the ACA implementation, the impedance matrix which is gotten through the EFIE of the two sufficiently separated boxes can be expressed in terms of two small matrices [11]

$$[Z_{ij}]_{m_1 m_2} = [U_{ij}]_{m_1 r}[V_{ij}]_{r m_2}, \tag{4}$$

where $[Z_{ij}]_{m_1 m_2}$ is the interaction matrix between the observation and source domains. The index r denotes the rank of the matrix $[Z_{ij}]_{m_1 m_2}$ and is much smaller than m_1 and m_2. Therefore, evaluating the matrix-vector product of the three matrices is much easier than for the direct multiplication.

D. Flexible generalized minimal residual (FGMRES)

In this paper, the FGMRES is used as the iterative solver for the EFIE to further accelerate the convergence [14-17]. Consider the iterative solution of equations of the form $Ax=b$. The GMRES algorithm with the right preconditioning solves the modified system $AM^{-1}(Mx)=b$, where the preconditioner M is constant. However, in FGMRES, the preconditioner is allowed to vary from one step to another in the outer iteration. We have GMRES for the inner iterations whose preconditioner is chosen as the near interaction of the modified ACA.

IV. NUMERICAL RESULTS

In this section, a number of numerical examples are presented to demonstrate the efficiency of the modified ACA in solving linear systems of electromagnetic scattering problems. The truncating tolerance of the ACA is 10^{-3} (relative to the largest singular value). All numerical experiments were performed in single precision on a Core-2 6300 with 1.86 GHz CPU and 1.96GB RAM. The restart number of the generalized minimal residual (GMRES) is set to be 30 and the stop precision for restarted GMRES is denoted to be 10^{-3}. Both the inner and outer restart numbers of FGMRES are 30. The stop precision for the inner and outer iteration in the FGMRES algorithm is 10^{-2} and 10^{-3}, respectively.

A. Cylinder geometry

First, we consider the scattering of a perfectly electrically conducting (PEC) cylinder at 300 MHz. The height and radius of the cylinder geometry are 1 m and 0.5 m, respectively. The z-axis is used as the rotation axis. It consists of the cylinder geometry with 12990 unknowns. The numerical result of monostatic RCS in theta direction when ϕ is fixed at 0° is depicted in Fig. 7. It can be found that there is an excellent agreement between the result of the modified ACA and that of FEKO. The result validates the accuracy of the modified ACA.

B. The plane-cylinder geometry

The bistatic RCS for the plane-cylinder geometry is shown in Fig. 8. The edge length of the square plane is 4 m, the radius of the small column is 0.1 m, and the height of the small column is 2 m. The rotation axis is the *z*-axis. The frequency is 300 MHz. It can be observed that the result of the proposed method agrees very well with the FEKO. Figures 9 and 10 show the setup time and the memory requirement for the plane-cylinder geometry as a function of the number of unknowns. With reference to Fig. 9, the setup time of the modified ACA is much less than that of the traditional ACA. With reference to Fig. 10, the memory requirement of the modified ACA is also much less than that of the traditional ACA.

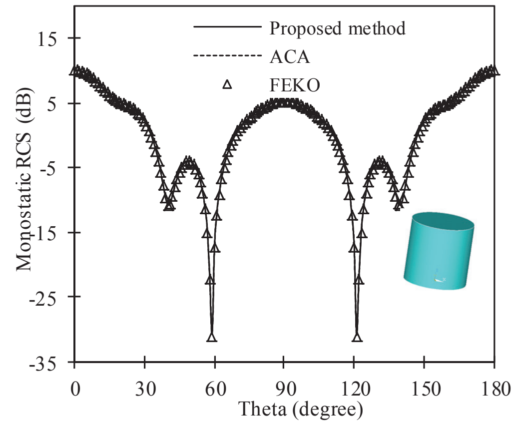

Fig. 7. The monostatic RCS for the cylinder geometry.

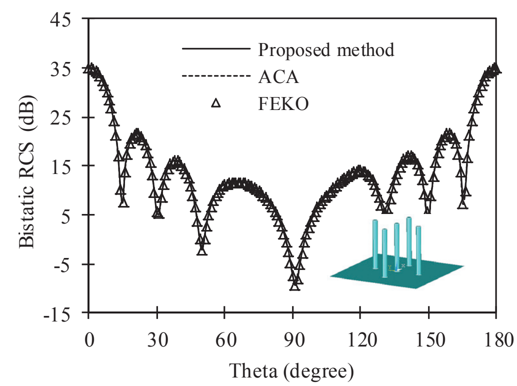

Fig. 8. The bistatic RCS for the plane-cylinder geometry.

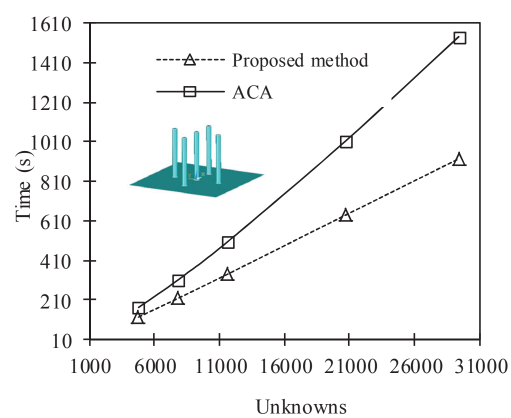

Fig. 9. The setup time for the plane-cylinder geometry.

Figure 11 gives the convergence history curves of the modified ACA solved with GMRES and FGMRES. The geometry is discretized with 29411 unknowns at 300 MHz. In this numerical experiment, GMRES requires 4884 s with 5182 iterative steps, while FGMRES requires only 567 s with 320 outer iterative steps. The solving time of GMRES is 8 times longer than that of FGMRES in this example.

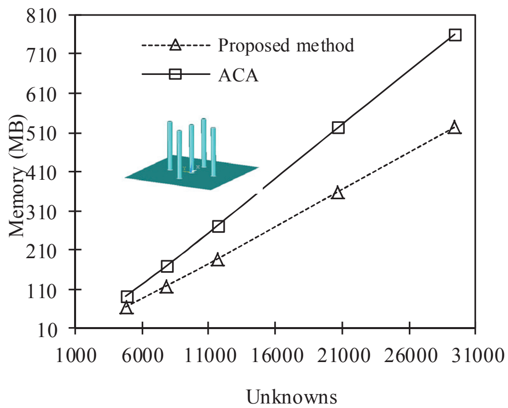

Fig. 10. The memory requirement for the plane-cylinder geometry.

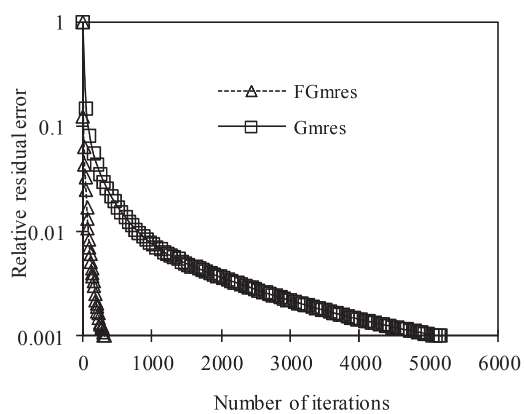

Fig. 11. Convergence histories of the proposed method for the plane-cylinder geometry solved with GMRES and FGMRES.

C. The VIAS geometry

The third example is the VIAS geometry [21]. The geometry fits within a cuboid with an aspect ratio $6:5:0.5$, and the maximum dimension is 4λ at 200 MHz. Figure 12 shows that the result of the proposed method agrees very well with the FEKO. The setup time and the memory requirement for the VIAS geometry as a function of the number of unknowns are shown in Figs. 13 and 14, respectively. With reference to Fig. 13, the setup time of the modified ACA is much less than that of the traditional ACA. It can be observed that the memory requirement of the modified ACA is also much less than that of the traditional ACA according to Fig. 14.

In order to compare the efficiency of the FGMRES with that of GMRES, the plots for the convergence steps and the solve times of the proposed method are provided in Fig. 15 and Fig. 16. It can be found that the solving time of GMRES is 6 times longer than that of FGMRES in this example.

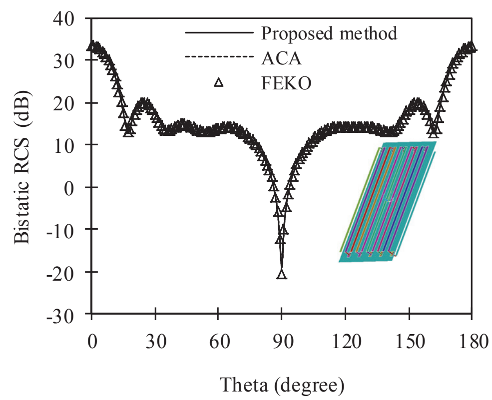

Fig. 12. The bistatic RCS for the VIAS geometry.

V. CONCLUSIONS

In this paper, a modified ACA is proposed for the electromagnetic problems. The proposed method utilizes the PILOT algorithm to reduce the setup time of the ACA, while it does not increase the memory consumption of the ACA. The numerical results demonstrate that setup time of the modified ACA is much less than that of the traditional ACA, while the memory consumption of the modified ACA is also less than that of the

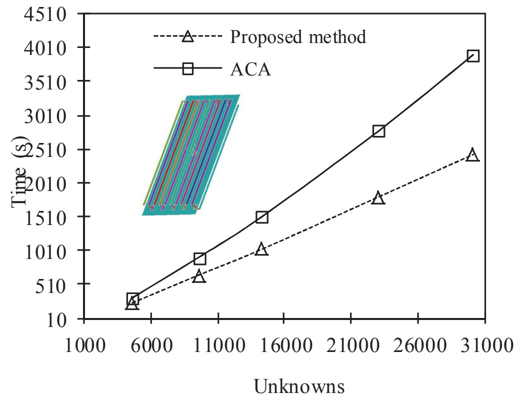

Fig. 13. The setup time for the VIAS geometry.

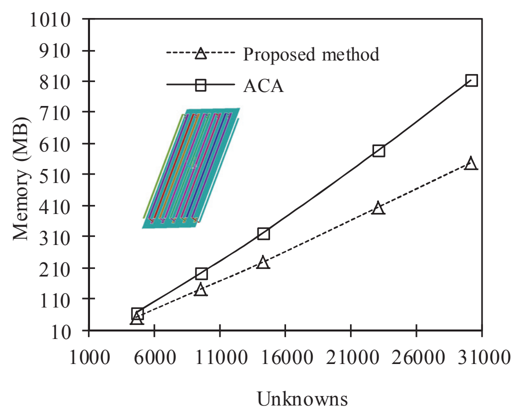

Fig. 14. The memory requirement for the VIAS geometry.

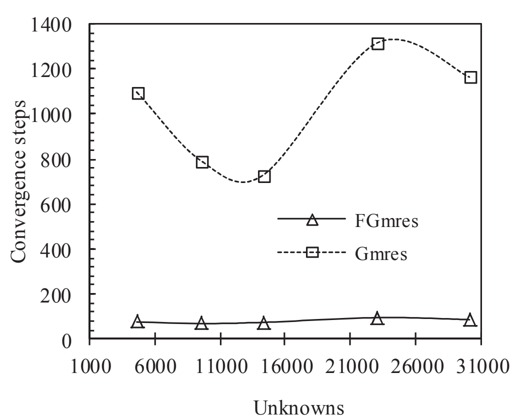

Fig. 15. The convergence steps for the VIAS geometry.

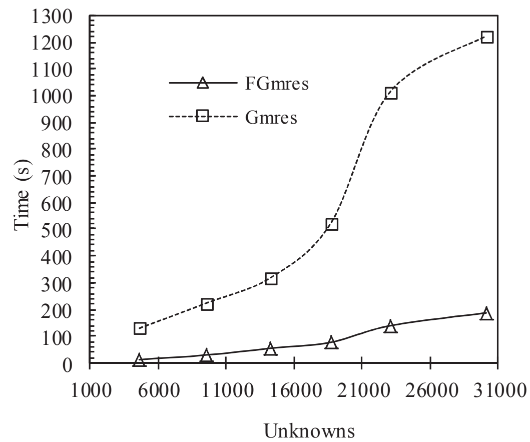

Fig. 16. The solving times for the VIAS geometry.

traditional ACA. With the application of the new far field interaction lists, an efficient version of ACA is obtained in this paper, while the accuracy of the modified ACA is controllable. It is observed that the convergence rate of GMRES is remarkably accelerated by the application of FGMRES algorithm. The proposed method is very efficient for analyzing the electromagnetic scattering problems.

ACKNOWLEDGMENT

We would like to thank the support of Major State Basic Research Development Program of China (973 Program: 2009CB320201); Natural Science Foundation of 60871013, 60701004, 60928002; Jiangsu Natural Science Foundation of BK2008048.

REFERENCES

[1] K. A. Michalski and D. L. Zheng, “Electromagnetic Scattering and Radiation by Surfaces of Arbitrary Shape in Layered Media, Part I: Theory,” *IEEE Trans. Antennas Propag,* vol. 38, no. 3, pp. 335-344, 1990.

[2] K. A. Michalski and D. L. Zheng, “Electromagnetic Scattering and Radiation by Surfaces of Arbitrary Shape in Layered Media, Part II: Implementation and Results for Contiguous Half-Spaces,” *IEEE Trans. Antennas Propag,* vol. 38, no. 3, pp. 345-352, 1990.

[3] S. M. Rao, D. R. Wilton, and A. W. Glisson, "Electromagnetic Scattering by Surfaces of Arbitrary Shape," *IEEE Trans. Antennas Propagat.*, vol. 30, no. 3, pp. 409-418, May 1982.

[4] E. H. Newman and D. Forrai, "Scattering from a Microstrip Patch," *IEEE Trans. Antennas Propagat.*, vol. AP-35, pp. 245-251, Mar. 1987.

[5] W. Zhuang, R. S. Chen, D. Z. Ding, and D. X. Wang, "An Efficient Analysis of Frequency Selective Surface in Spectral Domain with RWG Basis Functions," *Microw Opt. Technol. Lett*, vol. 51, no. 11, pp. 2567-2570, Nov. 2009.

[6] K. A. Michalski and C. G. Hsu, "RCS Computation of Coax-Loaded Microstrip Patch Antennas of Arbitrary Shape," *Electromagn.*, vol. 14, pp. 33-62, Jan.-Mar. 1994.

[7] R. Coifman, V. Rokhlin, and S. Wandzura, "The Fast Multipole Method for the Wave Equation: A Pedestrian Prescription," *IEEE Antennas Propag. Mag.*, vol. 35, no. 6, pp. 7-12, Jun. 1993.

[8] W. C. Chew, J. M. Jin, E. Michielssen, and J. Song, *Fast Efficient Algorithms in Computational Electromagnetics*, Boston, MA: Artech House, 2001.

[9] H. Zhao, J. Hu, and Z. Nie, "Parallelization of MLFMA with Composite Load Partition Criteria and Asynchronous Communication," *Applied Computational Electromagnetic Society (ACES) Journal*, vol. 25, no. 2, pp. 167-173, 2010.

[10] H. Fangjing, N. Zaiping, and H. Jun, "An Efficient Parallel Multilevel Fast Multipole Algorithm for Large-scale Scattering Problems," *Applied Computational Electromagnetic Society (ACES) Journal*, vol. 25, no. 4, pp. 381-387, 2010.

[11] K. Zhao, M. N. Vouvakis, and J. F. Lee, "The Adaptive Cross Approximation Algorithm for Accelerated Method of Moments Computations of EMC Problems," *Trans. on Elec. Comp.*, vol. 47, no. 4, pp. 763-773, Nov. 2005.

[12] D. Gope and V. Jandhyala, "Oct-Tree-Based Multilevel Low-Rank Decomposition Algorithm for Rapid 3-D Parasitic Extraction," *IEEE Trans. Computer-Aided Design*, vol. 23, no. 4, pp. 1575-1580, Nov. 2004.

[13] D. Gope, and V. Jandhyala, "Efficient Solution of EFIE via Low-Rank Compression of Multilevel Predetermined Interactions," *IEEE Trans. Antennas Propagat.*, vol. 53, no. 10, pp. 3324-3333, Oct. 2005.

[14] Y. Saad and M. H. Schultz, "GMRES: A Generalized Minimal Residual Algorithm for Solving Nonsymmetric Linear Systems," *SIAM J. Sci. Statist. Comput*, vol. 7, pp. 856-869, Jul. 1986.

[15] Y. Saad, "A Flexible Inner-Outer Preconditioned GMRES Algorithm," *SIAM J. Sci. Statist. Comput.*, vol. 14, pp. 461-469, 1993.

[16] R. S. Chen, D. Z. Ding, Z. H. Fan, E. K. N. Yung, and C. H. Chan, "Flexible GMRES-FFT Method for Fast Matrix Solution: Application to 3D Dielectric Bodies Electromagnetic Scattering," *Int. J. Numer. Model: Electronic. Networks, Devices and Fields*, vol. 17, pp. 523-537, 2004.

[17] R. S. Chen, Y. Q. Hu, Z. H. Fan, D. Z. Ding, D. X. Wang, and E. K. N. Yung, "An Efficient Surface Integral Equation Solution to EM Scattering by Chiral Objects above a Lossy Half Space," *IEEE Trans. Antennas Propag*, vol. 57, no. 11, pp. 3586-3593, Nov. 2009.

[18] E. Michielssen and A. Boag, "A Multilevel Matrix Decomposition Algorithm for Analyzing Scattering from Large Structures," *IEEE Trans. Antennas Propag*, vol. 44, no. 8, pp. 1086-1093, Aug. 1996.

[19] A. Heldring, J. M. Tamayo, J. M. Rius, and J. Parron, "Multilevel MDA-CBI for Fast Direct Solution of Large Scattering and Radiation Problems," *IEEE AP-S International Symposium 2007*, Honolulu, Hawaii, USA, 10-15 June 2007.

[20] J. M. Rius, J. Parron, E. Ubeda, and J. Mosig, "Multilevel Matrix Decomposition Algorithm for Analysis of Electrically Large Electromagnetic Problems in 3-D," *Microw Opt. Technol. Lett*, vol. 22, no. 3, pp. 177-182, Aug. 1999.

[21] J. Cheng, S. A. Maloney, R. J. Adams, and F.

X. Canning, "Efficient Fill of a Nested Representation of the EFIE at Low Frequencies," *IEEE Antennas and Propagation Society Int. Symp.*, pp. 1-4, 2008.

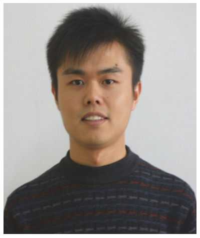

Zhaoneng Jiang was born in Jiangsu Province, the People's Republic of China. He received the B.S. degree in Physics from Huaiyin Normal College in 2007, and is currently working toward the Ph.D. degree at Nanjing University of Science and Technology (NJUST), Nanjing, China. His current research interests include computational electromagnetics, antennas and electromagnetic scattering and propagation, and electromagnetic modeling of microwave integrated circuits.

Ru-Shan Chen (M'01) was born in Jiangsu, P. R. China. He received his B.Sc. and M.Sc. degrees from the Dept. of Radio Engineering, Southeast University, in 1987 and in 1990, respectively, and his Ph.D. from the Dept. of Electronic Engineering, City University of Hong Kong in 2001. He joined the Dept. of Electrical Engineering, Nanjing University of Science & Technology (NJUST), where he became a Teaching Assistant in 1990 and a Lecturer in 1992. Since September 1996, he has been a Visiting Scholar with the Department of Electronic Engineering, City University of Hong Kong, first as Research Associate, then as a Senior Research Associate in July 1997, a Research Fellow in April 1998, and a Senior Research Fellow in 1999. From June to September 1999, he was also a Visiting Scholar at Montreal University, Canada. In September 1999, he was promoted to Full Professor and Associate Director of the Microwave & Communication Research Center in NJUST and in 2007, he was appointed Head of the Dept of Communication Engineering, Nanjing University of Science & Technology. His research interests mainly include microwave/millimeter-wave systems, measurements, antenna, RF-integrated circuits, and computational electromagnetics. He is a Senior Member of the Chinese Institute of Electronics (CIE). He received the 1992 third-class science and technology advance prize given by the National Military Industry Department of China, the 1993 third class science and technology advance prize given by the National Education Committee of China, the 1996 second-class science and technology advance prize given by the National Education Committee of China, and the 1999 first-class science and technology advance prize given by JiangSu Province as well as the 2001 second-class science and technology advance prize. At NUST, he was awarded the Excellent Honor Prize for academic achievement in 1994, 1996, 1997, 1999, 2000, 2001, 2002, and 2003. He has authored or co-authored more than 200 papers, including over 140 papers in international journals. He is the recipient of the Foundation for China Distinguished Young Investigators presented by the National Science Foundation (NSF) of China in 2003. In 2008, he became a Chang-Jiang Professor under the Cheung Kong Scholar Program awarded by the Ministry of Education, China.

Zhen-Hong Fan was born in Jiangsu, the People's Republic of China in 1978. He received the M.Sc. and Ph.D. degrees in Electromagnetic Field and Microwave Technique from Nanjing University of Science and Technology (NJUST), Nanjing, China, in 2003 and 2007, respectively. During 2006, he was with the Center of Wireless Communication in the City University of Hong Kong, Kowloon, as a Research Assistant. He is currently an associated Professor with the Electronic Engineering of NJUST. He is the author or coauthor of over 20 technical papers. His current research interests include computational electromagnetics, electromagnetic scattering, and radiation.

Yuyuan An was born in Sichuan Province, the People's Republic of China. He received the B.S. degree in Physics from Nanjing University of Science and Technology (NJUST) in 2009, and is currently working toward the Ph.D. degree at

Nanjing University of Science and Technology (NJUST), Nanjing, China. His current research interests include computational electromagnetics, antennas and electromagnetic scattering and propagation, and electromagnetic modeling of microwave integrated circuits.

Maomao Zhu was born in Anhui Province, the People's Republic of China. She received the B.S. degree in Physics from Anhui University in 2009, and is currently working toward the M.S. degree at Nanjing University of Science and Technology (NJUST), Nanjing, China. Her current research interests include computational electromagnetics, antennas and electromagnetic scattering and propagation, and electromagnetic modeling of microwave integrated circuits.

Kwok Wa Leung was born in Hong Kong SAR. He received his B.S. (Electronics) and Ph.D. (Electronic Engineering) from the Chinese University of Hong Kong in 1990 and 1993, respectively. From June 1988 to August 1989, he spent 15 months as a student trainee in the RF division of Motorola (HK) Limited. In 1994, he joined the City University of Hong Kong (CityU) as an Assistant Professor and is currently a Professor. From Jan.-June 2006, he was a Visiting Professor in the Department of Electrical Engineering, The Pennsylvania State University, USA. He was the Leader of the Departmental Graduate Research Programmes and of the B.Eng. (Honors) Programme in Electronic and Communication Engineering at City University. Professor Leung was the Chairman of the IEEE AP/MTT Hong Kong Joint Chapter for the years of 2006 and 2007. He was the Co-Chair of the Technical Program Committee, IEEE TENCON, Hong Kong, Nov. 2006, and was the Finance Chair of PIERS 1997, Hong Kong. He is currently the Chairman of the Technical Program Committee, 2008 Asia-Pacific Microwave Conference. His research interests include RFID tag antennas, dielectric resonator antennas, microstrip antennas, wire antennas, guided wave theory, numerical methods in electromagnetics, and mobile communications. He serves as an Editor for HKIE Transactions. He also serves as an Associate Editor for IEEE Transactions on Antennas and Propagation and for IEEE Antennas and Wireless Propagation Letters. Professor Leung received the International Union of Radio Science (USRI) Young Scientists Awards in 1993 and 1995, awarded in Kyoto, Japan and St. Petersburg, Russia, respectively. He is a Fellow of HKIE and a Senior Member of IEEE.

Gain and Bandwidth Limitations of Reflectarrays

Bhavani Devireddy, Ang Yu, Fan Yang, and Atef Z. Elsherbeni

Department of Electrical Engineering
The University of Mississippi, University, MS 38677-1848, USA
bdevired@olemiss.edu, ayu@olemiss.edu, fyang@olemiss.edu, atef@olemiss.edu

Abstract **-** In reflectarray antenna designs, it is important to find the gain and bandwidth for a desired application. In this paper, two analysis methods are illustrated, which can provide quick estimations on the reflectarray gain and bandwidth. A quantitative comparison on these two different approaches is made in terms of accuracy and computation time. Parametric studies are performed to provide design guidelines for selecting appropriate f/D ratio and feed pattern of a center-fed reflectarray in order to optimize the antenna gain and bandwidth. A gain and bandwidth comparison between the broadside and offset fed reflectarray antennas is presented. Furthermore, the effect of element bandwidth on the performance of an X-band reflectarray is given both numerically and experimentally.

Index Terms ─ Bandwidth, directivity, efficiency, gain, reflectarray.

I. INTRODUCTION

Reflectarray antenna combines the advantages of both traditional reflectors and conventional phased array antennas. It has a high gain like parabolic reflectors. But, unlike the reflector that has a theoretically infinite bandwidth due to its curved surface, the reflectarray has a narrow bandwidth due to its phase compensation mechanism.

In the last decades, it has been shown that there are mainly two factors which limit the bandwidth performance of a reflectarray antenna [1-2]. One is the narrow bandwidth of the microstrip patch element [3] and the other is the differential spatial path delay. The second bandwidth limitation factor depends on system parameters like aperture diameter (D), focal length to diameter ratio (f/D), and power factor (q) of the feed pattern. In this paper, the gain and bandwidth of reflectarrays are studied in details, and the focus is on the effects of the system parameters. Note that the frequency bandwidth in this paper, if not explicitly defined, is calculated at -1 dB from the maximum gain.

Section II of this paper describes two different methods to quickly estimate the reflectarray gain and bandwidth. A comparison is made in terms of accuracy and computation time. Focusing on the differential spatial delay effect, Section III presents the bandwidth study of a broadside center-fed reflectarray antenna. Parametric studies are performed in order to optimize the antenna gain and bandwidth. In Section IV, a comparison between broadside and offset reflectarray antenna in terms of gain and bandwidth is given. In Section V, an X-band reflectarray with identical circularly polarized elements but different rotation angles is investigated. Both the effect of differential spatial path delay and the effect of element bandwidth on the performance of reflectarray are studied. The simulated gain of this reflectarray antenna is compared with the measured result.

II. GAIN COMPUTATION METHODS

To analyze the radiation performance of reflectarray antennas, several approaches have been developed with different levels of accuracy and complexity. The most accurate method is to perform a full wave simulation on the entire reflectarray aperture and the feed horn. However, this method requires prohibitively large memory storage and computational time, especially for large-size reflectarrays. An infinite array approach is widely used by assuming local periodicity, where each reflectarray element is analyzed within a periodic environment to obtain its reflection magnitude and phase. The frequency variation, polarization status, and the actual incident angle can be considered in the simulation. Once the element property is determined, the aperture field distribution can be calculated and the radiation performance of the reflectarray can be obtained. This method is proved to be accurate; however, the algorithm is relatively complex and simulation time is relatively long.

In some engineering designs, it is necessary to provide quick estimations on the reflectarray performance such as the gain and bandwidth. In light of this, two simple and quick approaches are presented here for such estimations, which are based on the array theory and the aperture efficiency. Their accuracy and computational time are compared quantitatively in this paper. Combined with specific element phasing techniques, these approaches can be used to calculate the gain and bandwidth of reflectarray antennas.

The gain (G) calculation of a reflectarray antenna is defined as a product of the directivity (D_a) and aperture efficiency (η_a) [4] such that

$$G = D_a \times \eta_a, \tag{1}$$

where D_a of the aperture with an area A is

$$D_a = \frac{4\pi A}{\lambda^2}. \tag{2}$$

The η_a is the product of spillover efficiency (η_s), illumination efficiency (η_i) and other efficiency (η_o) factors. Other efficiencies include the feed loss, feed blockage, reflectarray element loss, polarization loss, mismatch loss, etc. Thus,

$$\eta_a = \eta_s \times \eta_i \times \eta_o. \tag{3}$$

In some gain computation methods, the directivity is calculated from the aperture field distribution [5-7]. Thus, the gain already includes the illumination efficiency which can then be represented by the following equation,

$$G = D_0 \times \eta_s \times \eta_o. \tag{4}$$

A. Directivity Calculations: Method 1

The directivity of an array with isotropic elements whose main beam is pointing in the $\theta = \theta_0$ and $\varphi=\varphi_0$ direction is given as,

$$D_0 = \frac{\left|AF(\theta_0,\varphi_0)\right|^2}{\frac{1}{4\pi}\int_0^{2\pi}\int_0^{\pi}\left|AF(\theta,\varphi)\right|^2 \sin\theta d\theta d\varphi}. \tag{5}$$

where,

$$AF(\theta,\varphi) = \sum_{n=0}^{N-1} A_n \cdot e^{j\phi_n} \cdot e^{j\beta\left(\hat{r}\cdot\vec{r}_n\right)}. \tag{6}$$

Here, A_n and ϕ_n are the amplitude and phase of the n^{th} array element, and

$$\hat{r}\cdot\vec{r}_n = p_{x_n}\sin\theta\cos\varphi + p_{y_n}\sin\theta\sin\varphi. \tag{7}$$

The position of the n^{th} element in an N-element planar array in the xy-plane is denoted by $\left(p_{x_n}, p_{y_n}\right)$. The array can have arbitrary configuration in the xy-plane and each element is indexed with a single index n. Note that N is the total number of elements and would equal to the product of the number of elements in x and y directions ($N_x \times N_y$) for a rectangular array.

The denominator in Eq. (5) referred to as '*DEN*' can be written as,

$$DEN \stackrel{\Delta}{=} \frac{1}{4\pi}\int_0^{2\pi}\int_0^{\pi}\left[AF(\theta,\varphi)\right]\left[AF(\theta,\varphi)\right]^* \sin\theta d\theta d\varphi. \tag{8}$$

When substituting equation (6) into equation (8), one obtains,

$$\begin{aligned} DEN = &\sum_{n=0}^{N-1}\sum_{m=0}^{N-1} w_n w_m^* \int_0^{\pi}\frac{1}{2}\sin\theta d\theta \\ &\int_0^{2\pi}\frac{1}{2\pi}\exp\left(j\frac{2\pi}{\lambda}\left(\Delta p_{x_{nm}}\sin\theta\cos\varphi + \Delta p_{y_{nm}}\sin\theta\sin\varphi\right)\right)d\varphi, \end{aligned} \tag{9}$$

where,

$$w_n = A_n \cdot e^{j\phi_n}, \tag{10}$$

$$\begin{aligned} \Delta p_{x_{nm}} &\stackrel{\Delta}{=} p_{x_n} - p_{x_m} = \rho_{nm}\cos\varphi_{nm}, \\ \Delta p_{y_{nm}} &\stackrel{\Delta}{=} p_{y_n} - p_{y_m} = \rho_{nm}\sin\varphi_{nm}, \end{aligned} \tag{11}$$

$$\begin{aligned} \rho_{nm} &= \left(\left(\Delta p_{x_{nm}}\right)^2 + \left(\Delta p_{y_{nm}}\right)^2\right)^{\frac{1}{2}} = \left\|\Delta p_{nm}\right\|, \\ \varphi_{nm} &= \arctan\left(\frac{\Delta p_{y_{nm}}}{\Delta p_{x_{nm}}}\right). \end{aligned} \tag{12}$$

Using Eqs. (11) and (12) in the inner integral in Eq. (9) gives

$$\begin{aligned} &\int_0^{2\pi}\frac{1}{2\pi}\exp\left(j\frac{2\pi}{\lambda}\rho_{nm}\sin\theta\left(\cos\left(\varphi-\varphi_{nm}\right)\right)\right)d\varphi \\ &= J_0\left(\frac{2\pi}{\lambda}\rho_{nm}\sin\theta\right), \end{aligned} \tag{13}$$

where $J_0(.)$ is a Bessel function of order zero. Substituting Eq. (13) into Eq. (9) gives

$$DEN = \sum_{n=0}^{N-1}\sum_{m=0}^{N-1} w_n w_m^* \int_0^{\pi} \frac{1}{2}\sin\theta . J_0\left(\frac{2\pi}{\lambda}\rho_{nm}\sin\theta\right)d\theta$$
$$= \sum_{n=0}^{N-1}\sum_{m=0}^{N-1} w_n w_m^* sinc\left(\frac{2\pi}{\lambda}\rho_{nm}\right). \quad (14)$$

Thus, the directivity in Eq. (5) can be calculated analytically, and the computational time of equation (14) is in the order of N^2.

B. Directivity Calculations: Method 2

Another simple approximation formula to calculate the directivity of a large planar array is,

$$D_0 = D_a \times \eta_i . \quad (15)$$

The illumination efficiency (η_i), due to the non-uniform amplitude and phase distribution on the aperture plane [8], is given as,

$$\eta_i = \eta_t \times \eta_{ph}, \quad (16)$$

where η_t and η_{ph} are the taper and phase efficiencies. The η_t accounts for the aperture illumination taper due to the feed and the reflector geometry and is given by,

$$\eta_t = \frac{1}{A}\frac{\left[\sum_{n=0}^{N-1}|E_n|\Delta x\Delta y\right]^2}{\sum_{n=0}^{N-1}|E_n|^2\Delta x\Delta y}. \quad (17)$$

The η_{ph} accounts for the phase-error over the aperture due to various causes such as, frequency change, displacement of the feed-horn from the on-axis focus, distortion of the optical surfaces, or it may be caused by phase-error in the field of the feed-horn. This η_{ph} is given by,

$$\eta_{ph} = \frac{\left|\sum_{n=0}^{N-1}E_n\Delta x\Delta y\right|^2}{\left[\sum_{n=0}^{N-1}|E_n|\Delta x\Delta y\right]^2}\times\cos\theta_0. \quad (18)$$

Finally, the illumination efficiency is given as,

$$\eta_i = \frac{1}{A}\frac{\left|\sum_{n=0}^{N-1}E_n\Delta x\Delta y\right|^2}{\sum_{n=0}^{N-1}|E_n|^2\Delta x\Delta y}\times\cos\theta_0, \quad (19)$$

where,

$$E_n = A_n\cdot e^{j\phi_n}\cdot e^{j\beta\left(\hat{r}_0\cdot\vec{r}_n\right)}. \quad (20)$$

The term $\beta(\hat{r}_0\cdot\vec{r}_n)$ is the phase due to the change in the main beam direction. For a broadside beam, this term will disappear. The parameters Δx and Δy represent the spacing between the elements along x and y axes, respectively. It is worthwhile to point out that the computational time in the denominator of Eq. (19) is only an order of N.

In summary, from Method 1 to Method 2, the computational time of the directivity is reduced from a $O(N^2)$ to $O(N)$.

C. Spillover Efficiency

The spillover efficiency (η_s) is defined as the ratio of the power intercepted by the reflecting elements to the total power [9],

$$\eta_s = \frac{\int_A \vec{p}.d\vec{s}}{\int_\Sigma \vec{p}.d\vec{s}}. \quad (21)$$

Both integrals are the fluxes of the Poynting vector $\vec{p}$ through some certain surface areas. The integral of the denominator is performed over the entire spherical surface centered at the feed, denoted by Σ. The integral in the numerator is evaluated on the array aperture A. Once the spillover efficiency is determined, the reflectarray gain can be calculated using equation (4).

D. Comparison of Results

By assuming the efficiency factor η_o = 1 in equation (4), a comparison between Method 1 and Method 2 for gain calculations was performed for a rectangular aperture reflectarray antenna which has a center feed and a broadside main beam (frequency = 32 GHz; spacing between elements = λ/2; f/D = 0.5; feed pattern power factor, q = 3). Ideal phasing elements are used in these comparisons. These comparisons are performed using Matlab on an Intel duo-core 3.2 GHz CPU and 2 GB of RAM and the results are reported in Table 1. Note that Method 1 always gives accurate results for any aperture size, whereas the approximation error in Method 2 decreases when the aperture size increases. Figure 1 illustrates the percentage error of Method 2 with respect to Method 1. The error is calculated using the following equation:

$$Error(\%) = \frac{|G(M2)-G(M1)|}{G(M1)}\times 100\%. \quad (22)$$

Of the two methods, the time taken for gain calculation is much less using Method 2. From Fig. 2, a clear agreement of the two methods at off-center frequencies can be seen for a broadside reflectarray. For 21 frequency points the Method

1 takes about 8 minutes whereas the Method 2 only takes around 30 seconds. The bandwidth obtained using either of the methods is about 5 %.

Table 1: Gain and CPU time comparison

Array size	Gain (dB)		Time (s)	
	Method 1	Method 2	Method 1	Method 2
11×11	24.3142	24.3855	0.6180	0.6060
21×21	30.0432	30.0834	0.6660	0.6420
41×41	35.9062	35.9307	2.2680	1.0140
81×81	41.8450	41.8622	22.2960	2.4840

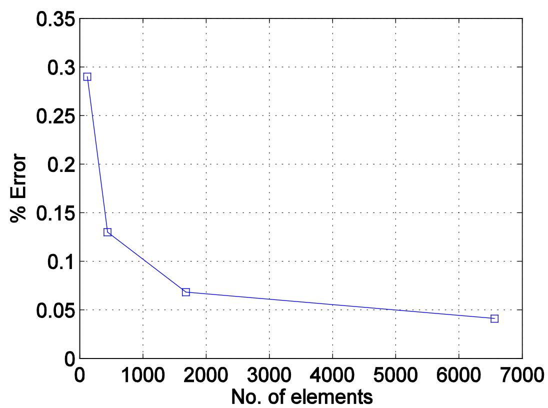

Fig. 1. Gain error of Method 2 vs. number of elements.

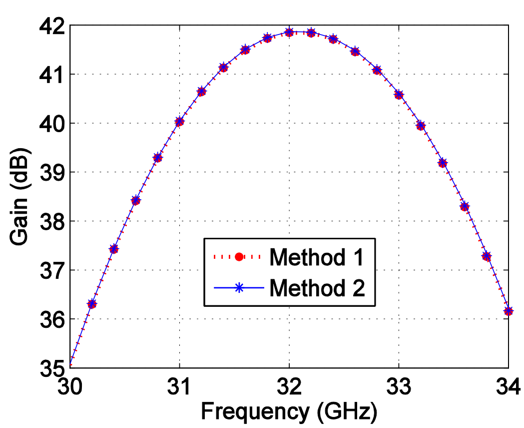

Fig. 2. Gain comparison of two methods for an 81×81 element reflectarray.

III. BANDWIDTH OF BROADSIDE FED REFLECTARRAY

Bandwidth of reflectarrays is determined by two factors: the system configuration and the element performance. In Sections III and IV, we focus on the effects of the system configuration, namely, the aperture size, the feed property, and the feed location. During this investigation, an ideal element phase is used, that is, as frequency varies the relative element reflection phase does not change. The reason for this assumption is to study only the effects of the system parameters. This assumption is valid also because in the element rotation technique, to be discussed in Section V, the relative reflection phase of the co-polarized CP wave (normalized to a reference element, e.g., the element located at the center of the aperture) only depends on the rotation angle and is therefore a constant over the frequency range of interest.

Considering the accuracy and computation time, Method 2 is used here to conduct a parametric study on the reflectarray gain and bandwidth performance.

A. Gain and Bandwidth vs. (f/D, q)

First, a parametric study has been done for a circular aperture (frequency = 32 GHz; spacing between elements = λ/2; diameter = 0.5 m (D/λ = 53.4); number of elements = 8937) with a gain around 43 dB. As the gain and bandwidth of a reflectarray varies with q and f/D ratio, an appropriate selection of these parameters is required. For a given q value, the gain versus f/D increases to a certain value and then decreases as shown in Fig. 3. The larger the q value, the narrower the horn beam. Thus, we need to choose a larger f/D in such cases in order to have a more uniform field distribution on the array.

It has been noticed that for a particular f/D and q value where we get maximum gain, the bandwidth may not be maximum. In Fig. 4, a gain of 43 dB is obtained for different combinations of f/D and q, but the bandwidth is wider for larger f/D and q values. The phase efficiencies at f/D = 0.5 and 0.75 are shown in Fig. 5 with q = 3. At off-center frequencies, the phase efficiency is high for large f/D ratio. This phase efficiency contributes to the increased bandwidth when we increase the f/D ratio. The bandwidth increases with an increase in the two parameters f/D and q as shown in Fig. 6.

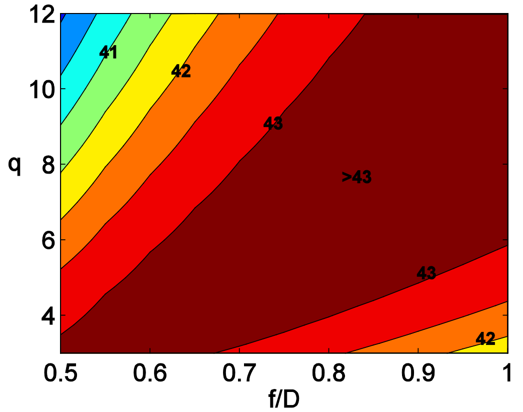

Fig. 3. Gain (dB) vs. (f/D, q) for a center-fed reflectarray at 32 GHz.

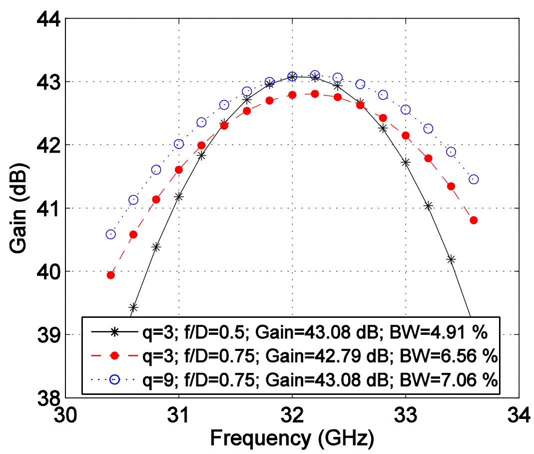

Fig. 4. Gain of center-fed reflectarrays with different q and f/D.

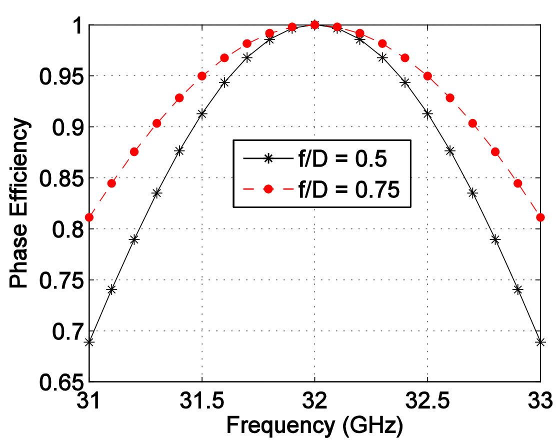

Fig. 5. Phase efficiency vs. frequency for a center-fed reflectarray with q = 3.

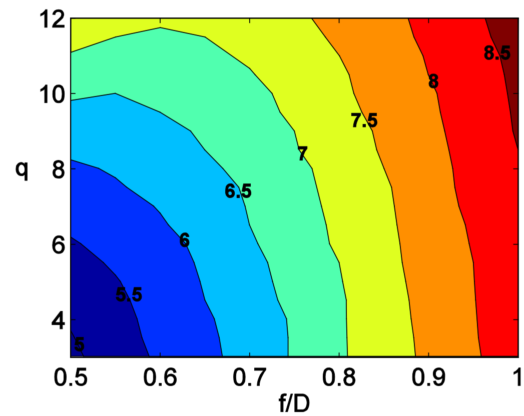

Fig. 6. Percentage bandwidth vs. (f/D, q) for a center-fed reflectarray.

B. Gain and Bandwidth Relation

A relation between gain and bandwidth of a large size (43 dB; D/λ = 53.4) and middle size (32 dB; D/λ = 16) reflectarray is shown in Figs. 7 and 8, respectively. It can be observed that for a fixed q value, the variation in gain is small (< 0.4 dB) when the f/D is increased. Meanwhile, the increase in bandwidth is high for a middle size reflectarray when compared to that of a large size reflectarray. At q = 3 and f/D from 0.5 - 0.74, the bandwidth of a large size reflectarray is varying from 4.91 % to 6.5 %, whereas the bandwidth of middle size reflectarray is varying from 16.37 % to 21.22 %. Figures 7 and 8 also illustrate that the gain and bandwidth are high for large f/D and q.

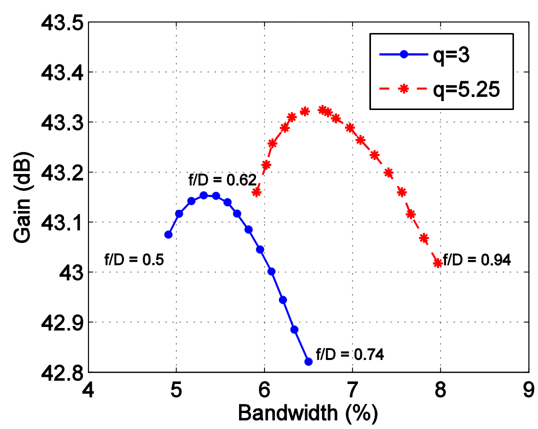

Fig. 7. Gain vs. bandwidth for a large size center-fed reflectarray with D/λ = 53.4.

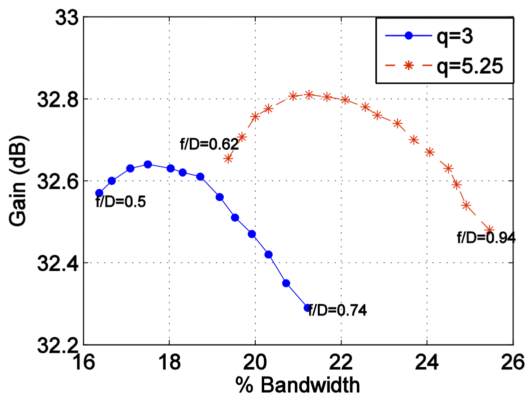

Fig. 8. Gain vs. bandwidth for a middle size center-fed reflectarray with D/λ = 16.

IV. BROADSIDE AND OFFSET FED REFLECTARRAY

For a circular aperture (frequency = 32 GHz; spacing between elements = λ/2; diameter = 0.5 m; number of elements = 8937), a comparison is done between broadside and offset reflectarrays. Here, the incident and main beam of the offset reflectarray is making an angle of 25° with respect to the broadside direction. In doing so, the reflected energy and the reradiated energy of each reflectarray element can be collocated in the same direction and not wasted [10]. At fixed f/D and q values, an offset reflectarray has lower gain but wider bandwidth (gain = 42.48 dB, bandwidth = 5.31%) when compared to that of a broadside reflectarray (gain = 43.08 dB, bandwidth = 4.95%), as shown in Fig. 9.

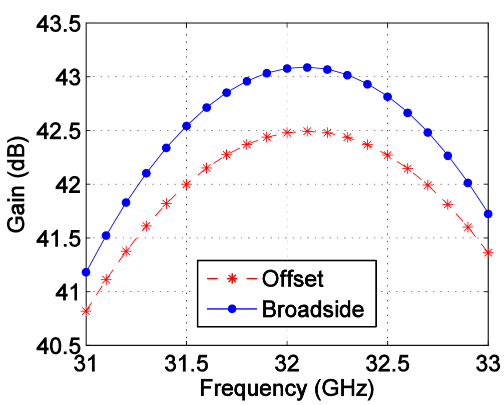

Fig. 9. Gain vs. frequency, for broadside and offset reflectarrays at q = 3 and f/D = 0.5.

The gain and bandwidth characteristics of both reflectarray antennas are shown in Fig. 10. At q = 3 and f/D = 0.4 - 0.74, for a broadside fed reflectarray, the maximum gain of 43.15 dB is achieved when f/D = 0.56, while the largest bandwidth of 6.5% is obtained when f/D = 0.74. Yet for an offset reflectarray antenna, the maximum gain of 42.5 dB is achieved when f/D = 0.52, while the largest bandwidth of 7.25% is obtained when f/D = 0.74.

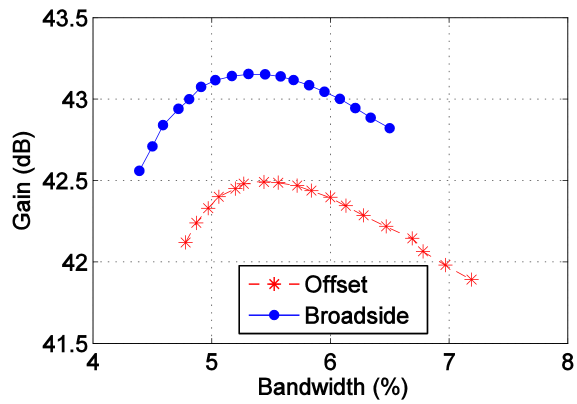

Fig. 10. Gain vs. bandwidth, for broadside and offset reflectarrays at q = 3 and f/D = 0.4 - 0.74.

V. ELEMENT BANDWIDTH EFFECT

In this section, the effect of the element bandwidth is included to investigate the performance of an X band reflectarray operating at 8.4 GHz. A split square loop is designed to reflect the CP wave with the same polarization state at X-band (8.4 GHz). A modified element rotation technique is used to compensate the spatial phase delay [11]. The full wave solver Ansoft Designer is applied in the element designs. Periodic boundary conditions (PBC) are placed around a single element to model an infinite array environment, and a plane wave is launched to illuminate the unit cell. It is worthwhile to point out that the mutual coupling effects between elements are considered in this analysis. The array grid is uniform and square shaped, with a period p = 18.75 mm between adjacent cells, as shown in Fig. 11. Figure 12 shows the magnitudes of the reflected co-polarized (right hand circularly polarized, RHCP) and the cross-polarized (left hand circularly polarized, LHCP) components under normal incidence. The element bandwidth obtained at -1 dB is about 4.29% (8.23-8.59 GHz) centered at 8.4 GHz. By rotating the slots around the perimeter of the square loop, different reflection phases can be obtained to compensate the spatial phase delay of elements at different locations on the reflecting surface.

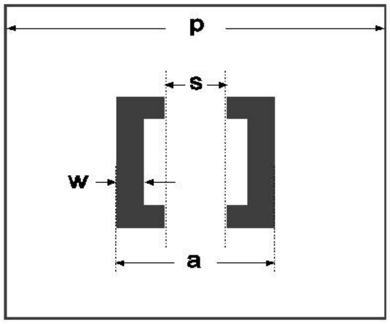

Fig. 11. Element geometry [11]: a = 11.375 mm, w = 2 mm, s = 7.2 mm and P = 18.75 mm, (substrate thickness = 1.57 mm and ε_r= 2.33).

The antenna elements are aligned on a circular aperture with the diameter D = 500 mm (D/λ = 14), f/D = 0.68, q = 6 and an offset feed structure is used with an angle of 25° aside from the normal direction of the reflector plane. Using these configuration parameters, the effect of differential spatial phase delay is studied first, and the results are shown in Fig. 13. Here, the gain is calculated using Method 2. As the aperture directivity (D_a) linearly increases with frequency, it can be observed that the maximum gain is obtained at 9 GHz instead of the design frequency 8.4 GHz. Figure 13 also shows the aperture efficiency over a frequency range of 7.8 GHz – 9 GHz. Note that the spillover and taper efficiencies are constant with frequency, but the phase efficiency varies with frequency. The gain bandwidth due to differential spatial phase delay is 25.83%.

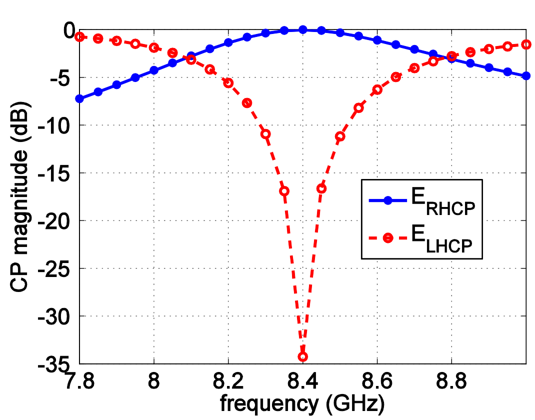

Fig. 12. Performance of the CP element using Ansoft Designer.

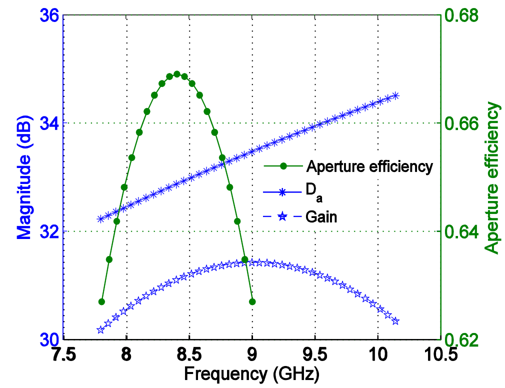

Fig. 13. Reflectarray performance due to spatial phase delay effect.

To include the element effect, the values of RHCP shown in Fig. 12 are considered as polarization mismatch in the code while doing frequency scan. The effect of element bandwidth on the performance of the reflectarray is shown in Fig. 14. The bandwidth with element effect is about 4.29% (8.25-8.61 GHz). The bandwidth obtained is equal to that of the element bandwidth, but note that the frequency range is slightly higher. It was observed that the bandwidth from element is much narrower than the bandwidth from differential spatial phase delay. Therefore, the element performance has a dominant effect on the reflectarray bandwidth compared to the spatial phase delay.

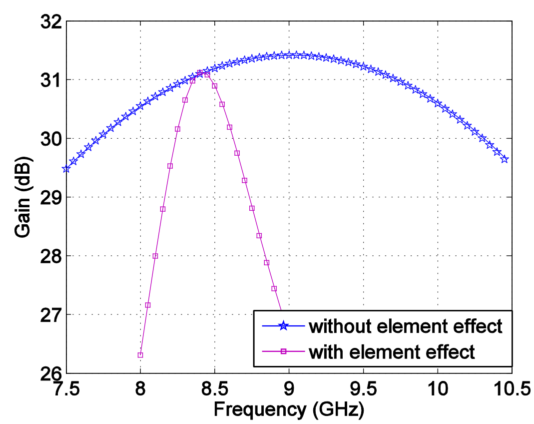

Fig. 14. Effects of spatial phase delay and element bandwidth on the reflectarray gain.

The gain of the reflectarray antenna obtained from simulations is compared with the measured result in Fig. 15. The gain of the prototype was obtained from near field measurements [11].

Table 2 summarizes the gain and bandwidth values. Since the measured result includes other efficiency factors such as the feed loss, which is lower than the simulated results. A major reason for the discrepancy between the simulated and measured results is due to the feed horn antenna effect. The q value, the purity of the RHCP beam, and the return loss of the horn all vary with frequency, which causes gain reduction. In particular at 8.8 GHz, the return loss of the horn is poor, resulting in a low gain. Since we do not have the complete data for the horn, this effect is not calculated in the simulation.

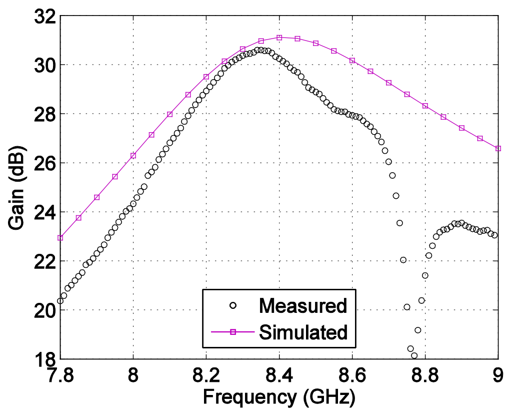

Fig. 15. Measured and simulated results of an offset reflectarray with D = 500 mm, f/D = 0.68, and q = 6.

Table 2: Gain and bandwidth from the measured and simulated results

	Gain at 8.4 GHz (dB)	1 dB Bandwidth (%)	3 dB Bandwidth (%)
Measured	30.25	2.86	6
Simulated	31.12	4.17	8.45

VI. CONCLUSION

Two methods of gain computation have been described, and it is observed that Method 2 has acceptable accuracy and takes less time for calculation. Based on the conducted parametric studies it was observed that the selection of f/D and q will affect both the gain and bandwidth performance of a reflectarray antenna. The tradeoff between gain and bandwidth is revealed to obtain an optimum performance of reflectarrays and it was observed that a reflectarray with large f/D and q can give a high gain and large bandwidth. At a fixed f/D and q value, an offset reflectarray has low gain but large bandwidth when compared to that of a broadside reflectarray. The gain and bandwidth of an X-band reflectarray has been calculated and the results are proved to be in good agreement with the measured results. For reflectarray with small D/λ, the spatial phase delay effect is smaller than the element effect on the performance of reflectarray.

ACKNOWLEDGEMENT

This work was supported by NASA/MS Space Grant Consortium under the contract number NNG05GJ72H and by NASA Stennis Space Center under the contract number NNX09AP18A.

REFERENCES

[1] J. Huang, “Bandwidth Study of Microstrip Reflectarray and a Novel Phased Reflectarray Concept,” *IEEE APS/URSI Symp. Dig.*, Newport Beach, CA, USA, pp. 582-585, June 1995.

[2] D. M. Pozar, “Bandwidth of Reflectarrays,” *Electronic Letters*, vol. 39, no. 21, pp. 1490-1491, Oct. 2003.

[3] S. Gultekin, K. Guney, and S. Sagiroglu, “Neural Networks for the Calculation of Bandwidth of Rectangular Microstrip Antennas,” *ACES Journal*, vol. 18, no. 2, pp. 46-56, 2003.

[4] A. W. Rudge, K. Milne, A. D. Olver, and P. Knight, *The Handbook of Antenna Design*, vols. 1 and 2, Chap. 3, pp.169-182, 1986.

[5] C. A. Balanis, *Antenna Theory*, Third ed., John Wiley & Sons, New Jersey, 2005.

[6] H. L. Van Trees, *Detection, Estimation, and Modulation Theory, Optimum Array Processing*, Part IV, John Wiley & Sons, 2002.

[7] W. L. Stutzman and G. A. Thiele, *Antenna theory and Design*, 2 ed., John Wiley & Sons, 1998.

[8] W. V. Cappellen, “Efficiency and Sensitivity Definitions for Reflector Antennas in Radio-Astronomy,” *SKADS MCCT Workshop*, 26-30 Nov. 2007.

[9] A. Yu, F. Yang, A. Z. Elsherbeni, J. Huang, and Y. Rahmat-Samii, “Aperture Efficiency Analysis of Reflectarray Antennas,” *Microwave and Optical Technology Letters*, vol. 52, no. 2, pp. 364-372, Feb. 2010.

[10] J. Huang and J. A. Encinar, *Reflectarray Antennas*, John Wiley & Sons, New Jersey, 2007.

[11] F. Yang, A. Yu, A. Z. Elsherbeni, and J. Huang, "An X-Band Circularly Polarized Reflectarray Using Split Square Ring Elements and the Modified Element Rotation Technique," The 2008 IEEE International Symposium on Antennas and Propagation, pp.1-4, 5-11 July 2008.

Bhavani Devireddy received her Bachelor of Technology degree from Jawaharlal Nehru Technological University, Hyderabad, India, in Electronics and Communications Engineering, in 2007. She received her M.S. degree from the University of Mississippi in 2010. Her research interests are focused on reflectarray antennas.

Ang Yu was born in Beijing, China, in 1978. He received the B.S. and M.S. degrees from Tsinghua University, Beijing, China, both in Electrical Engineering, in 2000 and 2003, respectively and received his Ph.D. degree from the University of Mississippi in 2010. From 2000 to 2003, he was a Research Assistant with the State Key Laboratory of Microwave and Digital Communications, Tsinghua University, Beijing, China. From 2003 to 2005, he was an engineer in Beijing Zhongjiaxun Antenna Technology Corporation. His research interests include microstrip antenna and array design, electromagnetic band gap structures and metamaterials.

Fan Yang received the B.S. and M.S. degrees from Tsinghua University in 1997 and 1999, and the Ph.D. degree from University of California, Los Angeles (UCLA) in 2002. He is an Associate Professor at the Electrical Engineering Department, The University of Mississippi. Dr. Yang's research interests include antenna theory, designs, and measurements, electromagnetic band gap (EBG) structures and their applications, computational electromagnetics and optimization techniques, and applied electromagnetic systems such as the radio frequency identification (RFID) system and concentrating solar energy system. He has published over 150 technical journal articles and conference papers, five book chapters, and two books entitled *Electromagnetic Band Gap Structures in Antenna Engineering* and *Electromagnetics and Antenna Optimization Using Taguchi's Method*. Dr. Yang serves as an Associate Editor of the *ACES Journal* and the *IEEE Trans. Antennas Propagation*. He is also a frequent reviewer for over twenty scientific journals and book publishers, and has chaired numerous technical sessions in various international symposiums.

Atef Elsherbeni is a Professor of Electrical Engineering and Associate Dean of Engineering for Research and Graduate Programs, the Director of The School of Engineering CAD Lab, and the Associate Director of The Center for Applied Electromagnetic Systems Systems Research (CAESR) at The University of Mississippi. In 2004, he was appointed as an adjunct Professor, at The Department of Electrical Engineering and Computer Science of the L.C. Smith College of Engineering and Computer Science at Syracuse University. In 2009, he was selected as Finland Distinguished Professor by the Academy of Finland and TEKES. Dr. Elsherbeni is the co-author of the following books: *The Finite Difference Time Domain Method for Electromagnetics With MATLAB Simulations*, SciTech 2009; the book *Antenna Design and Visualization Using Matlab*, SciTech, 2006; *MATLAB Simulations for Radar Systems Design*, CRC Press, 2003; *Electromagnetic ScatteringUsing the Iterative Multiregion Technique*, Morgan & Claypool, 2007; *Electromagnetics and Antenna Optimization using Taguchi's Method*, Morgan & Claypool, 2007; and the main author of the chapters "Handheld Antennas" and "The Finite Difference Time Domain Technique for Microstrip Antennas" in *Handbook of Antennas in Wireless Communications*, CRC Press, 2001. Dr. Elsherbeni is a Fellow member of the Institute of Electrical and Electronics Engineers (IEEE) and a Fellow member of The Applied Computational Electromagnetic Society (ACES). He is the Editor-in-Chief for ACES Journal.

2011 INSTITUTIONAL MEMBERS

DTIC-OCP LIBRARY
8725 John J. Kingman Rd, Ste 0944
Fort Belvoir, VA 22060-6218

AUSTRALIAN DEFENCE LIBRARY
Northcott Drive
Canberra, A.C.T. 2600 Australia

BEIJING BOOK CO, INC
701 E Linden Avenue
Linden, NJ 07036-2495

DARTMOUTH COLLEGE
6025 Baker/Berry Library
Hanover, NH 03755-3560

DSTO EDINBURGH
AU/33851-AP, PO Box 830470
Birmingham, AL 35283

SIMEON J. EARL – BAE SYSTEMS
W432A, Warton Aerodome
Preston, Lancs., UK PR4 1AX

ENGINEERING INFORMATION, INC
PO Box 543
Amsterdam, Netherlands 1000 Am

ETSE TELECOMUNICACION
Biblioteca, Campus Lagoas
Vigo, 36200 Spain

GA INSTITUTE OF TECHNOLOGY
EBS-Lib Mail code 0900
74 Cherry Street
Atlanta, GA 30332

TIMOTHY HOLZHEIMER
Raytheon
PO Box 1044
Rockwall, TX 75087

HRL LABS, RESEARCH LIBRARY
3011 Malibu Canyon
Malibu, CA 90265

IEE INSPEC
Michael Faraday House
6 Hills Way
Stevenage, Herts UK SG1 2AY

INSTITUTE FOR SCIENTIFIC INFO.
Publication Processing Dept.
3501 Market St.
Philadelphia, PA 19104-3302

LIBRARY – DRDC OTTAWA
3701 Carling Avenue
Ottawa, Ontario, Canada K1A OZ4

LIBRARY of CONGRESS
Reg. Of Copyrights
Attn: 407 Deposits
Washington DC, 20559

LINDA HALL LIBRARY
5109 Cherry Street
Kansas City, MO 64110-2498

MISSOURI S&T
400 W 14th Street
Rolla, MO 56409

MIT LINCOLN LABORATORY
Periodicals Library
244 Wood Street
Lexington, MA 02420

NATIONAL CHI NAN UNIVERSITY
Lily Journal & Book Co, Ltd
20920 Glenbrook Drive
Walnut, CA 91789-3809

JOHN NORGARD
UCCS
20340 Pine Shadow Drive
Colorado Springs, CO 80908

OSAMA MOHAMMED
Florida International University
10555 W Flagler Street
Miami, FL 33174

NAVAL POSTGRADUATE SCHOOL
Attn:J. Rozdal/411 Dyer Rd./ Rm 111
Monterey, CA 93943-5101

NDL KAGAKU
C/0 KWE-ACCESS
PO Box 300613 (JFK A/P)
Jamaica, NY 11430-0613

OVIEDO LIBRARY
PO BOX 830679
Birmingham, AL 35283

DAVID PAULSEN
E3Compliance
1523 North Joe Wilson Road
Cedr Hill, TX 75104-1437

PENN STATE UNIVERSITY
126 Paterno Library
University Park, PA 16802-1808

DAVID J. PINION
1122 E Pike Street #1217
SEATTLE, WA 98122

KATHERINE SIAKAVARA
Gymnasiou 8
Thessaloniki, Greece 55236

SWETS INFORMATION SERVICES
160 Ninth Avenue, Suite A
Runnemede, NJ 08078

YUTAKA TANGE
Maizuru Natl College of Technology
234 Shiroya
Maizuru, Kyoto, Japan 625-8511

TIB & UNIV. BIB. HANNOVER
DE/5100/G1/0001
Welfengarten 1B
Hannover, Germany 30167

UEKAE
PO Box 830470
Birmingham, AL 35283

UNIV OF CENTRAL FLORIDA
4000 Central Florida Boulevard
Orlando, FL 32816-8005

UNIVERSITY OF COLORADO
1720 Pleasant Street, 184 UCB
Boulder, CO 80309-0184

UNIVERSITY OF KANSAS – WATSON
1425 Jayhawk Blvd 210S
Lawrence, KS 66045-7594

UNIVERSITY OF MISSISSIPPI
JD Williams Library
University, MS 38677-1848

UNIVERSITY LIBRARY/HKUST
Clear Water Bay Road
Kowloon, Honk Kong

CHUAN CHENG WANG
8F, No. 31, Lane 546
MingCheng 2nd Road, Zuoying Dist
Kaoshiung City, Taiwan 813

THOMAS WEILAND
TU Darmstadt
Schlossgartenstrasse 8
Darmstadt, Hessen, Germany 64289

STEVEN WEISS
US Army Research Lab
2800 Powder Mill Road
Adelphi, MD 20783

YOSHIHIDE YAMADA
NATIONAL DEFENSE ACADEMY
1-10-20 Hashirimizu
Yokosuka, Kanagawa,
Japan 239-8686

APPLIED COMPUTATIONAL ELECTROMAGNETICS SOCIETY JOURNAL
http://aces.ee.olemiss.edu

INFORMATION FOR AUTHORS

PUBLICATION CRITERIA

Each paper is required to manifest some relation to applied computational electromagnetics. **Papers may address general issues in applied computational electromagnetics, or they may focus on specific applications, techniques, codes, or computational issues.** While the following list is not exhaustive, each paper will generally relate to at least one of these areas:

1. **Code validation.** This is done using internal checks or experimental, analytical or other computational data. Measured data of potential utility to code validation efforts will also be considered for publication.

2. **Code performance analysis.** This usually involves identification of numerical accuracy or other limitations, solution convergence, numerical and physical modeling error, and parameter tradeoffs. However, it is also permissible to address issues such as ease-of-use, set-up time, run time, special outputs, or other special features.

3. **Computational studies of basic physics.** This involves using a code, algorithm, or computational technique to simulate reality in such a way that better, or new physical insight or understanding, is achieved.

4. **New computational techniques** or new applications for existing computational techniques or codes.

5. **"Tricks of the trade"** in selecting and applying codes and techniques.

6. **New codes, algorithms, code enhancement, and code fixes.** This category is self-explanatory, but includes significant changes to existing codes, such as applicability extensions, algorithm optimization, problem correction, limitation removal, or other performance improvement. **Note: Code (or algorithm) capability descriptions are not acceptable, unless they contain sufficient technical material to justify consideration.**

7. **Code input/output issues.** This normally involves innovations in input (such as input geometry standardization, automatic mesh generation, or computer-aided design) or in output (whether it be tabular, graphical, statistical, Fourier-transformed, or otherwise signal-processed). Material dealing with input/output database management, output interpretation, or other input/output issues will also be considered for publication.

8. **Computer hardware issues.** This is the category for analysis of hardware capabilities and limitations of various types of electromagnetics computational requirements. Vector and parallel computational techniques and implementation are of particular interest.

Applications of interest include, but are not limited to, antennas (and their electromagnetic environments), networks, static fields, radar cross section, inverse scattering, shielding, radiation hazards, biological effects, biomedical applications, electromagnetic pulse (EMP), electromagnetic interference (EMI), electromagnetic compatibility (EMC), power transmission, charge transport, dielectric, magnetic and nonlinear materials, microwave components, MEMS, RFID, and MMIC technologies, remote sensing and geometrical and physical optics, radar and communications systems, sensors, fiber optics, plasmas, particle accelerators, generators and motors, electromagnetic wave propagation, non-destructive evaluation, eddy currents, and inverse scattering.

Techniques of interest include but not limited to frequency-domain and time-domain techniques, integral equation and differential equation techniques, diffraction theories, physical and geometrical optics, method of moments, finite differences and finite element techniques, transmission line method, modal expansions, perturbation methods, and hybrid methods.

Where possible and appropriate, authors are required to provide statements of quantitative accuracy for measured and/or computed data. This issue is discussed in "Accuracy & Publication: Requiring, quantitative accuracy statements to accompany data," by E. K. Miller, *ACES Newsletter,* Vol. 9, No. 3, pp. 23-29, 1994, ISBN 1056-9170.

SUBMITTAL PROCEDURE

All submissions should be uploaded to ACES server through ACES web site (http://aces.ee.olemiss.edu) by using the upload button, journal section. Only pdf files are accepted for submission. The file size should not be larger than 5MB, otherwise permission from the Editor-in-Chief should be obtained first. Automated acknowledgment of the electronic submission, after the upload process is successfully completed, will be sent to the corresponding author only. It is the responsibility of the corresponding author to keep the remaining authors, if applicable, informed. Email submission is not accepted and will not be processed.

EDITORIAL REVIEW

In order to ensure an appropriate level of quality control, papers are peer reviewed. They are reviewed both for technical correctness and for adherence to the listed guidelines regarding information content and format.

PAPER FORMAT

Only camera-ready electronic files are accepted for publication. The term **"camera-ready" means that the material is neat, legible, reproducible, and in accordance with the final version format listed below.**

The following requirements are in effect for the final version of an ACES Journal paper:

1. The paper title should not be placed on a separate page.

The title, author(s), abstract, and (space permitting) beginning of the paper itself should all be on the first page. The title, author(s), and author affiliations should be centered (center-justified) on the first page. The title should be of font size 16 and bolded, the author names should be of font size 12 and bolded, and the author affiliation should be of font size 12 (regular font, neither italic nor bolded).

2. An abstract is required. The abstract should be a brief summary of the work described in the paper. It should state the computer codes, computational techniques, and applications discussed in the paper (as applicable) and should otherwise be usable by technical abstracting and indexing services. The word "Abstract" has to be placed at the left margin of the paper, and should be bolded and italic. It also should be followed by a hyphen (—) with the main text of the abstract starting on the same line.

3. All section titles have to be centered and all the title letters should be written in caps. The section titles need to be numbered using roman numbering (I. II. ….)

4. Either British English or American English spellings may be used, provided that each word is spelled consistently throughout the paper.

5. Internal consistency of references format should be maintained. As a guideline for authors, we recommend that references be given using numerical numbering in the body of the paper (with numerical listing of all references at the end of the paper). The first letter of the authors' first name should be listed followed by a period, which in turn, followed by the authors' complete last name. Use a coma (,) to separate between the authors' names. Titles of papers or articles should be in quotation marks (" "), followed by the title of journal, which should be in italic font. The journal volume (vol.), issue number (no.), page numbering (pp.), month and year of publication should come after the journal title in the sequence listed here.

6. Internal consistency shall also be maintained for other elements of style, such as equation numbering. Equation numbers should be placed in parentheses at the right column margin. All symbols in any equation have to be defined before the equation appears or right immediately following the equation.

7. The use of SI units is strongly encouraged. English units may be used as secondary units (in parentheses).

8. Figures and tables should be formatted appropriately (centered within the column, side-by-side, etc.) on the page such that the presented data appears close to and after it is being referenced in the text. When including figures and tables, all care should be taken so that they will appear appropriately when printed in black and white. For better visibility of paper on computer screen, it is good to make color figures with different line styles for figures with multiple curves. Colors should also be tested to insure their ability to be distinguished after black and white printing. Avoid the use of large symbols with curves in a figure. It is always better to use different line styles such as solid, dotted, dashed, etc.

9. A figure caption should be located directly beneath the corresponding figure, and should be fully justified.

10. The intent and meaning of all text must be clear. For authors who are not masters of the English language, the ACES Editorial Staff will provide assistance with grammar (subject to clarity of intent and meaning). However, this may delay the scheduled publication date.

11. Unused space should be minimized. Sections and subsections should not normally begin on a new page.

ACES reserves the right to edit any uploaded material, however, this is not generally done. It is the author(s) responsibility to provide acceptable camera-ready files in pdf and MSWord formats. Incompatible or incomplete files will not be processed for publication, and authors will be requested to re-upload a revised acceptable version.

COPYRIGHTS AND RELEASES

PUBLICATION CHARGES

All authors are allowed for 8 printed pages per paper without charge. Mandatory page charges of $75 a page apply to all pages in excess of 8 printed pages. Authors are entitled to one, free of charge, copy of the printed journal issue in which their paper was published. Additional reprints are available for $ 50. Requests for additional re-prints should be submitted to the managing editor or ACES Secretary.

Corresponding author is required to complete the online form for the over page charge payment right after the initial acceptance of the paper is conveyed to the corresponding author by email.

ACES Journal is abstracted in INSPEC, in Engineering Index, DTIC, Science Citation Index Expanded, the Research Alert, and to Current Contents/Engineering, Computing & Technology.